DOT/FAA/TC-19/50, P1

Federal Aviation Administration
William J. Hughes Technical Center
Aviation Research Division
Atlantic City International Airport
New Jersey 08405

Development of a Tabulated Material Model for Composite Material Failure, MAT213

Part 1: Theory, Implementation, Verification & Validation

Date: January 2020

Final Report

This document is available to the U.S. public through the National Technical Information Services (NTIS), Springfield, Virginia 22161.

This document is also available from the Federal Aviation Administration William J. Hughes Technical Center at actlibrary.tc.faa.gov.

U.S. Department of Transportation
Federal Aviation Administration

NOTICE

Technical Report Documentation Page

1. Report No.	2. Government Accession No.	3. Recipient's Catalog No.
DOT/FAA/TC-19/50, P1		

4. Title and Subtitle	5. Report Date
Development of a Tabulated Material Model for Composite Material Failure, MAT213 Part 1: Theory, Implementation, Verification & Validation	January 2020
	6. Performing Organization Code

7. Author(s)	8. Performing Organization Report No.
Canio Hoffarth, Bilal Khaled, Loukham Shyamsunder, and Subramaniam Rajan	

9. Performing Organization Name and Address	10. Work Unit No. (TRAIS)
School of Sustainable Engineering and the Built Environment Arizona State University 660 South College Ave Tempe, AZ 85281-3005	11. Contract or Grant No. FAA Grant 12-G-001 NASA Contract NN15CA32

12. Sponsoring Agency Name and Address	13. Type of Report and Period Covered
U.S. Department of Transportation Federal Aviation Administration FAA New England Regional Office 1200 District Ave Burlington, MA 01803	Final Report
	14. Sponsoring Agency Code AIR-6A0

15. Supplementary Notes

The Federal Aviation Administration Aviation William J. Hughes Technical Center Research Division COR was Daniel Cordasco and the NASA Glenn Research Center Contracting Officer Representative was Robert Goldberg

16. Abstract

One of the challenges in building a predictive numerical model for composites is the ability to accurately model the behavior of the structure, especially under impact loading. This report provides details of a newly developed orthotropic material model that has three distinct sub-models for describing deformation, damage, and failure of general composites, and has been implemented in the commercial finite element program, LS-DYNA, as *MAT_213 (*MAT_COMPOSITE_TABULATED_PLASTICITY _DAMAGE). The model is driven by tabulated data that can be generated using laboratory tests or via virtual testing. The yield function is a modified form the Tsai-Wu failure model. A non-associated plastic flow is used. Rate and temperature dependence are supported along with tension-compression asymmetric behavior. The damage sub-model allows for both uncoupled and coupled parameters to be defined. Strain equivalence between the true and the effective stress space permits decoupling the plasticity and damage calculations. The failure modeling is currently being enhanced, and the initial version discussed in this report includes some of the most commonly used failure criteria – principal strain, Tsai-Wu, and a generalized tabulated laminate failure criterion.

Part 1 describes the experimental procedures and results from characterizing a widely used aerospace composite – T800-F3900.

Part 2 discusses the theory, implementation, verification and validation of MAT213 material model using the T800-F3900 composite as a test case. Verification tests are carried out using single and multiple element models. Validation tests are carried out using data from impact tests carried out at NASA-GRC involving T800-F3900 composite panels.

Part 3 discusses the probabilistic modeling implementation in LS-DYNA to support MAT213 (via *DEFINE_STOCHASTIC_ VARIATION_MAT213) and compares the results from deterministic and probabilistic modeling of impact events.

17. Key Words	18. Distribution Statement
Orthotropic plasticity, material characterization testing, damage, failure, cohesive zone modeling, explicit finite element analysis, probabilistic modeling, impact simulations. Composite failure, LSDYNA, MAT213, Tabulated material model	This document is available to the U.S. public through the National Technical Information Service (NTIS), Springfield, Virginia 22161. This document is also available from the Federal Aviation Administration William J. Hughes Technical Center at actlibrary.tc.faa.gov.

19. Security Classif. (of this report)	20. Security Classif. (of this page)	21. No. of Pages	22. Price
Unclassified	Unclassified		

TABLE OF CONTENTS

LIST OF FIGURES

LIST OF TABLES

LIST OF ACRONYMS

ASU	Arizona State University
FAA	Federal Aviation Administration
GRC	Glenn research Center
NASA	National Aeronautics and Space Administration

NOMENCLATURE

C = elastic stiffness matrix

$f(\sigma)$ = yield function with respect to the stress state

F_k = coefficients in vector portion of yield function

F_{ij} = coefficients in tensor portion of yield function

h = plastic potential function

$\left.\frac{\partial h}{\partial \boldsymbol{\sigma}}\right|_{n+1}^{i}$ = gradient of plastic potential function for iteration i of time step n+1

H_{ij} = constant coefficients of plastic potential function

q = vector of yield stresses in various coordinate directions

$\mathbf{q}_{n+1}^{i+1}$ = vector of yield stresses for iteration *i+1* of time step *n+1*

$\dot{W}^{p}$ = plastic work rate

$\Delta\boldsymbol{\varepsilon}$ = strain increment tensor

ε_{i-j}^{45} = yield strain from 45º test in *i-j* plane

$\dot{\boldsymbol{\varepsilon}}^{p}$ = plastic strain rate tensor

$\dot{\varepsilon}_{e}^{p}$ = effective plastic strain rate

$d\varepsilon_{e}^{p}$ = increment of effective plastic strain

$\dot{\varepsilon}_{ij}^{p}$ = components of plastic strain rate

$d\varepsilon_{ij}^{p}$ = components of increments of plastic strain

$\dot{\lambda}$ = scalar plastic multiplier equal to effective plastic strain rate

λ_n = effective plastic strain for time step *n*

$\Delta\lambda_{n+1}^{i+1}$ = increment of effective plastic strain for iteration *i+1* of time step *n+1*

$\boldsymbol{\sigma}$ = stress tensor

$\boldsymbol{\sigma}_n$ = stress tensor at time step n

$\boldsymbol{\sigma}_{n+1}^{i+1}$ = stress tensor for iteration *i+1* at time step *n+1*

σ_e = effective stress

σ_{ij} = stress components

σ_{ij}^{c} = compressive yield stresses

σ_{ij}^{t} = tensile yield stresses

$\sigma_{ij}'^{45}$ = yield stress from 45º off-axis test in *i-j* plane

ν_{ij} = elastic Poisson's ratio in *ij* direction

ν_{ij}^{p} = plastic Poisson's ratio in *ij* direction

d = deformation rate tensor

d_{ij} = deformation rate components

E_{ii} = elastic modulus in the *ii* direction

G_{ij} = elastic shear modulus in the *i-j* plane

EXECUTIVE SUMMARY

One of the challenges in building a predictive numerical model for composites is the ability to accurately model the behavior of the structure especially under impact loading. This report provides details of a newly developed orthotropic material model that has three distinct sub-models for describing deformation, damage, and failure of general composites and has been implemented in the commercial finite element program, LS-DYNA, as *MAT_213 (*MAT_COMPOSITE_TABULATED_PLASTICITY _DAMAGE). The model is driven by tabulated data that can be generated using laboratory tests or via virtual testing. The yield function is a modified form of the Tsai-Wu failure model. A non-associated plastic flow is used. Rate and temperature dependence are supported along with tension-compression asymmetric behavior. The damage sub-model allows for both uncoupled and coupled parameters to be defined. Strain equivalence between the true and the effective stress space permits decoupling the plasticity and damage calculations. The failure modeling is currently being enhanced, and the initial version discussed in this report includes some of the most commonly used failure criteria – principal strain, Tsai-Wu, and a generalized tabulated laminate failure criterion.

Part 1 describes the experimental procedures and results from characterizing a widely used aerospace composite – T800-F3900. Part 2 discusses the theory, implementation, verification, and validation of the MAT213 material model using the T800-F3900 composite as a test case. Verification tests are carried out using single and multiple element models. Validation tests are carried out using data from impact tests carried out at NASA-GRC involving T800-F3900 composite panels. Part 3 discusses the probabilistic modeling implementation in LS-DYNA to support MAT213 (via *DEFINE_STOCHASTIC_VARIATION_MAT213) and compares the results from deterministic and probabilistic modeling of impact events.

1. INTRODUCTION

Composite materials are now beginning to provide uses in structural systems hitherto reserved for metals such as airframes and engine containment systems, wraps for repair and rehabilitation, and ballistic/blast mitigation systems [1]. In the United States, several governmental agencies (including NASA and the FAA) recognized the importance of building a framework for composite systems by forming a public-private consortium. A press release [2] states that “NASA formed the consortium in support of the Advanced Composites Project, which is part of the Advanced Air Vehicles Program in the agency’s Aeronautics Research Mission Directorate. The project’s goal is to reduce product development and certification timelines by 30 percent for composites infused into aeronautics applications.”

A major reason for these challenges is the lack of mature material models that should be able to predict, with some degree of certainty, the deformation, damage, and failure of composite systems [3]. The list of desirable features in a general composite model includes the following:

- Continuum Damage Model with generalized, tabulated input, stress strain curve for non-damage related behavior (with limited or no curve fitting required by user).
- Current models use point-wise properties that lead to curve fit approximations to actual material response.
- Tabulated input based on a well-defined set of mechanical property tests leads to more accurate representations of actual material behavior.
- Input parameters based upon standard mechanical property tests (although alternate specimen test configurations or micro-mechanic analytical approaches producing virtual test results should be acceptable).
- Effects of strain rate need to be accounted for in a flexible, unified manner accounting for anisotropy of rate effects.
- Temperature dependency.
- Strain-based damage and failure parameters.
- Failure parameters adjusted for mesh size, i.e., mesh regularization (to adjust for localization effects in element removal).
- Explicit modeling of inter-laminar delamination via tiebreak contact and cohesive zone elements.
- Shell and solid element implementations required (though thickness properties can be important).
- Must be computationally fast.

The items in this list are addressed at various locations in this report and links to the current research work are drawn appropriately.

1.1 LITERATURE SURVEY

While material models exist that can be used to simulate the response of a variety of materials in these demanding applications under impact conditions, the more mature material models have focused on simulating the response of standard materials, such as metals ([4], [5], [6]), elastomers [7] and wood [8]. A conceptual diagram showing the constituent parts of a general composite material model is shown in figure 1-1.

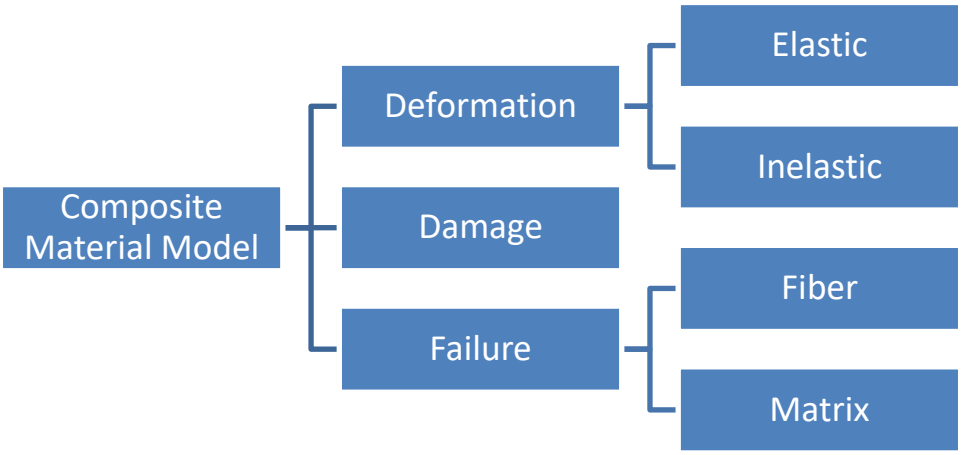

Figure 1-1. Components of a general, fiber-reinforced composite material model

Researchers have used several approaches to developing constitutive models for composites. The continuum mechanics approaches can be categorized into the following groups [9] –

a) nonlinear elasticity theories, e.g., [10]
b) damage theories coupled with elasticity, e.g., [11], [12], [13], and [14]
c) classical incremental plasticity theories, e.g., [9], [15], and [16]
d) endochronic plasticity theory, e.g., [17]

The approach used in this paper falls under the category of incremental plasticity theory. Sun and Chen [15] developed a plasticity-based material model for composites which simulates the nonlinear behavior of fiber composites relatively accurately. However, this model was designed to be used with unidirectional, carbon fiber-based composites under in-plane loading conditions and has limited ability to be extended to more complex fiber architectures (such as textile composites) and material systems.

A rate-independent, plasticity-based constitutive model was developed by Vaziri et al. [9] for fiber reinforced composites (FRC) that is able to predict the response of a single FRC layer for unidirectional and bidirectional fiber orientations, from elastic and plastic response to brittle and ductile failure. However, this model is restricted to two-dimensional applications due to its plane stress assumption and does not account for a reduction in the unloading/reloading modulus (associated with damage of the composite) during the plastic response. Griffin et al. [16] use Hill's orthotropic yield criterion and incremental plastic flow theory. Thermal effects are considered, but other

considerations are missing – asymmetry in tension-compression behavior, ability to handle rate effects, damage and failure, etc. Other composite material models have been developed that are only applicable for a well-defined class of problems such as short-fiber reinforced composites [18] or ceramic matrix composites [19].

Models can be created at different length scales which incorporate one or more of the three specified components (deformation, damage, and failure). For example, in Boutaous et al. [20], an elastoplastic damage model is developed to model the behavior of laminated composites up until fracture. Damage for each elementary constituent is accounted for at the micro level and a complete model at the meso-scale is obtained by applying a homogenization method such that the model can be implemented in a finite element program. This approach, while attractive to understand the constituent behavior of composites, requires far too much computational effort to model impact problems aside from other limitations in the framework.

While there is a need for a robust, efficient, accurate, general purpose constitutive material model for impact that can be used across a large range of composite material classes and fiber architectures, this development work is a challenging task given the wide array of performance conditions needed to capture the behavior accurately. In particular, there are several features of current composite impact models which limit their predictive capability. Existing models often require correlating parameters such as the failure strain based on structural level impact tests, which significantly limits the use of these methods as predictive tools. Input to some material models generally consists of point-wise properties (such as a specified failure stress or failure strain) that lead to curve fit approximations to the material stress-strain curves. This type of approach leads either to models with only a few parameters, which provide a crude approximation at best to the actual stress-strain curve, or to models with many parameters, which require a large number of complex tests to characterize.

Since one can think of nonlinear deformation in composites as being composed of a mixture of deformation and damage mechanisms, the present approach is to partition the nonlinear response into a plasticity-based deformation model (the focus of this paper) and a stiffness reduction due to damage (to be handled as a part of future work), with tabulated input for material behavior. Such a modeling approach, in which a plasticity-based deformation model is combined with a damage model [21], can provide some advantages. First, strain rate effects, critical for impact, can be accounted for in a more straightforward manner. Strain rate effects are also more likely to be closely related to deformation mechanisms than damage mechanisms. Second, this improved approach is driven by tabulated data, in which the material stress-strain curves are explicitly entered into the model in a discretized form. The discretized data, obtained from a well-defined straightforward set of experiments, allows the complete stress-strain response of the material to be accurately defined. For example, since impact is inherently a three-dimensional problem, being able to characterize and use the through-thickness material behavior becomes an important component of any material model. These curves can be functions of temperature and strain rates and can be handled

naturally within the constitutive model. Third, incorporation of damage and failure predictions is straightforward and would require additional experimental input.

1.2 A SHORT HISTORY OF THE DEVELOPMENT OF MAT213

A proposal was submitted to the FAA Catastrophic Failure Research Program in January 2012 for a new FAA Cooperative Agreement titled “Composite Material Model for Impact Analysis”. The proposal’s major objective was to provide support to the FAA and NASA to develop a new composite material model. NASA Glenn Research Center (GRC) was a partner in the proposal and agreed to provide in-kind support for the modeling and testing activities in support of the research. A secondary objective of the proposal was to provide support to the LS-DYNA Aerospace Working Group (AWG) and to continue to support fabric modeling development as needed. The AWG is a partnership of federal agencies, industry, and academia working together to assure the quality of aerospace modeling in LS-DYNA through the publication of test cases and modeling guidelines. This initial proposal was for a period of performance of 51 months segmented into four phases (Phase I was for 15 months, while Phases II-IV were for 12 months each). A roadmap was constructed to guide the research work and is shown in figure 1-2.

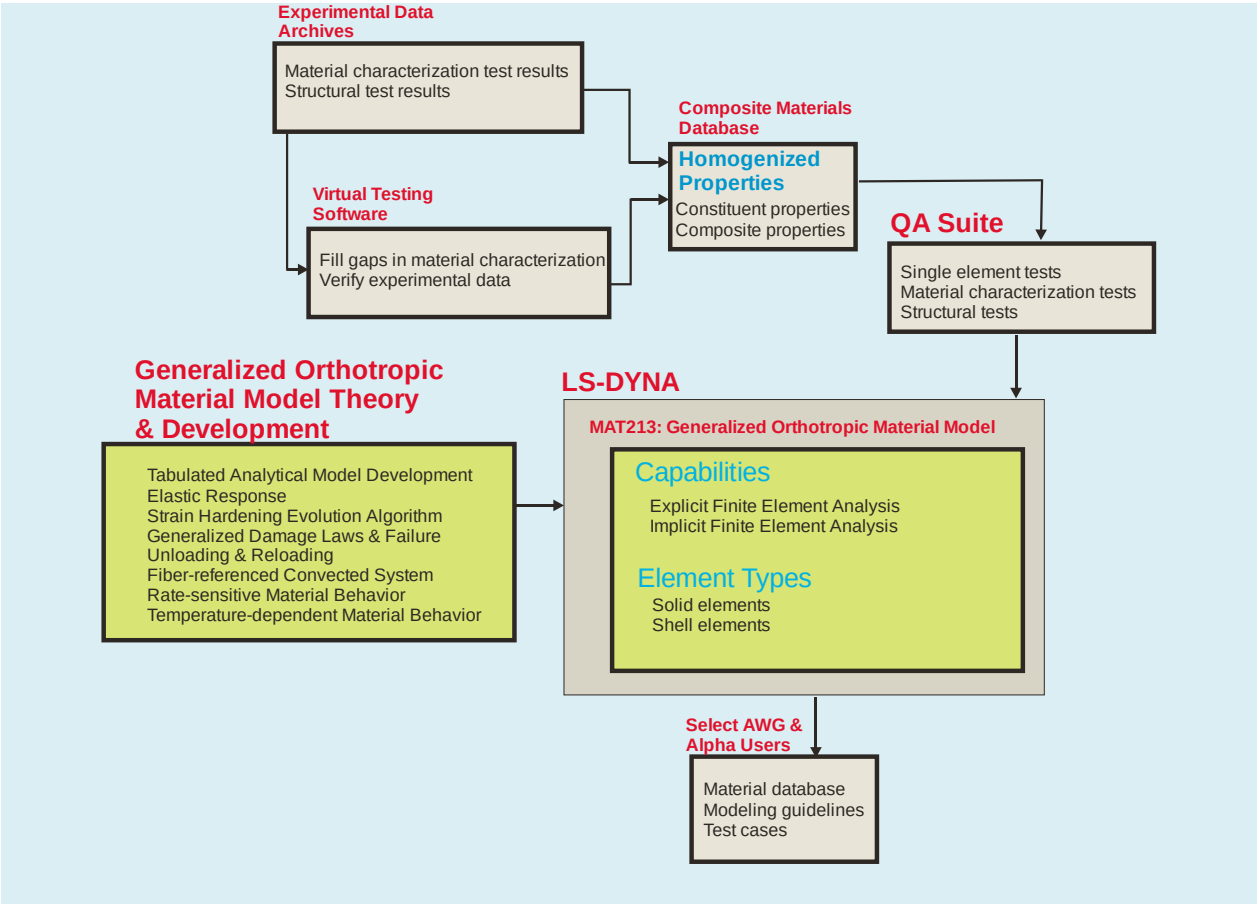

Figure 1-2. Overall Research Project Roadmap

At that time, a comprehensive list of the available material models in LS-DYNA was constructed and the strengths and weaknesses were identified. The goal was to overcome the weaknesses and add missing features so that one orthotropic material model could be developed for a wide variety of composite architectures.

- *MAT_2*: Orthotropic or anisotropic elastic; for the anisotropic version (solids only) constitutive matrix is input; shells or solids; no plastic-like deformation; no damage; no erosion; no rate sensitivity; no temperature sensitivity.

- *MAT_22*: Chang-Chang failure model, linear elastic in longitudinal and transverse response up to failure; nonlinear shear with one curve fit parameter; shells or solids; no plastic-like deformation; no damage; no erosion; no rate sensitivity; no temperature sensitivity.

- *MAT_54-55*: Chang-Chang or Tsai-Wu failure model, selective property degradation using Matzenmiller in compression; shell or solids; no plastic-like deformation; no erosion; no rate sensitivity; no temperature sensitivity.

- *MAT_58*: Matzenmiller continuum damage mechanics formulation with failure stress and strain-based curve fit; shells only; no plastic-like deformation; effective strain erosion; rate sensitivity (new); no temperature sensitivity.

- *MAT_158*: MAT_58 with isotropic rate dependence based on viscoelastic Prony series; shells only; no plastic-like deformation; effective strain erosion; no temperature sensitivity.

- *MAT_161-162*: Hashin stress-based initial failure with Matzenmiller damage after; solids only; no plastic-like deformation; volume strain erosion; modulus and strength scaled by strain rate; no temperature sensitivity; non-LSTC source.

- *MAT_219*: CODAM model with strain-based damage initiation and damage accumulation based on failure mode defined by many parameters; shell or solids; no plastic-like deformation; max principle strain erosion; no rate sensitivity; no temperature sensitivity.

- *MAT_221*: Marie damage model and failure defined by many parameters; solids only; no plastic-like deformation; damage-based erosion; no rate sensitivity; no temperature sensitivity.

- *MAT_261*: Pinho fracture model with separate damage evolution based on failure mode; shells or solids; no plastic-like deformation; no erosion; no rate sensitivity; no temperature sensitivity.

- *MAT_262*: Camanho fracture model with energy approach used to generate damage functions in various coordinate directions; shells or solids; no plastic-like deformation; no erosion; no rate sensitivity; no temperature sensitivity.

After nearly three years of effort, the NASA Advanced Composites Program was initiated. Arizona State University (ASU) teamed with George Mason University to expand the model development beyond the effort under the FAA Grant. The NASA contract's period of performance was Oct 1, 2015 through September 30, 2018. This contract complements the FAA-sponsored work as well as the work that was proposed for the FAA supplemental grant. A new FAA grant, 17-G-005, was awarded to ASU in June 2017 to continue the work through July 2020.

1.3 SCOPE OF WORK

The NASA-sponsored research work has the following tasks. This report covers details of the deformation, damage and failure sub-models as well as results from verification and validation tests as outlined in Tasks 4.2.1, 4.2.2, 4.3.1, 4.3.2, 4.3.3, and 4.3.4. Tasks 4.1.1, 4.1.2, 4.1.3, and 4.1.4 are presented in a companion report [22]. Tasks 4.4.1, 4.4.2, and 4.5.1 are presented in a companion report [23].

- *Task 4.1.1*: Experiments to Obtain T800-F3900 Composite Properties (Mass density, 1-Direction Tension, 2-Direction Tension, 1-2 Plane Shear, and 1-2 Plane 45° Off-Axis Tension test data).

- *Task 4.1.2*: Experiments to Obtain T800-F3900 Composite Properties (3-Direction Tension, 1-Direction Compression, 2-Direction Compression, 3-Direction Compression, 2-3 Plane Shear, 1-3 Plane Shear, 2-3 Plane 45° Off-Axis Compression, and 1-3 Plane 45° Off-Axis Compression test data).

- *Task 4.1.3*: Damage Characterization Test Plan.

- *Task 4.1.4*: Damage Characterization Tests.

- *Task 4.2.1*: Algorithm for Damage and Failure.

- *Task 4.2.2*: Implement Damage and failure into MAT213.

- *Task 4.3.1*: Verification of Deformation, Damage, and Failure Models.

- *Task 4.3.2*: Identify and Implement MAT213 (Improvements).

- *Task 4.3.3*: Validation of MAT213 (Simulation of Ballistic Impact Tests).

- *Task 4.3.4*: Identify and Implement MAT213 Improvements.

- *Task 4.4.1*: Probabilistic-Based Analysis (Identify Sensitive Variables and Distribution, Develop Theory and Algorithm).

- *Task 4.4.2*: Implement Probabilistics into MAT213.

- *Task 4.5.1*: Validate Probabilistic Methodology (Repeat selected studies from task 4.3, Document Improvements Obtained by Utilizing Probabilistic Methodology).

The deformation sub-model is discussed in chapter 2 with emphasis on the theory, implementation, and verification details. This is followed by the damage sub-model in chapter 3 and the failure sub-model in chapter 4. Chapter 5 is devoted to validation tests involving three impact tests at increasing velocities. The report concludes with a list of accomplishments and scope of the ongoing and future work.

2. DEFORMATION SUB-MODEL

In this chapter, the deformation sub-model is introduced. The theoretical background, implementation details, and model verification are all provided.

2.1 THEORETICAL BACKGROUND

The material deformation law in the model can be used to compute the elastic and permanent deformations of a composite with a full three-dimensional implementation suitable for solid and shell elements. Current development of the model includes a complete elasto-plastic deformation model, with strain rate and temperature effects, and damage, with failure capabilities to be added later. A quadratic function is used to define the yield surface. The Tsai-Wu failure criterion [24] has been generalized and is used as the orthotropic three-dimensional yield function for the plasticity model as:

$$f(\sigma) = a + \begin{pmatrix} F_1 & F_2 & F_3 & 0 & 0 & 0 \end{pmatrix} \begin{bmatrix} \sigma_{11} \\ \sigma_{22} \\ \sigma_{33} \\ \sigma_{12} \\ \sigma_{23} \\ \sigma_{31} \end{bmatrix} + \begin{bmatrix} \sigma_{11} \\ \sigma_{22} \\ \sigma_{33} \\ \sigma_{12} \\ \sigma_{23} \\ \sigma_{31} \end{bmatrix}^T \begin{bmatrix} F_{11} & F_{12} & F_{13} & 0 & 0 & 0 \\ F_{12} & F_{22} & F_{23} & 0 & 0 & 0 \\ F_{13} & F_{23} & F_{33} & 0 & 0 & 0 \\ 0 & 0 & 0 & F_{44} & 0 & 0 \\ 0 & 0 & 0 & 0 & F_{55} & 0 \\ 0 & 0 & 0 & 0 & 0 & F_{66} \end{bmatrix} \begin{bmatrix} \sigma_{11} \\ \sigma_{22} \\ \sigma_{33} \\ \sigma_{12} \\ \sigma_{23} \\ \sigma_{31} \end{bmatrix} \qquad 2.1$$

where $a = -1$, the 1-2-3 subscripts refer to the principal material directions, σ_{ii} represents the stresses, and the F_{ii} terms are the yield function coefficients based on the current yield stress values in the various coordinate directions. The use of varying yield function coefficients allows for evolution of the yield surface, and hardening can be precisely defined in each of the material directions. The normal coefficient values can be determined by simplifying the yield function for the case of unidirectional tension and compression as:

$$\begin{aligned} F_i \sigma_{ii}^T + F_{ii} \left(\sigma_{ii}^T \right)^2 &= 1 \\ F_i \sigma_{ii}^C + F_{ii} \left(\sigma_{ii}^C \right)^2 &= 1 \end{aligned} \quad \text{for } i = 1,2,3 \qquad 2.2$$

where F_i and F_{ii} are the linear and nonlinear coefficients, respectively. Assuming the sign convention that σ^C is always negative, the two expressions in equation 2.2 can then be used to solve for the uniaxial yield coefficients, in terms of the compressive and tensile yield stresses as:

$$F_i = \frac{1}{\sigma_{ii}^T} - \frac{1}{\sigma_{ii}^C}$$
$$F_{ii} = \frac{1}{\sigma_{ii}^T \sigma_{ii}^C} \qquad 2.3$$

The shear coefficient values can be determined in the same manner, by simplifying the yield function for the case of shear loading in each coordinate direction as:

$$F_{ii}\sigma_{ij}^2 = 1$$
$$F_{kk} = \frac{1}{\sigma_{ij}^2} \quad \text{for } i, j = 1,2,3, k = i+3 \qquad 2.4$$

where F_{ii} are the yield function coefficients and σ_{ij} are the shear stresses. The equations can be written with the uniaxial coefficients as:

$$F_1 = \frac{1}{\sigma_{11}^T} - \frac{1}{\sigma_{11}^C} \qquad F_{11} = \frac{1}{\sigma_{11}^T \sigma_{11}^C} \qquad F_{44} = \frac{1}{\sigma_{12}^2}$$
$$F_2 = \frac{1}{\sigma_{22}^T} - \frac{1}{\sigma_{22}^C} \qquad F_{22} = \frac{1}{\sigma_{22}^T \sigma_{22}^C} \qquad F_{55} = \frac{1}{\sigma_{23}^2} \qquad 2.5$$
$$F_3 = \frac{1}{\sigma_{33}^T} - \frac{1}{\sigma_{33}^C} \qquad F_{33} = \frac{1}{\sigma_{33}^T \sigma_{33}^C} \qquad F_{66} = \frac{1}{\sigma_{31}^2}$$

The stress components of the yield function coefficients correspond to the current yield stresses associated with the normal and shear tests (the methods of determining these values are discussed below), where the superscript *T* indicates the tensile yield stress and the superscript *C* denotes the absolute value of the compressive yield stress. The off-axis coefficients, required to capture the interactive effects in the yield stresses, can be determined using the results of 45° off-axis tests in various coordinate directions. For example, consider a uniaxial 45° off-axis tensile test of a unidirectional composite, or any uniaxial tensile test performed at a 45° angle from the longitudinal (1-direction) material axis in the 1-2 plane, for a multi-ply laminated or textile composite. The stresses in the local material axes can be determined using the stress transformation equations [25] and calculated using the following equations:

$$\sigma_{11} = 0.5\sigma^{45}$$
$$\sigma_{22} = 0.5\sigma^{45} \qquad 2.6$$
$$\sigma_{12} = -0.5\sigma^{45}$$

The σ^{45} term in equation 2.6 is the uniaxial yield stress in the structural loading direction obtained from the 45° off-axis tensile test. If the uniaxial yield stresses correspond to a compressive test, these will have opposite signs. Substituting equation

2.6 into equation 2.1 and solving results in an expression for the off-axis yield function coefficient, F_{12} as:

$$F_{12} = \frac{2}{\left(\sigma_{12}^{45}\right)^2} - \frac{F_1 + F_2}{\sigma_{12}^{45}} - \frac{1}{2}\left(F_{11} + F_{22} + F_{44}\right) \tag{2.7}$$

Expressions for the other two off-axis yield coefficients, F_{13} and F_{23}, can be determined using similar procedures for 45° off-axis tests in the 1-3 and 2-3 planes, with the expressions for the yield coefficients defined as:

$$F_{23} = \frac{2}{\left(\sigma_{23}^{45}\right)^2} - \frac{F_2 + F_3}{\sigma_{23}^{45}} - \frac{1}{2}\left(F_{22} + F_{33} + F_{55}\right) \tag{2.8}$$

$$F_{13} = \frac{2}{\left(\sigma_{13}^{45}\right)^2} - \frac{F_1 + F_3}{\sigma_{13}^{45}} - \frac{1}{2}\left(F_{11} + F_{33} + F_{66}\right) \tag{2.9}$$

The off-axis yield function coefficients corresponding to compressive testing are as follows:

$$F_{12} = \frac{2}{\left(\sigma_{12}^{45}\right)^2} + \frac{F_1 + F_2}{\sigma_{12}^{45}} - \frac{1}{2}\left(F_{11} + F_{22} + F_{44}\right) \tag{2.10}$$

$$F_{23} = \frac{2}{\left(\sigma_{23}^{45}\right)^2} + \frac{F_2 + F_3}{\sigma_{23}^{45}} - \frac{1}{2}\left(F_{22} + F_{33} + F_{55}\right) \tag{2.11}$$

$$F_{13} = \frac{2}{\left(\sigma_{13}^{45}\right)^2} + \frac{F_1 + F_3}{\sigma_{13}^{45}} - \frac{1}{2}\left(F_{11} + F_{33} + F_{66}\right) \tag{2.12}$$

A non-associative flow rule is used to define the evolution of the plastic strain components, with the plastic potential for the flow rule calculated as:

$$h = \sqrt{H_{11}\sigma_{11}^2 + H_{22}\sigma_{22}^2 + H_{33}\sigma_{33}^2 + 2H_{12}\sigma_{11}\sigma_{22} + 2H_{23}\sigma_{22}\sigma_{33} + 2H_{31}\sigma_{33}\sigma_{11} + H_{44}\sigma_{12}^2 + H_{55}\sigma_{23}^2 + H_{66}\sigma_{31}^2} \tag{2.13}$$

where the H_{ij} terms are the independent flow rule coefficients assumed to be constant, and σ_{jj} are the current stress values. The procedure for determining the flow rule coefficient values is discussed later. In order to ensure convexity of the flow surface, the flow rule coefficients must satisfy specific conditions [26]. A general quadratic failure/yield function, similar to the Tsai-Wu criterion used for the yield surface in this model, can be written as:

$$f(\boldsymbol{\sigma}) = a + \mathbf{b}^T\boldsymbol{\sigma} + \boldsymbol{\sigma}^T\mathbf{P}\boldsymbol{\sigma} \tag{2.14}$$

where $\boldsymbol{\sigma}^T = (\sigma_{11}, \sigma_{22}, \sigma_{33}, \sigma_{12}, \sigma_{23}, \sigma_{31})$, a is a scalar, $\mathbf{b}$ is a vector, and $\mathbf{P}$ is a matrix. In general, $\mathbf{b}$ is comprised of six independent coefficients, whereas $\mathbf{P}$ contains 36 coefficients, 21 of which are independent due to symmetry. The flow rule can be written in the form of the quadratic function as equation 2.15:

$$h^2 = H_{11}\sigma_{11}^2 + H_{22}\sigma_{22}^2 + H_{33}\sigma_{33}^2 + 2H_{12}\sigma_{11}\sigma_{22} + 2H_{23}\sigma_{22}\sigma_{33} + 2H_{31}\sigma_{33}\sigma_{11} + H_{44}\sigma_{12}^2 + H_{55}\sigma_{23}^2 + H_{66}\sigma_{31}^2$$

$$h^2 = \begin{bmatrix}\sigma_{11}\\ \sigma_{22}\\ \sigma_{33}\\ \sigma_{12}\\ \sigma_{23}\\ \sigma_{31}\end{bmatrix}^T \begin{bmatrix} H_{11} & H_{12} & H_{13} & 0 & 0 & 0\\ H_{12} & H_{22} & H_{23} & 0 & 0 & 0\\ H_{13} & H_{23} & H_{33} & 0 & 0 & 0\\ 0 & 0 & 0 & H_{44} & 0 & 0\\ 0 & 0 & 0 & 0 & H_{55} & 0\\ 0 & 0 & 0 & 0 & 0 & H_{66}\end{bmatrix} \begin{bmatrix}\sigma_{11}\\ \sigma_{22}\\ \sigma_{33}\\ \sigma_{12}\\ \sigma_{23}\\ \sigma_{31}\end{bmatrix} = \boldsymbol{\sigma}^T\mathbf{H}\boldsymbol{\sigma} \tag{2.15}$$

with $\mathbf{H}$ being the matrix of flow law coefficients and representing $\mathbf{P}$ from the general form of the quadratic yield function. To ensure convexity of the quadratic function, the coefficients $\mathbf{b}$ and $\mathbf{P}$ must have constraints. Assuming two distinct stress states $\boldsymbol{\sigma}$ and $\boldsymbol{\sigma}'$, the convex combination of the two vectors is:

$$\bar{\boldsymbol{\sigma}} = \alpha\boldsymbol{\sigma} + (1-\alpha)\boldsymbol{\sigma}' \quad 0 \le \alpha \le 1 \tag{2.16}$$

and to ensure convexity of f, must satisfy the inequality:

$$f(\bar{\boldsymbol{\sigma}}) \le \alpha f(\boldsymbol{\sigma}) + (1-\alpha) f(\boldsymbol{\sigma}') \tag{2.17}$$

where the yield function value determined at the convex combination of the two stress states must be within the convex combination of the yield function values evaluated at each stress state (remain within the convex hull). Thus, substituting equation 2.16 into equation 2.17, the inequality, equation 2.17 is reduced to the following equations:

$$a + \mathbf{b}^T\bar{\boldsymbol{\sigma}} + \bar{\boldsymbol{\sigma}}^T\mathbf{P}\bar{\boldsymbol{\sigma}} \le \alpha\left[a + \mathbf{b}^T\boldsymbol{\sigma} + \boldsymbol{\sigma}^T\mathbf{P}\boldsymbol{\sigma}\right] + (1-\alpha)\left[a + \mathbf{b}^T\boldsymbol{\sigma}' + \boldsymbol{\sigma}'^T\mathbf{P}\boldsymbol{\sigma}'\right]$$

or

$$\begin{aligned} a + \mathbf{b}^T\left[\alpha\boldsymbol{\sigma} + (1-\alpha)\boldsymbol{\sigma}'\right] & \\ + \left[\alpha\boldsymbol{\sigma} + (1-\alpha)\boldsymbol{\sigma}'\right]^T\mathbf{P}\left[\alpha\boldsymbol{\sigma} + (1-\alpha)\boldsymbol{\sigma}'\right] & \le \begin{aligned}&\alpha\left[a + \mathbf{b}^T\boldsymbol{\sigma} + \boldsymbol{\sigma}^T\mathbf{P}\boldsymbol{\sigma}\right]\\ &+ (1-\alpha)\left[a + \mathbf{b}^T\boldsymbol{\sigma}' + \boldsymbol{\sigma}'^T\mathbf{P}\boldsymbol{\sigma}'\right]\end{aligned} \end{aligned}$$

or

$$\begin{aligned} a+\alpha\mathbf{b}^T\boldsymbol{\sigma}+\mathbf{b}^T\boldsymbol{\sigma}'-\alpha\mathbf{b}^T\boldsymbol{\sigma}' \\ +\left[\alpha\boldsymbol{\sigma}^T+\boldsymbol{\sigma}'^T-\alpha\boldsymbol{\sigma}'^T\right]\left[\alpha\mathbf{P}\boldsymbol{\sigma}+\mathbf{P}\boldsymbol{\sigma}'-\alpha\mathbf{P}\boldsymbol{\sigma}'\right] \end{aligned} \leq \begin{aligned} \alpha a+\alpha\mathbf{b}^T\boldsymbol{\sigma}+\alpha\boldsymbol{\sigma}^T\mathbf{P}\boldsymbol{\sigma} \\ +a+\mathbf{b}^T\boldsymbol{\sigma}'+\boldsymbol{\sigma}'^T\mathbf{P}\boldsymbol{\sigma}'-\alpha a-\alpha\mathbf{b}^T\boldsymbol{\sigma}'-\alpha\boldsymbol{\sigma}'^T\mathbf{P}\boldsymbol{\sigma}' \end{aligned}$$

or

$$\begin{aligned} \alpha\boldsymbol{\sigma}^T\mathbf{P}\boldsymbol{\sigma}'-\alpha^2\boldsymbol{\sigma}^T\mathbf{P}\boldsymbol{\sigma}'+\alpha\boldsymbol{\sigma}'^T\mathbf{P}\boldsymbol{\sigma}-\alpha\boldsymbol{\sigma}'^T\mathbf{P}\boldsymbol{\sigma}'-\alpha^2\boldsymbol{\sigma}'^T\mathbf{P}\boldsymbol{\sigma}-\alpha^2\boldsymbol{\sigma}'^T\mathbf{P}\boldsymbol{\sigma}'\leq 0 \\ -\alpha\left[-\boldsymbol{\sigma}^T\mathbf{P}\boldsymbol{\sigma}'+\alpha\boldsymbol{\sigma}^T\mathbf{P}\boldsymbol{\sigma}'-\boldsymbol{\sigma}'^T\mathbf{P}\boldsymbol{\sigma}+\boldsymbol{\sigma}'^T\mathbf{P}\boldsymbol{\sigma}'+\alpha\boldsymbol{\sigma}'^T\mathbf{P}\boldsymbol{\sigma}+\alpha\boldsymbol{\sigma}'^T\mathbf{P}\boldsymbol{\sigma}'\right]\leq 0 \\ -\boldsymbol{\sigma}^T\mathbf{P}\boldsymbol{\sigma}'+\alpha\boldsymbol{\sigma}^T\mathbf{P}\boldsymbol{\sigma}'-\boldsymbol{\sigma}'^T\mathbf{P}\boldsymbol{\sigma}+\boldsymbol{\sigma}'^T\mathbf{P}\boldsymbol{\sigma}'+\alpha\boldsymbol{\sigma}'^T\mathbf{P}\boldsymbol{\sigma}+\alpha\boldsymbol{\sigma}'^T\mathbf{P}\boldsymbol{\sigma}'\geq 0 \\ \left(1-\alpha\right)\left(\boldsymbol{\sigma}-\boldsymbol{\sigma}'\right)^T\mathbf{P}\left(\boldsymbol{\sigma}-\boldsymbol{\sigma}'\right)\geq 0 \end{aligned}$$

or

$$\left(\boldsymbol{\sigma}-\boldsymbol{\sigma}'\right)^T\mathbf{P}\left(\boldsymbol{\sigma}-\boldsymbol{\sigma}'\right)\geq 0 \qquad 2.18$$

for all $\boldsymbol{\sigma}$ and $\boldsymbol{\sigma}'$. This implies that $\mathbf{P}$ must be positive semidefinite, meaning the diagonal components of $\mathbf{P}$ must be nonnegative

$$\mathbf{P}_{ii}\geq 0 \quad i=1,2,...,6 \qquad 2.19$$

and the off-diagonal components of $\mathbf{P}$ must satisfy the following condition.

$$\mathbf{P}_{ii}\mathbf{P}_{jj}-\mathbf{P}_{ij}^2\geq 0 \quad i=1,2,...,6, \quad j=i+1,...,6 \qquad 2.20$$

The two constraints in equations 2.19 and 2.20 can then be written in terms of the flow law coefficients as:

$$\begin{aligned} &H_{11}\geq 0 \\ &H_{22}\geq 0 \\ &H_{33}\geq 0 \\ &H_{44}\geq 0 \\ &H_{55}\geq 0 \\ &H_{66}\geq 0 \\ &H_{11}H_{22}-H_{12}^2\geq 0 \\ &H_{33}H_{22}-H_{23}^2\geq 0 \\ &H_{11}H_{33}-H_{31}^2\geq 0 \end{aligned} \qquad 2.21$$

with the coefficients determined using a procedure described later. The plastic potential function in equation 2.13 is used in the flow law with the usual normality hypothesis of

classical plasticity assumed to apply, where the plasticity variable, λ, is a scalar plastic multiplier [27]. Thus, the plastic strains are defined in terms of the plastic multiplier, flow potential, and stresses as:

$$
\begin{aligned}
\dot{\boldsymbol{\varepsilon}}^{p} &= \dot{\lambda}\frac{\partial h}{\partial \boldsymbol{\sigma}} \\
\dot{\varepsilon}_{11}^{p} &= \frac{\dot{\lambda}}{2h}\left(2H_{11}\sigma_{11} + 2H_{12}\sigma_{22} + 2H_{13}\sigma_{33}\right) \\
\dot{\varepsilon}_{22}^{p} &= \frac{\dot{\lambda}}{2h}\left(2H_{12}\sigma_{11} + 2H_{22}\sigma_{22} + 2H_{23}\sigma_{33}\right) \\
\dot{\varepsilon}_{33}^{p} &= \frac{\dot{\lambda}}{2h}\left(2H_{13}\sigma_{11} + 2H_{23}\sigma_{22} + 2H_{33}\sigma_{33}\right) \\
\dot{\varepsilon}_{12}^{p} &= \frac{\dot{\lambda}}{2h}H_{44}\sigma_{12} \\
\dot{\varepsilon}_{23}^{p} &= \frac{\dot{\lambda}}{2h}H_{55}\sigma_{23} \\
\dot{\varepsilon}_{31}^{p} &= \frac{\dot{\lambda}}{2h}H_{66}\sigma_{31}
\end{aligned}
\qquad 2.22
$$

where ε_{jj}^{p} are the individual plastic strain components, with the shear components representing tensorial, not engineering, strain. Using the expressions for the plastic strains, in equation 2.22, and defining the "plastic Poisson's ratios" in terms of these plastic strains, the coefficients of the flow potential function, H_{ij}, can be defined as (uniaxial testing in the 1-direction):

$$
\begin{aligned}
&\sigma_{11} \neq 0 \\
&\nu_{12}^{p} = -\frac{\dot{\varepsilon}_{22}^{p}}{\dot{\varepsilon}_{11}^{p}} = -\frac{H_{12}}{H_{11}} \\
&\nu_{13}^{p} = -\frac{\dot{\varepsilon}_{33}^{p}}{\dot{\varepsilon}_{11}^{p}} = -\frac{H_{13}}{H_{11}}
\end{aligned}
\qquad 2.23
$$

From uniaxial testing in the 2-direction, we have:

$$
\begin{aligned}
&\sigma_{22} \neq 0 \\
&\nu_{21}^{p} = -\frac{\dot{\varepsilon}_{11}^{p}}{\dot{\varepsilon}_{22}^{p}} = -\frac{H_{12}}{H_{22}} \\
&\nu_{23}^{p} = -\frac{\dot{\varepsilon}_{33}^{p}}{\dot{\varepsilon}_{22}^{p}} = -\frac{H_{23}}{H_{22}}
\end{aligned}
\qquad 2.24
$$

From uniaxial testing in the 3-direction, we have:

$$\sigma_{33} \neq 0$$
$$\nu_{32}^{p} = -\frac{\dot{\varepsilon}_{22}^{p}}{\dot{\varepsilon}_{33}^{p}} = -\frac{H_{23}}{H_{33}} \qquad 2.25$$
$$\nu_{31}^{p} = -\frac{\dot{\varepsilon}_{11}^{p}}{\dot{\varepsilon}_{33}^{p}} = -\frac{H_{13}}{H_{33}}$$

which are useful in creating a procedure for characterizing the coefficient values.

The general shapes of the yield and flow surfaces, for a plane stress case, are shown in Figure 2-1 and Figure 2-2, respectively (values are set for example only). Note that:

$$F_1 = -0.75,\ F_2 = 3.0,\ F_{11} = 0.5,\ F_{22} = 2.0,\ F_{12} = -0.5,\ F_{44} = 5$$
$$H_{11} = H_{22} = 1.0,\ H_{12} = -0.101,\ H_{44} = 3.0$$

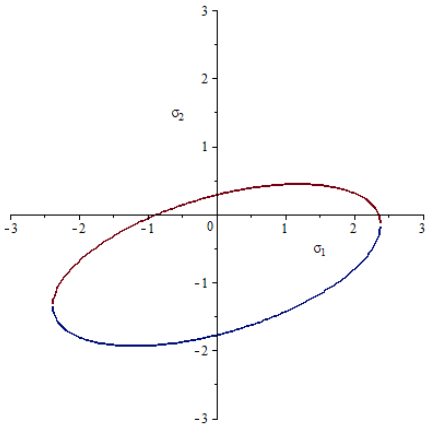

(a)

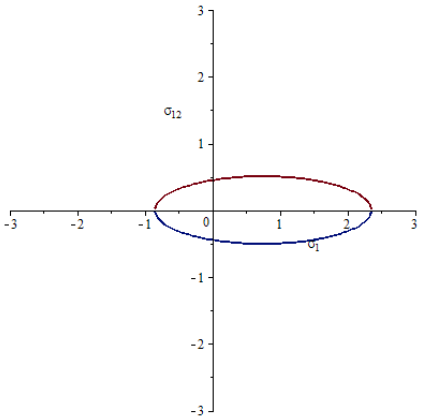

(b)

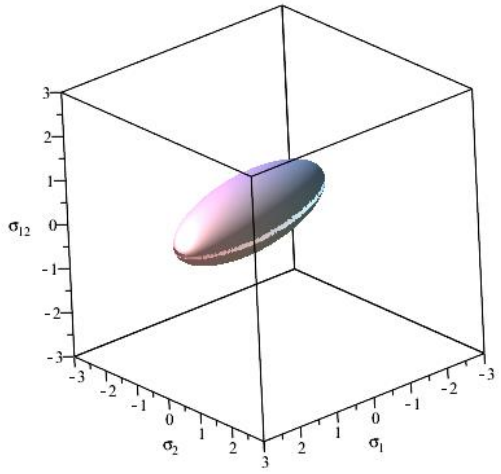

(c)

Figure 2-1. Example yield surface for plane stress case (a) 2D: $\sigma_1 - \sigma_2$ plane, (b) 2D: $\sigma_1 - \sigma_{12}$ plane, (c) 3D plot

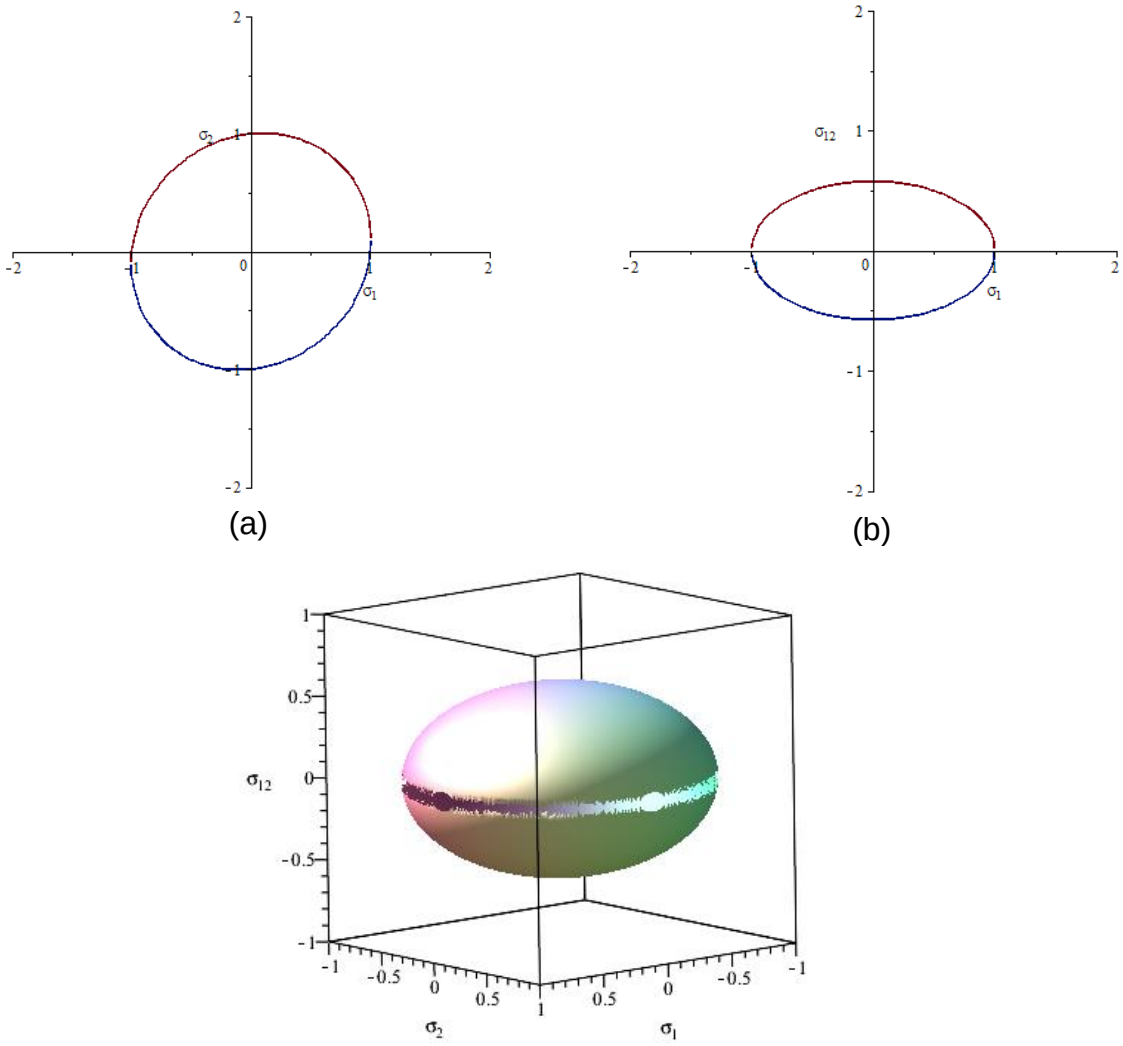

(a) (b)

(c)

Figure 2-2. Example flow surface for plane stress case (a) 2D: $\sigma_1 - \sigma_2$ plane, (b) 2D: $\sigma_1 - \sigma_{12}$ plane, (c) 3D plot

At this point, it is important to note that the flow law contains only the quadratic terms, whereas the yield function also includes the linear terms and hence can differentiate between tension and compression, which the flow law cannot. Including the linear terms in flow law would make plastic Poisson's ratio dependent on stress, and in turn the flow law coefficients. For example, the uniaxial plastic strains would be defined as:

$$\dot{\varepsilon}_{11}^{p} = \frac{\dot{\lambda}}{2h}\left(H_1 + 2H_{11}\sigma_{11} + 2H_{12}\sigma_{22} + 2H_{13}\sigma_{33}\right)$$
$$\dot{\varepsilon}_{22}^{p} = \frac{\dot{\lambda}}{2h}\left(H_2 + 2H_{12}\sigma_{11} + 2H_{22}\sigma_{22} + 2H_{23}\sigma_{33}\right) \qquad 2.26$$
$$\dot{\varepsilon}_{33}^{p} = \frac{\dot{\lambda}}{2h}\left(H_3 + 2H_{13}\sigma_{11} + 2H_{23}\sigma_{22} + 2H_{33}\sigma_{33}\right)$$

where H_i would be the linear flow law coefficients. Thus, considering a uniaxial test in the 1-direction, the plastic Poisson's ratios would be defined as:

$$\sigma_{11} \neq 0$$
$$\nu_{12}^{p} = -\frac{\dot{\varepsilon}_{22}^{p}}{\dot{\varepsilon}_{11}^{p}} = -\frac{H_{12} + H_2}{H_{11} + H_1}$$
$$\nu_{13}^{p} = -\frac{\dot{\varepsilon}_{33}^{p}}{\dot{\varepsilon}_{11}^{p}} = -\frac{H_{13} + H_3}{H_{11} + H_1} \qquad 2.27$$

This stress dependency, needed to solve for the additional parameters on the flow law coefficients, would most likely result in erratic behavior of the model. The flow law coefficients could be assumed to vary based on the current stress and strain state, similar to the yield function coefficients, but would require the development of conditions to define the evolution of the flow law, which may be difficult to construct using experimental data. This might include normalizing the flow rule coefficients with respect to a common variable, similar to the effective plastic strain used for the yield surface. In doing so, the plastic Poisson's ratios used to calculate the flow rule coefficients in equation 2.27, would need to be defined as a function of the effective plastic strain, and the flow rule coefficients would be calculated based on the varying values of the plastic Poisson's ratios (the following theory and implementation assumes constant plastic Poisson's ratios and therefore constant flow rule coefficients).

Expressions for the effective stress and effective plastic strain can now be written using the flow law and the principle of the equivalence of plastic work [27]. Taking a vector product of the stress and plastic strain tensors results in the plastic potential function h being multiplied by the plastic multiplier λ. The principle of the equivalence of plastic work defines the vector product of the stress and the plastic strain to be equal to the product of the effective stress and effective plastic strain. Therefore, the effective stress can be defined by the plastic potential function h and the effective plastic strain can be defined by the plastic multiplier λ. This process can be shown as:

$$\dot{W}_p = \boldsymbol{\sigma} : \dot{\boldsymbol{\varepsilon}}^{p} = \boldsymbol{\sigma} : \dot{\lambda}\frac{\partial h}{\partial \boldsymbol{\sigma}} = h\dot{\lambda} = \sigma_e : \dot{\varepsilon}_e^{p}, \qquad 2.28$$

where $\dot{W}_p$ is the plastic work, σ_e is the effective stress, and ε_e^p is the effective plastic strain.

It is common, in plasticity constitutive equations, to use analytical functions to define the evolution of stresses as a function of the (effective) plastic strain components in order to compute the current value of the yield stresses required to evaluate the yield function. Alternatively, tabulated stress-strain curves can be used to track the changes of the yield stresses in each coordinate direction.

In this dissertation, experimental stress versus plastic strain curves generated for each yield stress value (uniaxial tension and compression curves in each of the normal directions (1-2-3)), shear curves in each of the shear directions, 1-2, 2-3, 3-1, and 45°, off-axis tension curves (in the 1-2, 2-3, and 3-1 planes) are used as tabulated stress-strain curves. The off-axis tests are required to calculate the interaction terms $\left(F_{12}, F_{13}, F_{23}\right)$ defined in equations 2.7/2.10, 2.8/2.11, 2.9/2.12. This approach eliminates the use of curve fitting approximations, since tabulated stress-strain curves are used to track the evolution of the deformation response.

The tabulated stress-strain data can be generated from actual laboratory testing or supplemented using appropriate numerical experiments simulated in stand-alone codes (virtual testing). Though there are twelve required stress-strain curves for the model, the actual number of tests may be smaller based on the composite architecture. A unidirectional composite has transverse isotropy and hence requires only four tension and compression tests (1 and 2/3 directions), only two shear tests (1-2/3, 2-3), and only two 45° off-axis tests (1-2/3, 2-3). However, the 45° off-axis test in the 2-3 plane is not necessary, as the response is approximately equal to that of the uniaxial tension test in the 2/3 direction (as deduced from transverse isotropy). Thus, the number of required tests for a uniaxial composite can be reduced from twelve to seven, and a similar simplification approach can be used for other composites with some degree of symmetric architecture.

A summary of reducing experimental tests for a few special cases is shown in Table 2-1.

Table 2-1. Reduction of Experimental Testing Based on Composite Architecture

Label	**Experimental Test**	**Material Type**			
		Isotropic	**Plane Stress (2-D, thin shell)**	**Transversely Isotropic in 2-3 (Unidirectional Fiber Composite)**	**Transversely Isotropic in 1-2 (Plain Weave Composite)**
T1	Tension (1-direction)	Needed	Needed	Needed	Needed

Label	Experimental Test	Material Type			
		Isotropic	**Plane Stress (2-D, thin shell)**	**Transversely Isotropic in 2-3 (Unidirectional Fiber Composite)**	**Transversely Isotropic in 1-2 (Plain Weave Composite)**
T2	Tension (2-direction)	Same as T1	Needed	Needed	Same as T1
T3	Tension (3-direction)	Same as T1	Not Needed	Same as T2	Needed
C1	Compression (1-direction)	Needed	Needed	Needed	Needed
C2	Compression (2-direction)	Same as C1	Needed	Needed	Same as C1
C3	Compression (3-direction)	Same as C2	Not Needed	Same as C2	Needed
S12	Shear (1-2 direction)	Not Needed	Needed	Needed	Needed
S23	Shear (2-3 direction)	Not Needed	Not Needed	Needed	Needed
S13	Shear (1-3 direction)	Not Needed	Not Needed	Same as S12	Same as S23
O12	Off-axis Tension (45°, 1-2 plane)	Not Needed	Needed	Needed	Needed
O23	Off-axis Tension/Compression (45°, 2-3 plane)	Not Needed	Not Needed	Same as T2	Needed
O13	Off-axis Tension/Compression (45°, 1-3 plane)	Not Needed	Not Needed	Same as O12	Same as O23
	Total Number of Tests to Perform	2	6	7	8

The effective plastic strain is used as the tracking parameter for the evolution of the deformation response by determining the yield stresses from each of the tabulated input curves as a function of the effective plastic strain at each time step. Therefore, the tabulated stress-strain curves must be normalized and converted to stress versus effective plastic strain. This is achieved by using the principle of the equivalence of plastic work to relate the plastic strain increment to the effective plastic strain increment.

The effective plastic strain can then be written in terms of the plastic strain and flow potential function as (for a unidirectional loading in the 1-direction):

$$\begin{aligned}
\sigma_{ij} d\varepsilon_{ij}^{p} &= \sigma_e d\varepsilon_e^{p} = h d\varepsilon_e^{p} \\
\sigma_{11} d\varepsilon_{11}^{p} &= h d\varepsilon_e^{p} \\
\sigma_{11} d\varepsilon_{11}^{p} &= \sqrt{H_{11}}\sigma_{11} d\varepsilon_e^{p} \\
d\varepsilon_e^{p} &= \frac{\sigma_{11} d\varepsilon_{11}^{p}}{\sqrt{H_{11}}\sigma_{11}} \\
\varepsilon_e^{p} &= \int \frac{\sigma_{11} d\varepsilon_{11}^{p}}{\sqrt{H_{11}}\sigma_{11}}
\end{aligned} \qquad 2.29$$

where σ_{11} is the unidirectional stress, $d\varepsilon_{11}^{p}$ is the plastic strain increment in the loading direction, and $d\varepsilon_e^{p}$ is the effective plastic strain increment. The expression for the effective plastic strain in equation 2.29 can be rewritten as $\varepsilon_e^{p} = \int \frac{\sigma_{11} d\varepsilon_{11}^{p}}{h}$, in which it is clear that the effective plastic strain can be computed as the incremental area of the stress versus plastic strain curve divided by the current effective stress value. An example of this transformation is shown in Figure 2-3:

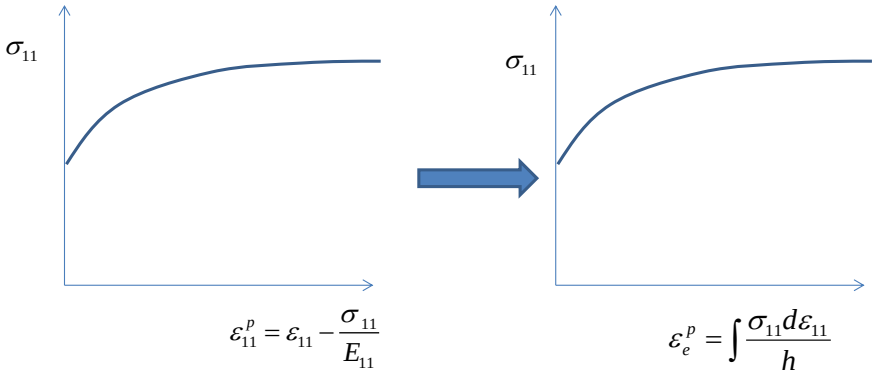

Figure 2-3. Conversion of stress versus plastic strain curves to stress versus effective plastic strain curves

The computation of the effective plastic strain is achieved using a numerical algorithm based on the radial return method. From the updated value of the effective plastic strain, the yield stress values and the overall stress state can be determined (details of

the numerical implementation are explained later in this dissertation). The revised stresses are computed using a typical elastic constitutive equation in which the flow law is used to describe the plastic strains as:

$$\dot{\boldsymbol{\sigma}} = \mathbf{C} : \left(\dot{\boldsymbol{\varepsilon}} - \dot{\boldsymbol{\varepsilon}}^{\mathrm{p}} \right) = \mathbf{C} : \left(\dot{\boldsymbol{\varepsilon}} - \dot{\lambda} \frac{\partial h}{\partial \boldsymbol{\sigma}} \right) \tag{2.30}$$

where $\mathbf{C}$ is the standard elastic stiffness matrix and $\boldsymbol{\sigma}$ is the total strain. The effective plastic strain rate, $\dot{\lambda}$, is calculated using a combination of the consistency condition (the stress state must remain on the subsequent yield surface, during the plastic deformation) and elastic constitutive equation as:

$$\begin{aligned} \dot{f} &= \frac{\partial f}{\partial \boldsymbol{\sigma}} \dot{\boldsymbol{\sigma}} + \frac{\partial f}{\partial \mathbf{q}} \dot{\mathbf{q}} = 0 \\ \dot{f} &= \frac{\partial f}{\partial \boldsymbol{\sigma}} \left(\mathbf{C} : \dot{\boldsymbol{\varepsilon}} - \mathbf{C} : \dot{\lambda} \frac{\partial h}{\partial \boldsymbol{\sigma}} \right) + \frac{\partial f}{\partial \mathbf{q}} \dot{\lambda} \frac{d\mathbf{q}}{d\lambda} = 0 \\ \dot{\lambda} &= \frac{\dfrac{\partial f}{\partial \boldsymbol{\sigma}} \mathbf{C} : \dot{\boldsymbol{\varepsilon}}}{\dfrac{\partial f}{\partial \boldsymbol{\sigma}} \mathbf{C} : \dfrac{\partial h}{\partial \boldsymbol{\sigma}} - \dfrac{\partial f}{\partial \mathbf{q}} \dfrac{d\mathbf{q}}{d\lambda}} \end{aligned} \tag{2.31}$$

where f is the yield function defined in equation 2.1 and $\mathbf{q}$ is the vector of yield stresses, determined from the input stress-strain data written as:

$$\mathbf{q}^T = \left[\sigma_{11}^T \quad \sigma_{22}^T \quad \sigma_{33}^T \quad \sigma_{11}^C \quad \sigma_{22}^C \quad \sigma_{33}^C \quad \sigma_{12} \quad \sigma_{23} \quad \sigma_{31} \quad \sigma_{45-12}^C \quad \sigma_{45-23}^C \quad \sigma_{45-31}^C \right] \tag{2.32}$$

The derivative of the $\mathbf{q}$ vector with respect to the effective plastic strain, λ, can be determined using a chain rule expansion based on the plastic strain as:

$$\frac{d\mathbf{q}}{d\lambda} = \frac{d\mathbf{q}}{d\boldsymbol{\varepsilon}^p} \frac{d\boldsymbol{\varepsilon}^p}{d\lambda} \tag{2.33}$$

where the derivative of the yield stress vector with respect to the plastic strain is the instantaneous slope of the stress versus plastic strain curve, and the derivative of the plastic strain with respect to the effective plastic strain is determined from the flow law, both corresponding to each of the twelve input stress-strain curves. However, special consideration must be taken in the off-axis case, for which the flow law must first be converted to the material axis coordinate system and then the plastic strains must be converted to the structural axis system. To do so, the off-axis test is first converted to stress vs. plastic strain in the structural axis system, then converted to stress vs. effective plastic strain. However, the flow law *h* is defined in terms of the material axis system of the off-axis test (1-2 case, for example) as:

$$(h)_{45-12} = \sqrt{H_{11}\sigma_{11}^2 + H_{22}\sigma_{22}^2 + 2H_{12}\sigma_{11}\sigma_{22} + H_{44}\sigma_{12}^2}$$

but the material axis stresses can be written in terms of the structural axis stress:

$$\sigma_{11} = 0.5\sigma$$
$$\sigma_{22} = 0.5\sigma$$
$$\sigma_{12} = -0.5\sigma$$

resulting in a simplified function of the off-axis case for the flow law as defined in equation 2.34:

$$(h)_{45-12} = 0.5\sigma_{45-12}\sqrt{H_{11} + H_{22} + 2H_{12} + H_{44}} \qquad 2.34$$

This is done in order to compute the correct derivative of the plastic strain with respect to the effective plastic strain, as the input for the off-axis tests is assumed to be in the structural coordinate system. Furthermore, the secant method is used with the radial return method to compute the necessary value of the effective plastic strain increment.

2.1.1 Characterization of Flow Law Coefficients

The flow law coefficients, introduced in the previous section, need to be characterized based on the data obtained from experimental stress-strain curves or virtual testing, with the procedures detailed in this section defined for quasi-static, room temperature tests. For example, if the mechanical properties of composite constituents are known, stress-strain curves can be generated through virtual tests conducted using either high fidelity finite element analysis, e.g., Virtual Testing System Software (VTSS) [28] developed at ASU, or analytical tools such as the micromechanics code MAC-GMC [29] developed at NASA Glenn.

The procedure for the determination of the flow law coefficients for a general composite is presented here, beginning with a unidirectional composite. In the case of a unidirectional carbon fiber composite, it is reasonable to assume that the plastic strain in the fiber direction (1-direction) is equal to zero for all values of stress, due to the linear elastic behavior of the carbon fiber [15]. From the second expression in equation 2.22, it is clear that the plastic strain can only be zero if the flow law coefficients H_{11}, H_{12}, and H_{13} are all equal to zero. In the same regard, the response in the transverse (2-direction) composite direction can show some degree of nonlinearity, and for a unidirectional load in the 2-direction, it is reasonable to assume the value of the effective stress, h, to be equal to the applied stress, σ_{22}. Then, the plastic potential function, equation 2.13, can be simplified for the case of a uniaxial applied load in the 2-direction as:

$$h = \sqrt{H_{22}\sigma_{22}^2} = \sqrt{H_{22}}\sigma_{22} \tag{2.35}$$

and from the assumption that the effective stress, h, is equal to the applied stress, σ_{22}, the flow law coefficient, H_{22}, must be equal to one. Due to the transverse isotropy in the unidirectional composite, the flow law coefficient, H_{33}, can be assumed to be one as well, and using these known values of the flow law coefficients, the remaining value, H_{23}, can be determined using equation 2.24 as

$$H_{23} = -H_{22}\nu_{23}^p = -\nu_{23}^p \tag{2.36}$$

The flow law coefficients are assumed to be constant, which requires a constant value of the plastic Poisson's ratio, and can be determined as an average value from unidirectional transverse tension test data. The flow law coefficient for in-plane shear, H_{44}, can be calculated using a similar procedure [15], in which the plastic potential function in equation 2.13, and plastic strain definition, in equation 2.22, are simplified for a pure shear loading case in the 1-2 plane as:

$$\begin{aligned} h &= \sigma_e = \sigma_{12}\sqrt{H_{44}} \\ d\varepsilon_{12}^p &= \frac{d\lambda}{2h}H_{44}\sigma_{12} = \frac{d\varepsilon_e^p}{2\sigma_{12}\sqrt{H_{44}}}H_{44}\sigma_{12} \\ &= 0.5d\varepsilon_e^p\sqrt{H_{44}} \\ or,\ d\varepsilon_e^p &= \frac{d\varepsilon_{12}^p}{0.5\sqrt{H_{44}}} \end{aligned} \tag{2.37}$$

Therefore, the shear coefficient, H_{44}, can be determined by fitting the effective stress versus effective plastic strain curve, for the in-plane shear, to the overall effective stress versus effective plastic strain curve, based on the transverse tension test for a unidirectional carbon fiber composite using equation 2.37. The coefficient, H_{55}, can be determined using a similar fitting approach using shear loading in the 2-3 plane, or, using transverse isotropy of the composite, the effective stress for an off-axis test in the 2-3 plane can be calculated and used to determine the coefficient, H_{55}, from H_{23}, as:

$$H_{55} = 2\left(1+\nu_{23}^p\right) = 2\left(1-H_{23}\right) \tag{2.38}$$

Finally, the last flow law coefficient, H_{66}, can be set equal to H_{44}, using transverse isotropy.

In the general case, such as a triaxially braided composite, similar procedures can be used to determine the flow law coefficients taking the tension test in the 1-direction as the baseline case. The flow law coefficient, H_{11}, can be determined by simplifying equation 2.13 for unidirectional applied stress in the 1-direction as:

$$h = \sqrt{H_{11}\sigma_{11}^2} = \sqrt{H_{11}}\sigma_{11} \tag{2.39}$$

From equation 2.39, it is clear that the coefficient, H_{11}, is equal to one. Thus, the relationships of the other flow law coefficients, from equations 2.23, 2.24, and 2.25, can be rewritten in terms of the known coefficient, H_{11}. First, modifying equations 2.23, 2.24, and 2.25 by assuming a value for H_{11} and eliminating H_{11} yields:

$$\begin{bmatrix} 0 & 0 & 0 & 1 & 0 \\ \nu_{21}^p & 0 & 1 & 0 & 0 \\ \nu_{23}^p & 0 & 0 & 0 & 1 \\ 0 & \nu_{32}^p & 0 & 0 & 1 \\ 0 & \nu_{31}^p & 0 & 1 & 0 \end{bmatrix} \begin{Bmatrix} H_{22} \\ H_{33} \\ H_{12} \\ H_{13} \\ H_{23} \end{Bmatrix} = \begin{Bmatrix} -\nu_{13}^p H_{11} \\ 0 \\ 0 \\ 0 \\ 0 \end{Bmatrix}. \tag{2.40}$$

These equations are linearly independent, and one can solve for the five unknown coefficients. Pivoting the rows results in:

$$\begin{bmatrix} \nu_{23}^p & 0 & 0 & 0 & 1 \\ 0 & \nu_{31}^p & 0 & 1 & 0 \\ \nu_{21}^p & 0 & 1 & 0 & 0 \\ 0 & 0 & 0 & 1 & 0 \\ 0 & \nu_{32}^p & 0 & 0 & 1 \end{bmatrix} \begin{Bmatrix} H_{22} \\ H_{33} \\ H_{12} \\ H_{13} \\ H_{23} \end{Bmatrix} = \begin{Bmatrix} 0 \\ 0 \\ 0 \\ -\nu_{13}^p H_{11} \\ 0 \end{Bmatrix}. \tag{2.41}$$

Now that the diagonals are all non-zero, a Gauss-Jordan elimination can be performed to obtain an analytical expression for the five remaining flow rule coefficients, which yields:

$$\begin{bmatrix} 1 & 0 & 0 & 0 & 0 \\ 0 & 1 & 0 & 0 & 0 \\ 0 & 0 & 1 & 0 & 0 \\ 0 & 0 & 0 & 1 & 0 \\ 0 & 0 & 0 & 0 & 1 \end{bmatrix} \begin{Bmatrix} H_{22} \\ H_{33} \\ H_{12} \\ H_{13} \\ H_{23} \end{Bmatrix} = \begin{Bmatrix} \frac{\nu_{32}^p \nu_{13}^p}{\nu_{23}^p \nu_{31}^p} H_{11} \\ \frac{\nu_{13}^p}{\nu_{31}^p} H_{11} \\ -\frac{\nu_{21}^p \nu_{32}^p \nu_{13}^p}{\nu_{23}^p \nu_{31}^p} H_{11} \\ -\nu_{13}^p H_{11} \\ \frac{\nu_{32}^p \nu_{13}^p}{\nu_{31}^p} H_{11} \end{Bmatrix}. \quad 2.42$$

Therefore, the coefficients can be rewritten in terms of the plastic Poisson's ratios and H_{11} (equal to one) as:

$$\begin{aligned} H_{12} &= -\nu_{12}^p H_{11} = -\nu_{12}^p \\ H_{13} &= -\nu_{13}^p H_{11} = -\nu_{13}^p \\ H_{22} &= \frac{\nu_{12}^p}{\nu_{21}^p} H_{11} = \frac{\nu_{12}^p}{\nu_{21}^p} \\ H_{23} &= \frac{-\nu_{23}^p \nu_{12}^p}{\nu_{21}^p} H_{11} = \frac{-\nu_{23}^p \nu_{12}^p}{\nu_{21}^p} \\ H_{33} &= \frac{\nu_{13}^p}{\nu_{31}^p} H_{11} = \frac{\nu_{13}^p}{\nu_{31}^p} \end{aligned} \quad 2.43$$

where the shown coefficients are based solely on the plastic Poisson's ratios. The final three flow law coefficients H_{44}, H_{55}, and H_{66}, are determined using the same fit technique as in the simplified case, but each shear curve must be fit with the 1-direction test acting as the baseline. These are calculated by fitting the effective stress versus effective plastic strain curves of the shear tests with the baseline uniaxial test. In order to fit the shear curves with the uniaxial curve and find the optimal flow rule coefficient value, H_{ll}^*, the difference between the two curves is minimized as:

$$f(\mathrm{H}_{ll}) = \sum_{k=1}^{n} \left[\left(\hat{\sigma}_{ii} \right)_k - \left(\hat{\sigma}_{ij} \right)_k \right]^2 \quad 2.44$$

such that:

$$H_{ll}^{\min} \le H_{ll}^{*} \le H_{ll}^{\max} \qquad 2.45$$

where *n* is the number of data points in the master curve, $\left(\hat{\sigma}_{ii}\right)_k$ is the k[th] effective stress value from the baseline curve, and $\left(\hat{\sigma}_{ij}\right)_k$ is the effective stress value for the shear curve.

2.1.2 Convexity of the Yield Surface

The current yield stresses are determined using a curve search of a set of input stress-strain curves. Each of the 12 input curves is stored as stress versus total effective plastic strain, thus allowing the model to describe different hardening properties in each direction. By tracking the effective plastic strain in the deformation model, the evolution of the yield stresses in the various coordinate directions can then be correlated to the current value of the effective plastic strain.

The Tsai-Wu based yield function, used as the yield surface to track plasticity, is quite general and can result in both convex and concave yield surfaces. The yield surface used in the elasto-plastic deformation model must be convex, as the radial return procedure employed for the numerical implementation of the model utilizes the value of the yield function to determine if the stress state has returned to the yield surface. It should be noted that plasticity theory in general requires a convex yield surface [30]. If the original input parameters do not produce an appropriate convex yield surface, a convex correction procedure must be implemented. An example of a non-convex yield surface that is modified to render it convex is shown in Figure 2-4. The off-axis stress values were corrected, as explained later, to make the surface convex.

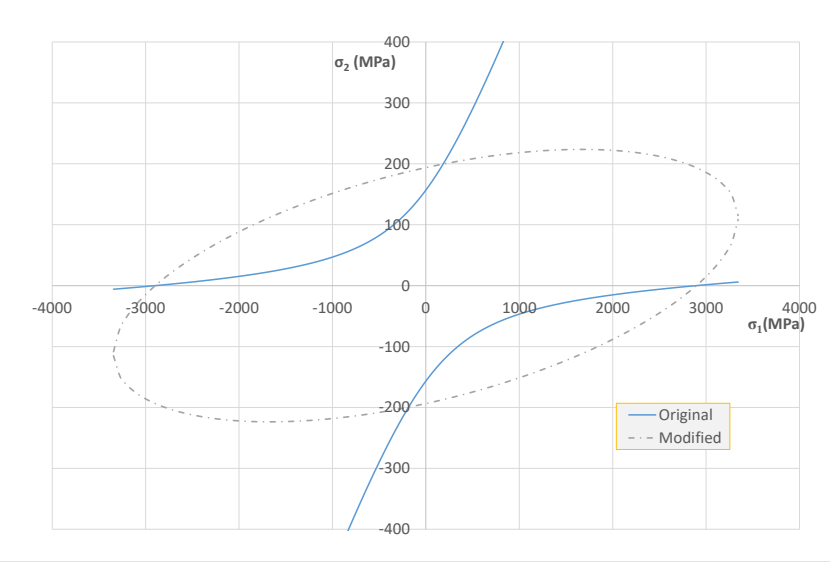

(a)

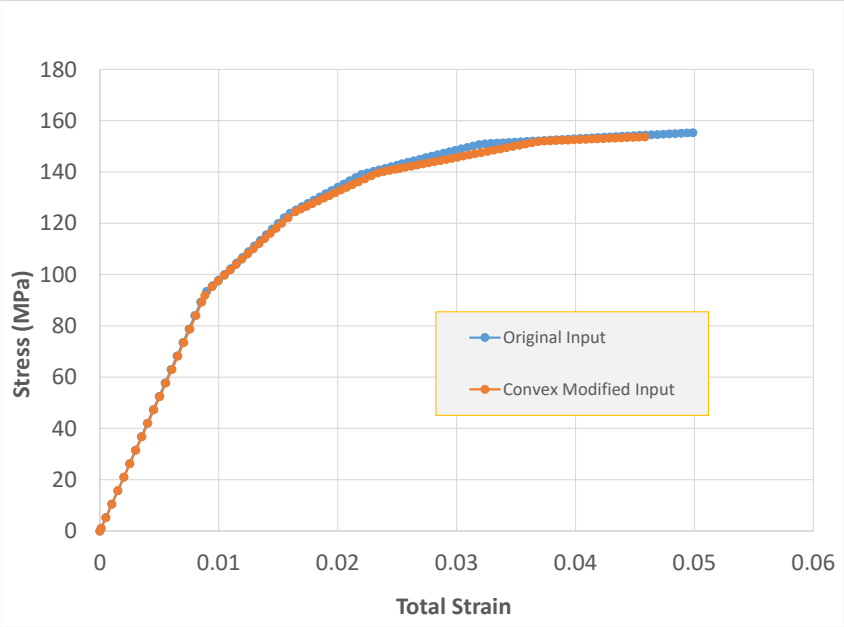

(b)

Figure 2-4. (a) Non-convex and modified convex yield surfaces, (b) modification of original stress-strain curve to yield a fully convex stress-strain curve

For the yield surface to remain convex, the following conditions must be met (adapted from equation 2.21, derived for convexity of the plastic potential function):

$$F_{11} \geq 0, F_{22} \geq 0, F_{33} \geq 0, F_{44} \geq 0, F_{55} \geq 0, F_{66} \geq 0$$
$$F_{11}F_{22} - F_{12}^2 \geq 0, F_{33}F_{22} - F_{23}^2 \geq 0, F_{11}F_{33} - F_{31}^2 \geq 0 \quad (2.46)$$

Note that the diagonal terms are always positive and the final three conditions must be satisfied. One way of ensuring convexity is by modifying the off-axis terms (F_{12}, F_{23}, F_{31}) while retaining the original values of the diagonal terms (F_{11}, F_{22}, F_{33}). The convexity-satisfying conditions of the shear terms can be represented as:

$$F_{ij} \leq \sqrt{F_{ii}F_{jj}} \quad (2.47)$$

However, by making the condition more restrictive, the modified off-axis values can be found such that the convexity condition is satisfied more readily, and in a form that is more commonly used in the original Tsai-Wu failure criterion, as:

$$F'_{ij} = -\frac{1}{2}\sqrt{F_{ii}F_{jj}} \quad (2.48)$$

Allowing for the off-axis yield stress values to be modified for convexity, the right-hand sides of equations 2.5, 2.7/2.10, 2.8/2.11, and 2.9/2.12 can be set equal to the value

obtained from equation 2.48, thus allowing for the determination of a modified yield stress in a particular direction. For example, for the case of the off-axis tension test in the 1-2 plane, the modified value of the yield stress required to ensure the yield stress is convex can be determined as follows:

$$F'_{12} = \frac{2}{\left(\sigma'^{45}_{12}\right)^2} - \frac{F_1 + F_2}{\sigma'^{45}_{12}} - \frac{1}{2}\left(F_{11} + F_{22} + F_{44}\right)$$

$$\frac{2}{\left(\sigma'^{45}_{12}\right)^2} - \frac{F_1 + F_2}{\sigma'^{45}_{12}} - \frac{1}{2}\left(F_{11} + F_{22} + F_{44}\right) - F'_{12} = 0$$

$$2 - \left(F_1 + F_2\right)\sigma'^{45}_{12} - \frac{1}{2}\left(F_{11} + F_{22} + F_{44}\right)\left(\sigma'^{45}_{12}\right)^2 - F'_{12}\left(\sigma'^{45}_{12}\right)^2 = 0$$

$$a\left(\sigma'^{45}_{12}\right)^2 + b\sigma'^{45}_{12} - 2 = 0 \qquad 2.49$$

where

$$a = F'_{12} + \frac{1}{2}\left(F_{11} + F_{22} + F_{44}\right)$$

$$b = F_1 + F_2$$

and σ'^{45}_{12} is the corrected off-axis yield stress value. If the tension and compression responses are the same (yield stress values the same for a given direction), the linear coefficients (F_1, F_2, F_3) are equal to zero and equation 2.49 can be simplified as:

$$\sigma'^{45}_{12} = \sqrt{\frac{2}{a}} \qquad 2.50$$

This convexity must be ensured through all time steps and iterations. In practice, at any point where the yield function is determined, convexity must first be checked and, if non-convex, the required off-axis yield coefficients and stresses for convexity are calculated based on equation 2.48.

2.1.3 Temperature and Strain Rate Dependencies

Strain rate and temperature dependent material response is incorporated into the elasto-plastic material model using tabulated experimental input data derived from the same 12 tests detailed earlier. These effects are important for impact simulation due to the high load rate and associated increased localized temperatures at the point of impact. If strain rate and/or temperature effects need to be modeled, multiple curves for each of the 12 experimental tests, performed at different strain rates, are used as input data for the model. All of the strain rate and temperature dependent curves are modified the same way, as described earlier, and converted to stress versus effective plastic strain, explained in chapter 3. The interpolation is necessary between the different strain rate curves, based on the strain rate at a given time step, when updating the yield

stresses during the plasticity algorithm, in equation 2.33. Additionally, the elastic moduli are interpolated based on the strain rate and temperature dependent input data.
For the case of the off-axis curves, the strain rate associated with the principal material directions (PMD) are not readily available. Thus, the strain rates associated with the off-axis tests must be calculated using a transformation of the material axis system strain rate values. The material model subroutine (MAT213) receives the deformation rate tensor in the global X-Y-Z coordinate system from the finite element analysis (LS-DYNA). Within the MAT213 subroutine, the tensor components are transformed to the PMDs (1-2-3 system) as:

$$\mathbf{d} = \begin{bmatrix} d_{11} & d_{22} & d_{33} & d_{12} & d_{23} & d_{13} \end{bmatrix} \tag{2.51}$$

The deformation rate tensor can be written in terms of the small incremental strain tensor if the magnitudes of the displacement gradients are small, $\left|\partial u_i / \partial x_j\right| << 1$. Thus, the deformation rate tensor can be written as:

$$\dot{\boldsymbol{\varepsilon}} = \begin{bmatrix} \dot{\varepsilon}_{11} & \dot{\varepsilon}_{22} & \dot{\varepsilon}_{33} & \dot{\varepsilon}_{12} & \dot{\varepsilon}_{23} & \dot{\varepsilon}_{13} \end{bmatrix} = \begin{bmatrix} d_{11} & d_{22} & d_{33} & 0.5d_{12} & 0.5d_{23} & 0.5d_{13} \end{bmatrix} \tag{2.52}$$

The transformation of the principal strain rates can be performed to obtain the associated 45° off-axis terms as:

$$\dot{\boldsymbol{\varepsilon}}'_{3\times3} = \mathbf{a}_{3\times3}\dot{\boldsymbol{\varepsilon}}_{3\times3}\mathbf{a}^{T}_{3\times3} \tag{2.53}$$

where the transformation tensor **a** can be defined for each off-axis case as:

$$\mathbf{a}^{45}_{1-2} = \begin{bmatrix} 0.707 & 0.707 & 0 \\ -0.707 & 0.707 & 0 \\ 0 & 0 & 1 \end{bmatrix} \tag{2.54}$$

$$\mathbf{a}^{45}_{2-3} = \begin{bmatrix} 1 & 0 & 0 \\ 0 & 0.707 & 0.707 \\ 0 & -0.707 & 0.707 \end{bmatrix} \tag{2.55}$$

$$\mathbf{a}^{45}_{1-3} = \begin{bmatrix} 0.707 & 0 & -0.707 \\ 0 & 1 & 0 \\ 0.707 & 0 & 0.707 \end{bmatrix} \tag{2.56}$$

The corresponding diagonal component of the resulting transformed strain rate tensors, $\dot{\boldsymbol{\varepsilon}}'$, are needed to define the corresponding resultant off-axis strain rates and are calculated using equations 2.54, 2.55, and 2.56 in equation 2.53. Therefore, the resultant strain rates for the off-axis tests, given strain rates in the principal axis can be written as:

$$\dot{\varepsilon}_{1\text{-}2}^{45} = \dot{\varepsilon}'_{11} = 0.5\dot{\varepsilon}_{11} + \dot{\varepsilon}_{12} + 0.5\dot{\varepsilon}_{22} \quad 2.57$$

$$\dot{\varepsilon}_{2\text{-}3}^{45} = \dot{\varepsilon}'_{22} = 0.5\dot{\varepsilon}_{22} + \dot{\varepsilon}_{23} + 0.5\dot{\varepsilon}_{33} \quad 2.58$$

$$\dot{\varepsilon}_{1\text{-}3}^{45} = \dot{\varepsilon}'_{33} = 0.5\dot{\varepsilon}_{11} + \dot{\varepsilon}_{13} + 0.5\dot{\varepsilon}_{33} \quad 2.59$$

The input curves for the principal directions account for compression and tension for use in defining the yield surface. Hence care must be taken when using the strain rates corresponding to the three principal directions (equation 2.52), since they can be either positive (tension) or negative (compression). Thus, if the PMD strain rate is positive, then the tension strain rate value is taken as that, whereas the compression strain rate value would be zero (quasi-static) and vice-versa. This procedure is outlined below.

$$\begin{aligned}
&\textit{if } \dot{\varepsilon}_{ii} > 0 \textit{ then } \dot{\varepsilon}_{ii}^{t} = \dot{\varepsilon}_{ii} \textit{ and } \dot{\varepsilon}_{ii}^{c} = 0 \\
&\textit{elseif } \dot{\varepsilon}_{ii} < 0 \textit{ then } \dot{\varepsilon}_{11}^{c} = \dot{\varepsilon}_{11} \textit{ and } \dot{\varepsilon}_{ii}^{t} = 0 \\
&\textit{else } \dot{\varepsilon}_{ii}^{t} = 0 \textit{ and } \dot{\varepsilon}_{ii}^{c} = 0
\end{aligned}$$

2.2 IMPLEMENTATION DETAILS

In this section, details of the numerical implementation of the theory discussed in chapter 2 are shown and discussed. The focus is on the deformation model including rate and temperature effects.

The following sets of data are needed as input to the model:

1. Twelve true stress versus true strain curves at a prescribed strain rate and a prescribed temperature from:

    a. uniaxial tension tests in 1-, 2-, and 3-directions,
    b. uniaxial compression tests in 1-, 2-, and 3-directions,
    c. shear in 1-2, 2-3 and 1-3 planes, and
    d. 45 degrees off-axis uniaxial tension or compression in 1-2, 2-3, and 1-3 planes,

    are required in a tabulated x-y data form. The number of such data sets is a function of the material's behavior as a function of strain rate and temperature dependence.

2. Also required are the modulus of elasticity, Poisson's ratio, and average plastic Poisson's ratio (averaged over the entire nonlinear portion of the stress-strain curve) obtained from the tension and compression tests. The basic elastic properties are required for the elastic portion of the deformation analysis, and the plastic Poisson's ratios are needed to compute the coefficients in the plastic potential function.

The first six flow rule coefficients are computed directly from the assumed flow rule coefficient value and the plastic Poisson's ratios. (See equation 2.43.) The last three flow rule coefficients $\left(H_{44}, H_{55}, H_{66}\right)$ are calculated by using the fitting technique described in equation 2.44.

Each set of the twelve input curves are normalized with respect to the effective plastic strain, where the effective plastic strain can be expressed in terms of the experimental stress versus total strain data. For the compressive response in the 1-direction, for example, this is written as:

$$\left.\begin{array}{l} \sigma_{11}^{c}\left(\varepsilon_{11}^{p}=\varepsilon_{11}-\dfrac{\sigma_{11}^{c}}{E_{11}}\right) \\ \varepsilon_{e}^{p}=\int\left(\sigma_{11} d\varepsilon_{11}^{p} / h\right) \end{array}\right\} \Rightarrow \sigma_{11}^{c}\left(\varepsilon_{e}^{p}\right) \qquad 2.60$$

where σ_{11}^{c} is the experimental compressive true stress in the 1-direction, ε_{11} is the total true strain in the 1-direction, E_{11} is the elastic modulus in the 1-direction, ε_{11}^{p} is the true plastic strain in the 1-direction, ε_{e}^{p} is the effective plastic strain, and h is the value of the effective stress as shown in equation 2.13.

Once the input curves are fully normalized, the plasticity algorithm is initiated. In the following, the subscript "*n*" refers to the value from the previous time step, the subscript "*n+1*" refers to the value from the current time step, the superscript "*i*" refers to the value from the previous iteration within a time step, the superscript "*i+1*" refers to the value from the current iteration, and the superscript "*i-1*" refers to the value from the 2nd iteration prior to the current iteration. To numerically implement the material model, a typical elastic stress update is applied as follows:

$$\boldsymbol{\sigma}_{n+1}=\boldsymbol{\sigma}_{n}+\mathbf{C}\Delta t:\left(\dot{\boldsymbol{\varepsilon}}-\dot{\boldsymbol{\varepsilon}}^{p}\right) \qquad 2.61$$

where $\mathbf{C}$ is the orthotropic elastic stiffness matrix, Δt is the time step, $\dot{\boldsymbol{\varepsilon}}$ is the total strain rate, and $\dot{\boldsymbol{\varepsilon}}^{p}$ is the plastic strain rate as defined in equation 2.22. The elastic stiffness matrix is written in terms of the compliance matrix as:

$$\mathbf{C} = \mathbf{S}^{-1} = \begin{bmatrix} \frac{1}{E_{11}} & -\frac{\nu_{21}}{E_{22}} & -\frac{\nu_{31}}{E_{33}} & 0 & 0 & 0 \\ & \frac{1}{E_{22}} & -\frac{\nu_{32}}{E_{33}} & 0 & 0 & 0 \\ & & \frac{1}{E_{33}} & 0 & 0 & 0 \\ & & & \frac{1}{G_{23}} & 0 & 0 \\ & Sym & & & \frac{1}{G_{31}} & 0 \\ & & & & & \frac{1}{G_{12}} \end{bmatrix}^{-1} \quad 2.62$$

where E_{ii} are the elastic moduli in the principal material directions, G_{ij} are the elastic shear moduli, and ν_{ij} are the elastic Poisson's ratios. The elastic moduli values shown above are interpolated based on the temperature and strain rate data. The current values of the yield stresses used to determine the yield function coefficients are summarized into a single vector, equation 2.32, corresponding to data obtained from each of the 12 input experimental test curves with the rate of change represented as:

$$\dot{\mathbf{q}} = \dot{\lambda} \frac{d\mathbf{q}}{d\lambda} \quad 2.63$$

The vector of yield stress values is updated during the strain hardening process, adjusted yield stresses are checked for convexity, and, if necessary, the off-axis terms are based on convexity conditions using equations 2.48 and 2.50. The yield stresses in the various coordinate directions are assumed to evolve as a function of the effective plastic strain. Lastly, as defined in equation 2.31 and expanded here, the plasticity consistency condition is written in terms of the gradient of the yield function as:

$$\dot{f} = \frac{\partial f}{\partial \boldsymbol{\sigma}} \dot{\boldsymbol{\sigma}} + \frac{\partial f}{\partial \mathbf{q}} \dot{\mathbf{q}} = 0 \quad 2.64$$

which establishes the requirement for the stress state to remain on the yield surface, hence the inclusion of the yield stress vector. Equations 2.22 and 2.61 can be applied within equation 2.64 to obtain the following expression:

$$\dot{f} = \frac{\partial f}{\partial \boldsymbol{\sigma}} \left(\mathbf{C} : \dot{\boldsymbol{\varepsilon}} - \mathbf{C} : \dot{\lambda} \frac{\partial h}{\partial \boldsymbol{\sigma}} \right) + \frac{\partial f}{\partial \mathbf{q}} \dot{\lambda} \frac{d\mathbf{q}}{d\lambda} = 0 \quad 2.64a$$

where $\dot{\boldsymbol{\sigma}}$ is written in terms of the stiffness matrix and total and plastic strain rates, and the rate of change in the yield stresses has been expanded using equation 2.63. As discussed earlier, due to the strain hardening formulation applied in the plasticity law, the plastic multiplier $\dot{\lambda}$ can be shown to be equal to the effective plastic strain. Solving for the effective plastic strain rate produces the following consistency equation, which is utilized within the numerical algorithm to compute an estimate used for the evolution of the effective plastic strain:

$$\dot{\lambda} = \frac{\dfrac{\partial f}{\partial \boldsymbol{\sigma}} \mathbf{C} : \dot{\boldsymbol{\varepsilon}}}{\dfrac{\partial f}{\partial \boldsymbol{\sigma}} \mathbf{C} : \dfrac{\partial h}{\partial \boldsymbol{\sigma}} - \dfrac{\partial f}{\partial \mathbf{q}} \dfrac{d\mathbf{q}}{d\lambda}} \qquad 2.65$$

To start the calculations for a particular time step, the current values of the yield stresses, set equal to the original yield stresses until initial yield occurs, and set equal to the yield stresses corresponding to the current value of the effective plastic strain after initial yield occurs, are set in the vector $\mathbf{q}$ shown in equation 2.63. These current yield stresses are also used in equations 2.5, 2.7/2.10, 2.8/2.11, and 2.9/2.12 to compute the initial estimate of the coefficients of the yield function for the time step. To compute the increment in effective plastic strain (and the resulting stress state) for a particular time step, a variation of the radial return algorithm, commonly used in plasticity analysis [27], is employed. To initiate the algorithm, a perfectly elastic response is assumed. Therefore, an elastic predictor is used to compute an initial estimate for the stresses at the end of the time step as follows:

$$\left(\boldsymbol{\sigma}\right)^{e} = \left(\boldsymbol{\sigma}\right)^{n} + \mathbf{C}\Delta t : \left(\dot{\boldsymbol{\varepsilon}}\right) \qquad 2.66$$

With the elastic trial stresses computed, a trial yield function value can be calculated from equation 2.1 using the current values of the yield stresses to determine if the load step is elastic or plastic by applying the following expression:

$$f\left(\boldsymbol{\sigma}^{e}, \mathbf{q}^{n}\right) \le 0 \;?, \;\; if \;\; yes \Rightarrow elastic \begin{cases} \boldsymbol{\sigma}^{n+1} = \boldsymbol{\sigma}^{e} \\ \Delta\lambda = 0 \end{cases} \qquad 2.67$$

If the value of the yield function is less than zero, the time step is assumed to be an elastic time step, the values of the stresses at the end of the time step are set equal to the elastic trial stresses, and the algorithm continues to the next time step.

If the value of the yield function is greater than zero, the time step is assumed to be a plastic time step, and the radial return algorithm must be employed to bring the stress state back to the yield surface by computing a converged value for the increment in effective plastic strain, $\Delta\lambda$.

If the trial yield function is greater than zero, then $\Delta\lambda > 0$ must be true. The value of $\Delta\lambda_i$ (*i* is the iteration number) is determined using a secant iteration, with $\Delta\lambda_i^1 = 0$ for the first iteration (assuming a purely elastic response). An estimate for a second iterative value for the effective plastic strain is determined from the consistency equation (equation 2.65), as:

$$\Delta\lambda_i^2 = \frac{\left.\frac{\partial f}{\partial \boldsymbol{\sigma}}\right|_e : \left(\boldsymbol{\sigma}^e - \boldsymbol{\sigma}^n\right)}{\left.\frac{\partial f}{\partial \boldsymbol{\sigma}}\right|_e \mathbf{C} : \left.\frac{\partial h}{\partial \boldsymbol{\sigma}}\right|_e - \frac{\partial f}{\partial \mathbf{q}}\frac{d\mathbf{q}}{d\lambda}} \approx \frac{\left.\frac{\partial f}{\partial \boldsymbol{\sigma}}\right|_e : \left(\boldsymbol{\sigma}^e - \boldsymbol{\sigma}^n\right)}{\left.\frac{\partial f}{\partial \boldsymbol{\sigma}}\right|_e \mathbf{C} : \left.\frac{\partial h}{\partial \boldsymbol{\sigma}}\right|_e} \qquad 2.68$$

where the derivatives of $\mathbf{q}$ are taken as zero, meaning that the response is assumed to be perfectly plastic. If a negative estimate for the increment in effective plastic strain is computed, the effective plastic strain increment value is either set equal to the value of total effective plastic strain, if not zero (after initial yield is reached), or the absolute value of the strain increment (until initial yield is reached). The partial derivatives of the yield function and the plastic potential function with respect to the stresses can be evaluated from equations 2.1 and 2.13, respectively, as:

$$\frac{\partial f}{\partial \boldsymbol{\sigma}} = \begin{bmatrix} F_1 + 2F_{11}\sigma_{11} + 2F_{12}\sigma_{22} + 2F_{13}\sigma_{33} \\ F_2 + 2F_{12}\sigma_{11} + 2F_{22}\sigma_{22} + 2F_{23}\sigma_{33} \\ F_3 + 2F_{13}\sigma_{11} + 2F_{23}\sigma_{22} + 2F_{33}\sigma_{33} \\ F_{44}\sigma_{12} \\ F_{55}\sigma_{23} \\ F_{66}\sigma_{31} \end{bmatrix} \qquad 2.69$$

$$\frac{\partial h}{\partial \boldsymbol{\sigma}} = \frac{1}{2h}\begin{bmatrix} 2H_{11}\sigma_{11} + 2H_{12}\sigma_{22} + 2H_{13}\sigma_{33} \\ 2H_{12}\sigma_{11} + 2H_{22}\sigma_{22} + 2H_{23}\sigma_{33} \\ 2H_{13}\sigma_{11} + 2H_{23}\sigma_{22} + 2H_{33}\sigma_{33} \\ H_{44}\sigma_{12} \\ H_{55}\sigma_{23} \\ H_{66}\sigma_{31} \end{bmatrix} \qquad 2.70$$

By assuming a condition of perfect plasticity in the second iteration, the stress state is ensured to return to the interior of the yield surface, thus resulting in a negative value of the yield function. If a negative value of the yield function is not obtained, the estimate for the effective plastic strain increment is doubled and the process is repeated until a negative yield function value is reached. By utilizing this procedure for the first two

iterations the solution is bounded, which helps to ensure a reasonable convergence towards the actual increment in effective plastic strain for the time step. Once the increment in effective plastic strain, $\Delta\lambda$, is computed for the second iteration, the corresponding stresses (including a plastic correction from the elastic trial stresses), can be computed using a modified version of equation 2.61, where the stiffness matrix multiplied by the total strain is set equal to the elastic trial stress, and the plastic strain is written in terms of the effective plastic strain increment and the gradient of the plastic potential function evaluated using the elastic trial stresses.

$$\boldsymbol{\sigma}_{n+1} = \boldsymbol{\sigma}^e - \mathbf{C} : \Delta\lambda \left.\frac{\partial h}{\partial \boldsymbol{\sigma}}\right|_e \tag{2.71}$$

These modified stresses can then be used to compute a new estimate of the value of the yield function for the second iteration of the secant iteration process. Given the estimates of the effective plastic strain and value of the yield function for the first two iterations, a secant process can be used to compute a revised estimate to be used in a third iteration of the effective plastic strain:

$$\Delta\lambda^3 = \Delta\lambda^1 - f^1 \frac{\Delta\lambda^2 - \Delta\lambda^1}{f^2 - f^1} \tag{2.72}$$

In the above equation, the superscript represents the iteration number corresponding to the given term. A revised estimate of the stresses for the third iteration within the time step is calculated using a revised version of equation 2.71, where the gradient of the plastic potential function is computed using the stresses computed during the second iteration and the effective plastic strain value computed for the third iteration is employed:

$$\boldsymbol{\sigma}\big|_{n+1}^3 = \boldsymbol{\sigma}^e - \mathbf{C} : \Delta\lambda^3 \left.\frac{\partial h}{\partial \boldsymbol{\sigma}}\right|_{\Delta\lambda^2} \tag{2.73}$$

Based on these revised stresses, the value of the yield function for the third iteration is computed. At this point, convergence of the secant iteration can be checked by applying the following conditions:

$$\begin{aligned}
&f_3 \approx 0 \Rightarrow \Delta\lambda = \Delta\lambda^3; \\
&f_3 > 0 \Rightarrow \begin{cases} \Delta\lambda^1 = \Delta\lambda^3,\ f^1 = f\big|_{n+1}^3 \\ \Delta\lambda^2 = \Delta\lambda^2,\ f^1 = f\big|_{n+1}^1 \end{cases}; \\
&f_3 < 0 \Rightarrow \begin{cases} \Delta\lambda^1 = \Delta\lambda^1,\ f^1 = f\big|_{n+1}^1 \\ \Delta\lambda^2 = \Delta\lambda^3,\ f^2 = f\big|_{n+1}^3 \end{cases}
\end{aligned} \tag{2.74}$$

If the value of the yield function is not less than some predefined tolerance, the secant iteration process is continued. To continue the secant iterations, the increment of the effective plastic strain used in the next iteration (now generalized to iteration “i+1”), is computed using an expression similar to equation 2.72:

$$\Delta\lambda_{n+1}^{i+1} = \Delta\lambda^1 - f^1 \frac{\Delta\lambda^2 - \Delta\lambda^1}{f^2 - f^1} \qquad 2.75$$

where the values to be used in the expression are determined based on equation 2.74. The new estimate for the effective plastic strain is then used to determine a new set of updated stresses as follows:

$$\boldsymbol{\sigma}\Big|_{n+1}^{i+1} = \boldsymbol{\sigma}_n + \mathbf{C} : \left[\Delta\boldsymbol{\varepsilon} - \Delta\lambda_{n+1}^{i+1} \frac{\partial h}{\partial \boldsymbol{\sigma}}\Big|_{n+1}^{i} \right] \qquad 2.76$$

In this expression, the gradient of the plastic potential function is determined based on the stresses computed in the previous increment. The rationale for computing the gradient of the plastic potential function using stresses other than the trial elastic stresses is based on the fact that due to the anisotropic hardening of the material the yield surface rotates (besides just expanding) as additional plastic strain is applied. The anisotropic strain hardening results from the fact that the changes in yield stresses in the various coordinate directions are not necessarily proportional. This concept, which is displayed schematically in figure 2.5 is discussed in more detail in [30].

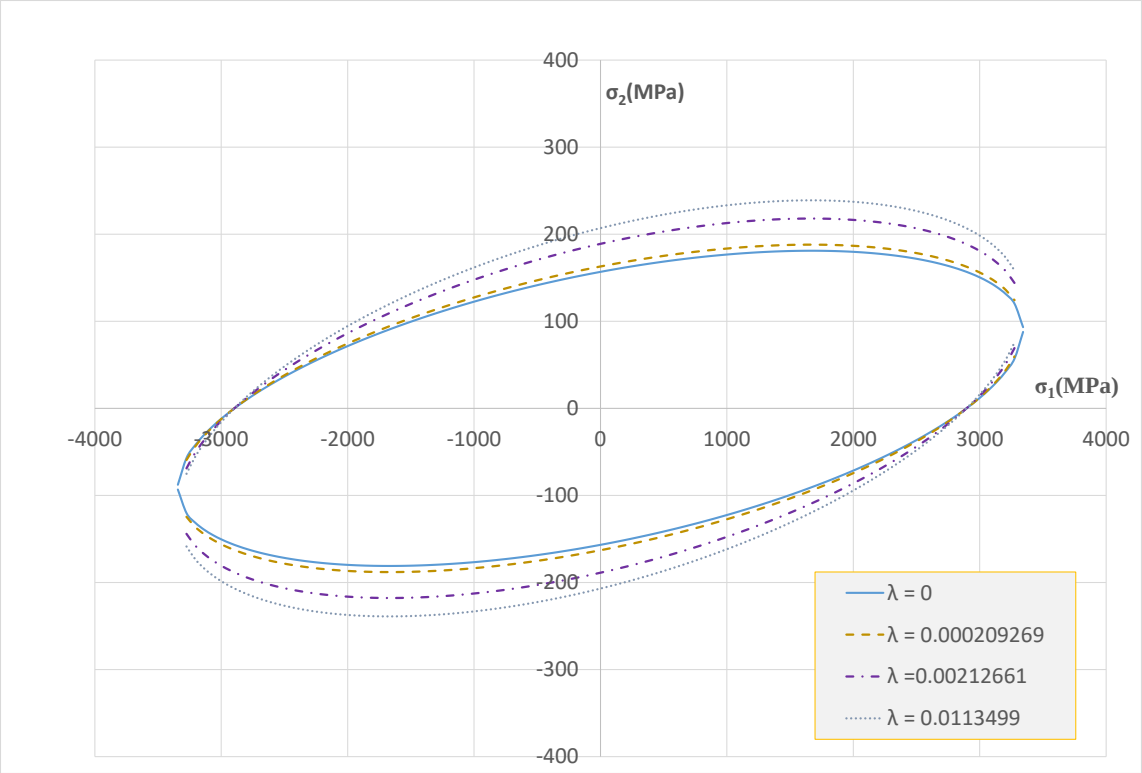

Figure 2-5. Anisotropic yield surface evolution in 1-2 stress space

After the revised stresses for the new iteration are computed, the yield function value is evaluated with these updated stresses, and updated yield stresses are computed based on the new estimate for the effective plastic strain and the input curves. Based on the revised computed value for the yield function, $f\big|_{n+1}^{i+1}$, convergence is checked and revised parameters required for the secant method computations of the increments of effective plastic strain are determined based on the following revised version of equation 2.74:

$$
\begin{aligned}
&f\big|_{n+1}^{i+1} \approx 0 \Rightarrow \Delta\lambda = \Delta\lambda^{i+1};\\
&f\big|_{n+1}^{i+1} > 0 \Rightarrow \begin{cases} \Delta\lambda^{1} = \Delta\lambda^{i+1},\ f^{1} = f\big|_{n+1}^{i+1} \\ \Delta\lambda^{2} = \Delta\lambda^{i},\ f^{2} = f\big|_{n+1}^{i} \end{cases};\\
&f\big|_{n+1}^{i+1} < 0 \Rightarrow \begin{cases} \Delta\lambda^{1} = \Delta\lambda^{i-1},\ f^{1} = f\big|_{n+1}^{i-1} \\ \Delta\lambda^{2} = \Delta\lambda^{i+1},\ f^{2} = f\big|_{n+1}^{i+1} \end{cases}
\end{aligned}
\qquad 2.77
$$

If convergence is not reached, the process described in equation 2.75 and equation 2.76 is repeated for a new iteration. Once convergence is satisfied, the appropriate increment of effective plastic strain is known based on the iteration results and the stresses can be updated as:

$$\boldsymbol{\sigma}_{n+1} = \boldsymbol{\sigma}^{e} - \mathbf{C} : \Delta\lambda \frac{\partial h}{\partial \boldsymbol{\sigma}} \tag{2.78}$$

where the stress values computed in the iteration prior to convergence being reached are used to compute the gradient of the plastic potential function. Finally, the yield stresses are updated as well, using the new value of the overall effective plastic strain, λ , in each input curve to determine the corresponding yield stress level, with respect to the temperature and strain rate, as:

$$q_{n+1} = q\left(\lambda_n + \Delta\lambda, \dot{\varepsilon}, T\right) \tag{2.79}$$

A detailed algorithm that has been implemented as a computer code is presented below.

The following parameters are referenced in the algorithm:

- δ_{tol} Tolerance value. Default is 10^{-6}.
- $n_{\sec\max}$ Maximum number of iterations allowed in the secant method. Default is 100.
- n_{double} Maximum times the value of $\Delta\lambda$ is incremented with a factor in order to find a negative value of yield function thus bounding the solution. Default is 1000. The factor used is 1.1.

Step 1: *Preprocessing (this is executed once immediately after reading the material data)*

Read and store as many sets of 12 stress-strain curves obtained at constant strain rate and temperature as needed. Convert these curves to stress versus effective plastic strain using equation2.60. Store initial yield stresses in q, based off the initial strain rate and temperature.

The following steps are executed when the material model subroutine is called for each Gauss point in all the elements at every time step.

Step 2: *Initialization*

The following parameters are passed to the subroutine: $\boldsymbol{\sigma}_n$, $(\dot{\boldsymbol{\varepsilon}}_n, \Delta t_n)$.

Step 3: *Elastic predictor*

(a) Compute the yield function coefficients using equations 2.5, 2.7/2.10, 2.8/2.11, and 2.9/2.12 for yield stresses based on the current temperature and strain rate. Calculate off-axis coefficients based on convexity conditions using equation 2.48, if necessary. It should be noted that the aforementioned “yield stresses” are taken as the stress values corresponding to the specified yield strain value for the first time step. From the second

time step onwards, the yield stresses are taken corresponding to the previous value of effective plastic strain, λ . If λ is beyond the end of the curve in consideration, the curve is extrapolated with a slope which is equal to one percent of the corresponding elastic stiffness.

(b) Construct the elastic stiffness matrix using equation 2.62, interpolating the elastic moduli based on the current temperature and strain rate.

(c) Compute elastic trial stresses, $\boldsymbol{\sigma}_{n+1}^{e}$, using equation 2.61.

(d) Compute the trial yield function, f_{n+1}^{trial}, using the elastic trial stresses in equation 2.1. If $f_{n+1}^{trial} \le \delta_{tol}$, the current state is elastic. Set $\Delta\lambda_n = 0$ and go to stress update (Step 5), else go to plastic corrector (Step 4).

Step 4: *Plastic corrector*

(a) Set $\Delta\lambda^1 = 0$.
(b) Calculate $\Delta\lambda^2$ from equation 2.68.
(c) Compute the new estimate of the stress for each effective plastic strain increment $\left(\Delta\lambda^1, \Delta\lambda^2\right)$ using equation 2.71.
(d) Calculate the effective plastic strains at the next time step as:
$\lambda^1 = \lambda_n + \Delta\lambda^1, \lambda^2 = \lambda_n + \Delta\lambda^2$.
(e) Update the yield stresses using equation 2.79.
(f) Determine the corresponding yield function coefficients for each increment based on the updated yield stresses using equations 2.5, 2.7/2.10, 2.8/2.11, and 2.9/2.12; calculate off-axis coefficients based on convexity conditions using equation 2.48, if necessary.
(g) Calculate the yield function values using equation 2.1. For a negative $\Delta\lambda^2$: if $\lambda > 0$ set $\Delta\lambda^2 = \lambda$, else if $\lambda = 0$, $\Delta\lambda^2 = abs(\Delta\lambda^2)$.
(h) Calculate the yield function for $\Delta\lambda^2$: if $f_2 < 0$ then use the current value of $\Delta\lambda^2$, else increase $\Delta\lambda^2$ by a factor until $f_2 < 0$. This increasing $\Delta\lambda^2$ by a factor is done n_{double} times, to ensure the solution is bounded. If the solution is NOT bounded after n_{double} cycles, bound the solution using robust technique using the following algorithm:

(i) Set $\Delta\lambda^1 = 0$ and compute $f(\Delta\lambda^1) = f_1$.
(ii) Set $step = \Delta\lambda^2$.
(iii) Set $X_2 = \Delta\lambda^2$ and compute $f(X_2) = f(\Delta\lambda^2) = f_2$.
(iv) If $f_2 < 0$ $\Delta\lambda^2$ bounds the solution, and hence exit the algorithm.
(v) $step = factor * step$.
(vi) $X_3 = X_2 + step = \Delta\lambda^2 + step$, compute $f(X_3) = f_3$.

(vii) If $f_3 < 0$, X_3 bounds the solution, and hence exit the algorithm.

(viii) If $f_1 > f_2 > f_3$ or $f_1 < f_2 < f_3$, set $X_1 = X_2$ and $X_2 = X_3$. Go to step v.

(ix) $X_{mid} = \dfrac{X_2 + X_3}{2}$ and compute $f(X_{mid}) = f_{mid}$.

(x) If $f_{mid} < 0$, X_{mid} bounds the solution, and hence exit the algorithm.

(xi) Given that if $f_1 > f_2$, if $f_2 < f_3$ then set $X_3 = X_{mid}$ and go to step ix or else if $f_2 > f_3$ then set $X_2 = X_{mid}$ and go to step ix.

(xii) Given that if $f_1 < f_2$, if $f_2 < f_3$ then set $X_2 = X_{mid}$ and go to step ix or else if $f_2 > f_3$ then set $X_3 = X_{mid}$ and go to step ix.

(xiii) Go to Step v.

(i) Compute new plastic multiplier increment, $\Delta\lambda^3$, from equation 2.72.

(j) Calculate the updated stresses using equation 2.73 and the new estimate for the yield function, f^3.If $\left|f^3\right| \le \delta_{tol}$, set $\Delta\lambda = \Delta\lambda^3$, exit the loop and go to stress update (step 5); else update secant iteration parameters using equation 2.74 and proceed with secant iterations.

(k) Loop through secant iteration for $n_{sec\max}$ iterations:

(i) Calculate new estimate of the increment of effective plastic strain, $\Delta\lambda^{i+1}$, using equation 2.75.

(ii) Compute the updated stresses for the new estimate of the increment using equation 2.71.

(iii) Update total effective plastic strain $\lambda_{n+1}^{i+1} = \lambda_n + \Delta\lambda_{n+1}^{i+1}$.

(iv) Update yield stresses using equation 2.79.

(v) Calculate the yield function value, f^{i+1}, using equation 2.1; calculate off-axis coefficients based on convexity conditions using equation 2.48, if necessary.

(vi) Update the derivative of the plastic potential, $\left.\dfrac{\partial h}{\partial \sigma}\right|_{n+1}^{i+1}$.

(vii) If $\left|f^{i+1}\right| \le yieldtol$, set $\Delta\lambda = \Delta\lambda^{i+1}$, exit the loop and go to stress update; else update secant iteration parameters using equation 2.77 and go to next step of secant iteration.

(viii) If secant method hits $n_{\sec\max}$, a more robust technique is used. The robust technique uses the bounds on the root and Brent's method for root finding [31] to find the plastic multiplier increment within the specified tolerance.

Step 5: *Stress Update*

Calculate $\boldsymbol{\sigma}_{n+1}$ using equation 2.71.

Step 6: *History Variable Update*

Update history variables for plastic work and work hardening parameters (q, $\hat{\mathbf{d}}$, and λ).

(a) Set $\lambda_{n+1} = \lambda_n + \Delta\lambda_n$.

(b) Determine new yield stresses, $\mathbf{q}_{n+1}$, using equation 2.79.

It should be noted that $\boldsymbol{\sigma}_{n+1}$ is updated and passed back from the subroutine for use in the rest of LS-DYNA functionalities.

2.3 MODEL VERIFICATION

The verification is carried out using T800S/F3900 composite. A minimum of twelve material stress-strain curves are required as input for MAT213, which are obtained from the experiments. The properties of the composite obtained from the experiments [22] on the coupon level are shown in Table 2-2. The verification tests are carried out using single element FE models initially. The single element verification model are cubes of dimension 1 in x 1 in x 1 in. Multi-element verification tests are carried out where the models have the same geometry as that of the ones used in the experiments. The FE models were made using LS-PrePost V4.6 [32].

Table 2-2. Material Properties

Property	**Value (Tensile)**	**Value (Compressive)**
1-direction modulus (E_{11}, psi)	23.5 x10^6(162 GPa)	18.7 x 10^6 (128 GPa)
2-direction modulus (E_{22}, psi)	1.07 x10^6 (7.3 GPa)	1.12 x10^6 (7.7 GPa)
3-direction modulus (E_{33}, psi)	9.66 x10^5 (6.6 GPa)	1.04 x10^6 (7.1 GPa)
1-2 plane shear modulus (G_{12}, psi)	5.80 x10^5 (3.9 GPa)	
2-3 plane shear modulus (G_{23}, psi)	3.26 x10^5(2.2 GPa)	
1-3 plane shear modulus (G_{13}, psi)	3.48 x10^5 (2.3 GPa)	
Poisson's ratio (v_{12})	0.317	0.342
Poisson's ratio (v_{23})	0.484	0.728
Poisson's ratio (v_{13})	0.655	0.578
Poisson's ratio (v_{21})	0.0168	0.0207
Poisson's ratio (v_{32})	0.439	0.676

Property	Value (Tensile)	Value (Compressive)
Poisson's ratio (v_{31})	0.027	0.032
Density (ρ, slugs/in^3)	$1.457\ 10^{-4}$	

2.3.1 Determination of Flow-Rule coefficients

The flow rule coefficients are calculated using (a) the flow law from equation 2.22, and (b) the Poisson's ratio of the plastic strains to derive a set of functions relating the flow rule coefficients to the plastic Poisson's ratios. A general form of these equations was rewritten in terms of the plastic Poisson's ratios and H_{11} in equation 2.40. However, this requires a known value of H_{11}. Since the T800/F3900 composite is unidirectional and transversely isotropic in the 2- and 3-directions, a simplified procedure described in chapter 2 can be applied. The parameters H_{11}, H_{12}, and H_{13} are assumed to be zero, from:

$$\dot{\varepsilon}_{11}^{p} = \frac{\dot{\lambda}}{2h}\left(2H_{11}\sigma_{11} + 2H_{12}\sigma_{22} + 2H_{13}\sigma_{33}\right) = 0 \quad \Rightarrow \quad H_{11} = H_{12} = H_{13} = 0$$

and equation 2.35 holds true, so H_{22} must be equal to 1. The flow law coefficient, H_{33}, can be assumed to be one as well, due to the assumption of transverse isotopy. The remaining value, H_{23}, can be determined using equation 2.36, and is computed as -0.7760. It should be noted that the flow law coefficients are assumed to be constant, which implies a constant value of the plastic Poisson's ratio, ν_{23}^{p}, and is determined as an average value from unidirectional transverse (2-direction) tension test data.

The final three flow law coefficients H_{44}, H_{55}, and H_{66}, are determined using the same fit technique as in the simplified case, discussed in chapter 2. However, each shear curve must be fit with the 2-direction test acting as the baseline. Using the same method as described with equation 2.44, the objective function for the problem can be rewritten in terms of the 2-direction baseline as:

$$f(\mathrm{H}_{ll}) = \sum_{k=1}^{n}\left[\left(\hat{\sigma}_{22}\right)_k - \left(\hat{\sigma}_{ij}\right)_k\right]^2 \qquad 2.80$$

Results from this exercise in terms of computing the optimal flow-rule coefficients (solution to equation 2.80) are shown in Figure 2-6, Figure 2-7, and Figure 2-8. These plots show the results for the minimized difference between the shear and base curve in the effective stress vs. effective plastic strain space, equation 2.80. However, the two curves do not exactly match, as the effect of the flow rule coefficient values do not fundamentally change the shape of the shear curves.

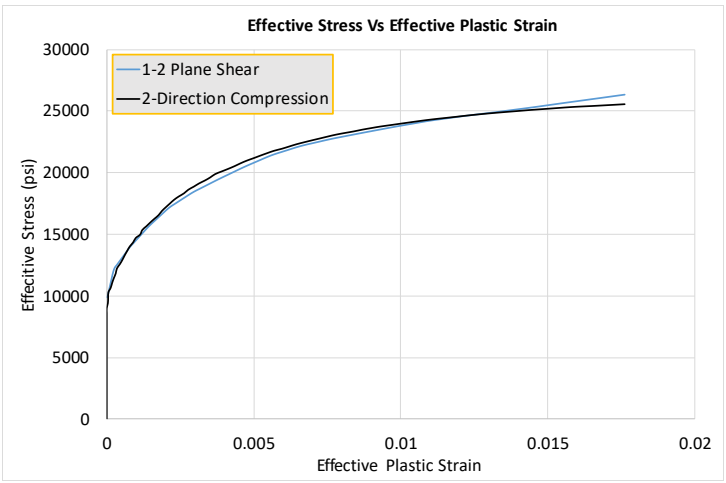

Figure 2-6. Comparison of master curve with optimized H44 value

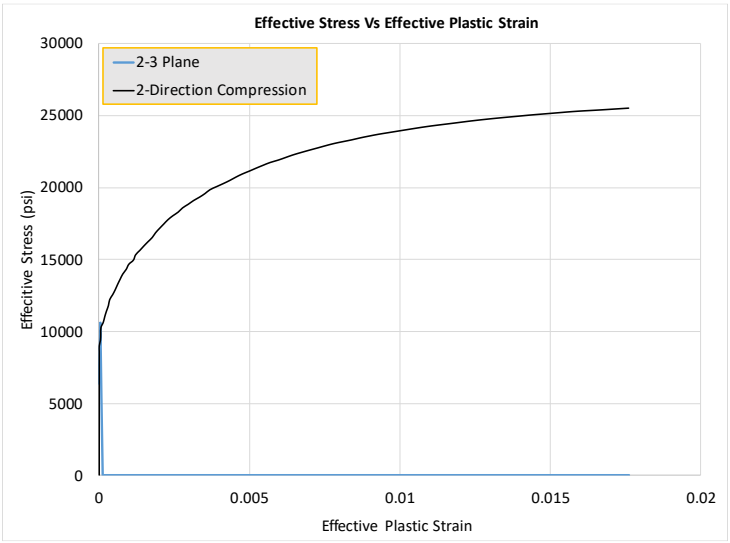

Figure 2-7. Comparison of master curve with optimized H55 value

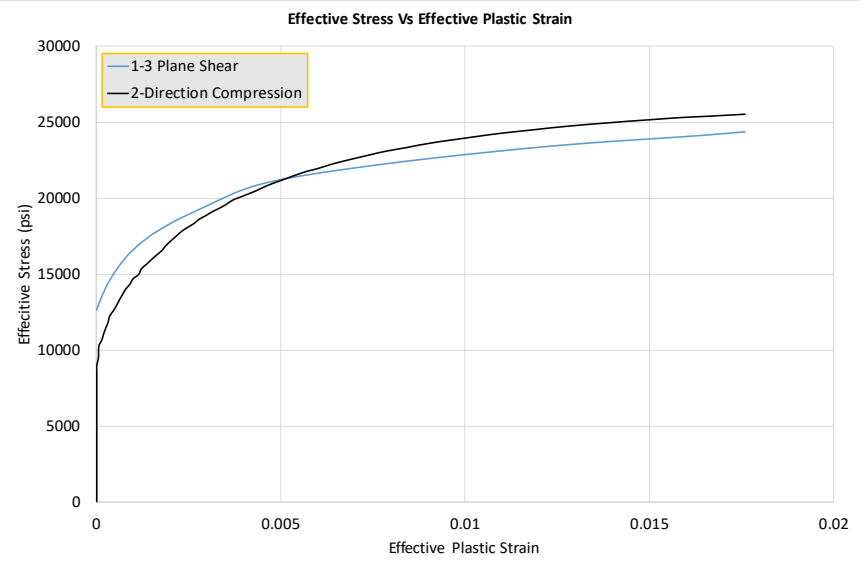

Figure 2-8. Comparison of master curve with optimized H66 value

A summary of all the flow law coefficient values is shown in Table 2-3 below.

Table 2-3. Flow Law Coefficients for T800-F3900 Composite

Coefficient	Value
H_{11}	0.0000
H_{22}	1.0000
H_{33}	1.0000
H_{12}	0.0000
H_{23}	-0.7760
H_{13}	0.0000
H_{44}	4.2390
H_{55}	15.3100
H_{66}	5.3718

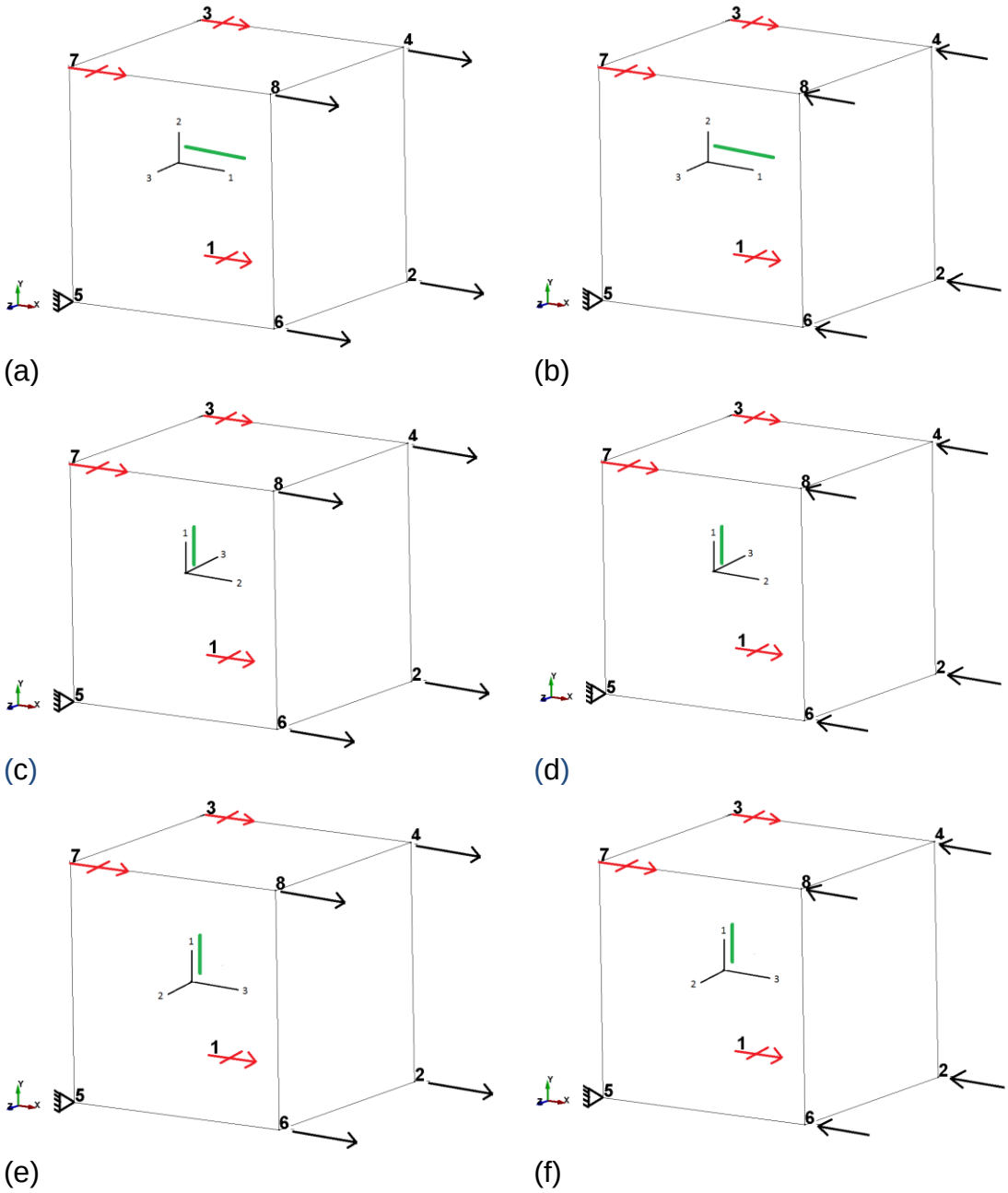

Figure 2-9. Schematic diagram for (a) 1-direction tension model, (b) 1-direction compression model, (c) 2-direction tension model, (d) 2-direction compression model, (e) 3-direction tension model, (f) 3-direction compression model

2.3.2 Single Element Verification Test

In the schematic diagrams of the single element model used (Figure 2-9, Figure 2-10, and Figure 2-11), all the translational displacements are restrained at the pin support. The red arrow with a cut represents a restrain in the translational displacement along

the direction the arrow is pointed. The black color arrows represent a displacement applied to the node in the corresponding direction at a rate of 0.5 in/s. The blue and the violet color arrows represent a force applied on the face connected by the nodes on which these arrows are placed. The green color line represents the orientation of the fiber in the composite.

Each of these elements are 1 in x 1 in x 1 in cube. 8-noded hexahedral solid elements are used with ELFORM 1 (1-direction tension, 2-direction tension, 3-direction tension, 1-2 plane 45° off-axis tension) or 2 (1-direction compression, 2-direction compression, 3-direction compression, 1-2 plane shear, 2-3 plane shear, 1-3 plane shear, 2-3 plane 45° off-axis compression, 1-3 plane 45° off-axis compression). Unless otherwise stated, the loading rate is 0.5 in/s.

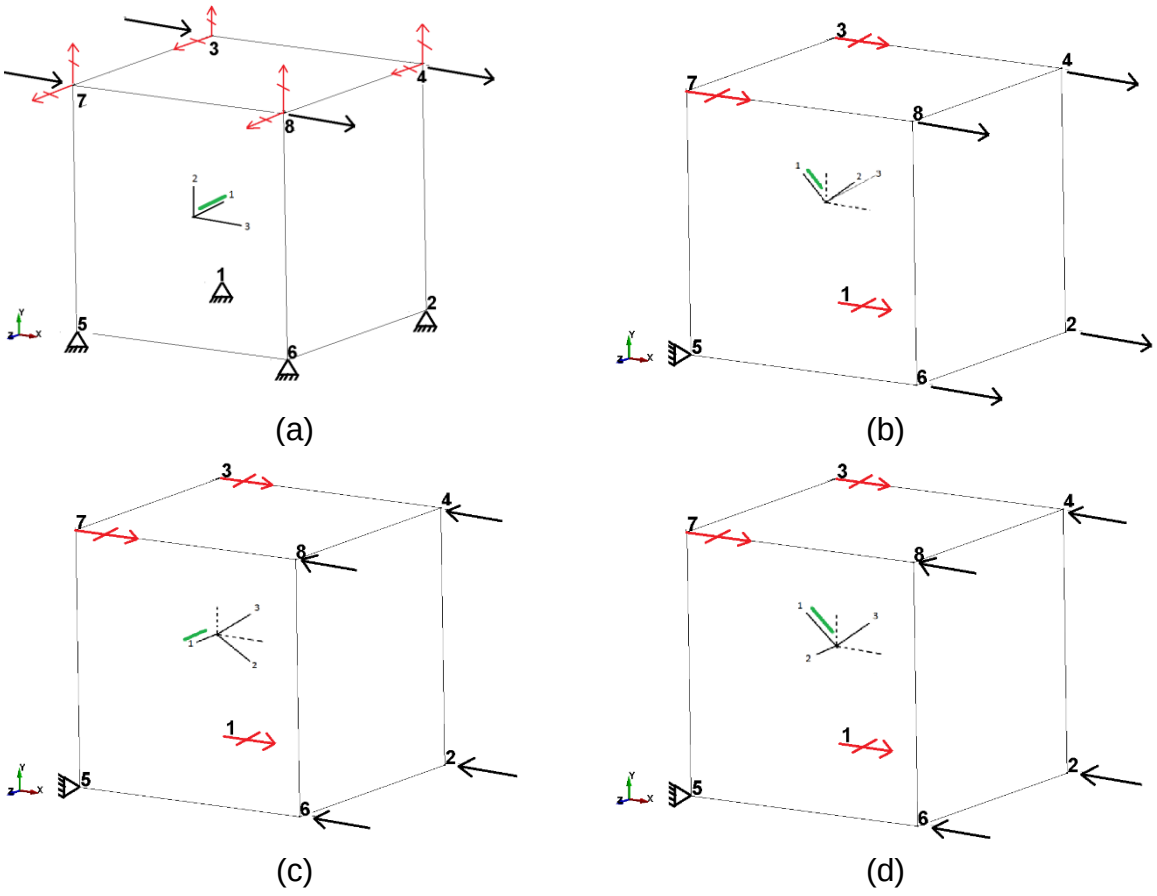

Figure 2-10. Schematic diagram for (a) 2-3 plane shear model, (b) 1-2 plane 45° off-axis tension model, (c) 2-3 plane 45° off-axis compression model, (d) 1-3 plane 45° off-axis compression model

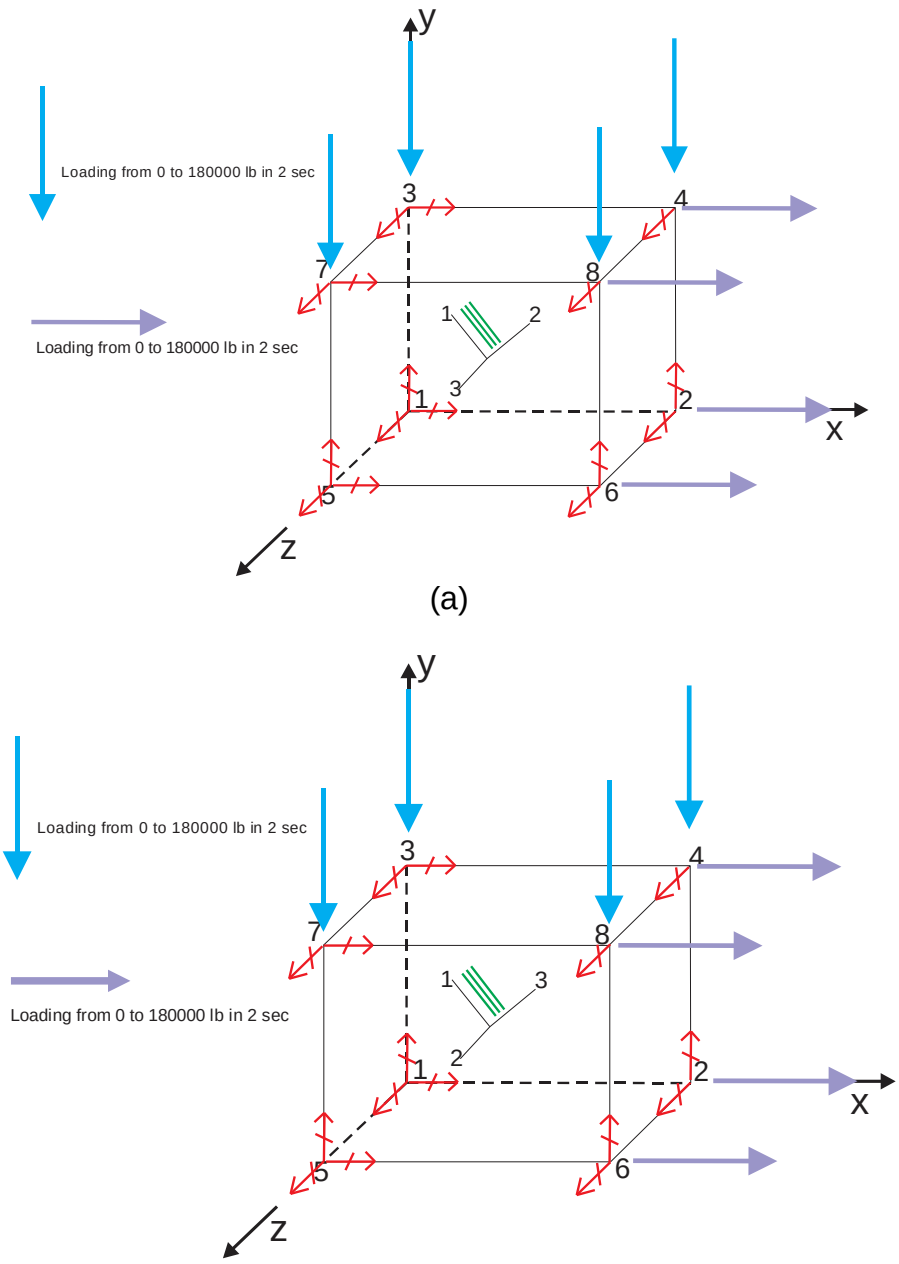

Figure 2-11. Schematic Diagram for (a) 1-2 plane shear model, (b) 1-3 plane shear model

In each of the stress-strain curves shown, the blue color curve represents the experimental data (input data for MAT213). The dashed black curve is obtained from MAT213 simulation using deformation model.

2.3.2.1 1-Direction Tension Test and 1-Direction Compression Test

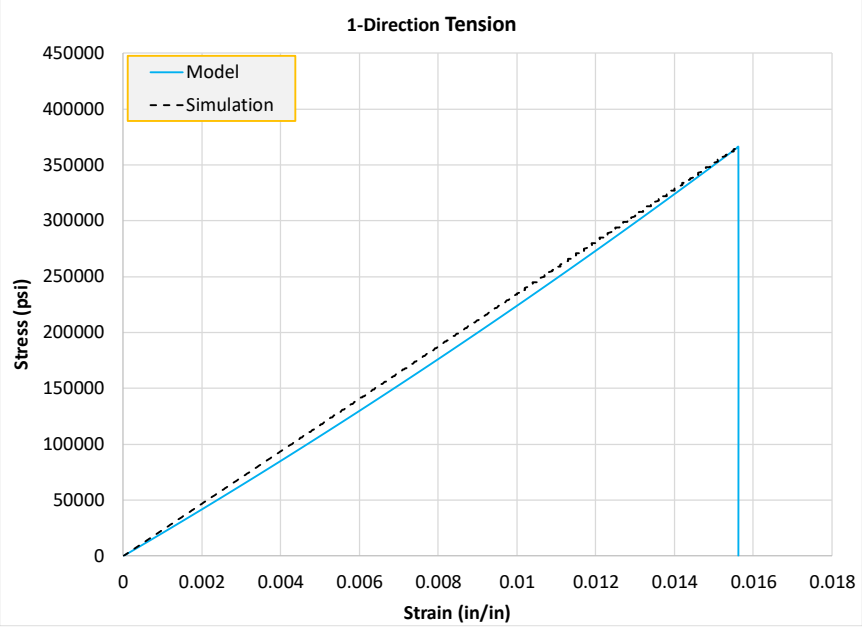

Figure 2-12. 1-Direction Tension Stress-Strain Plot

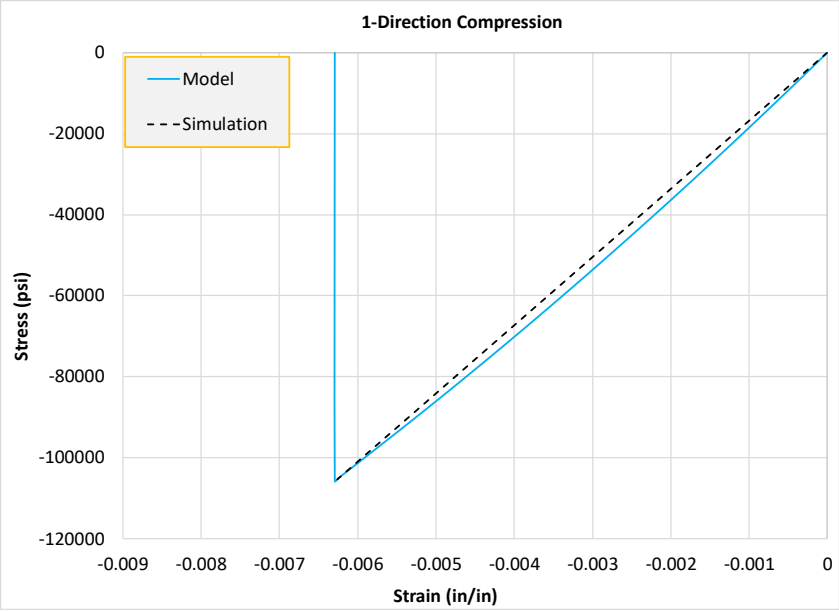

Figure 2-13. 1-Direction Compression Stress-strain plot

The simulation stress-strain curve in Figure 2-12 and Figure 2-13 remains linearly elastic because tension and compression in 1-Direction is set to be linearly elastic in the material card, i.e., the onset of initial plastic strain is set to a value of 1.

2.3.2.2 2-Direction Tension Test and 2-Direction Compression Test

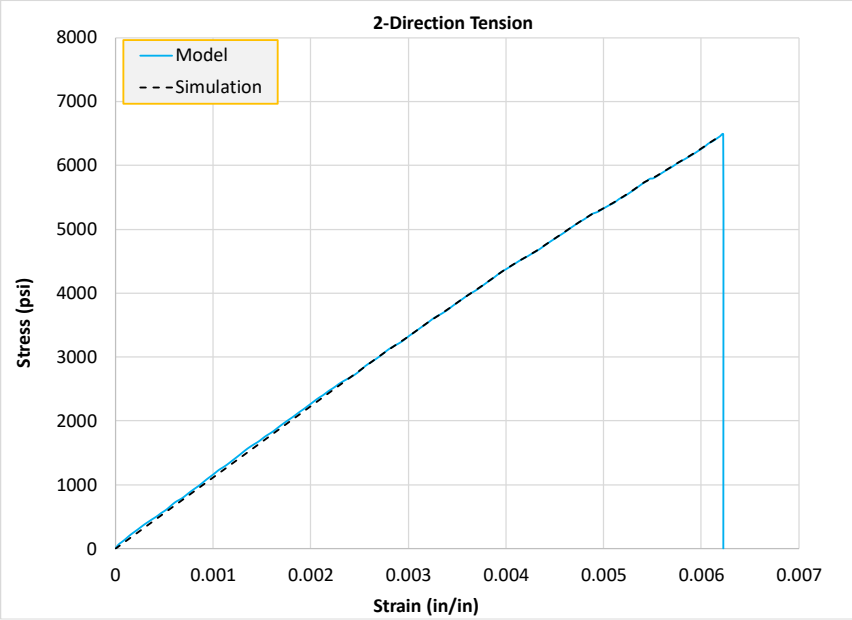

Figure 2-14. 2-Direction Tension Stress-Strain Plot

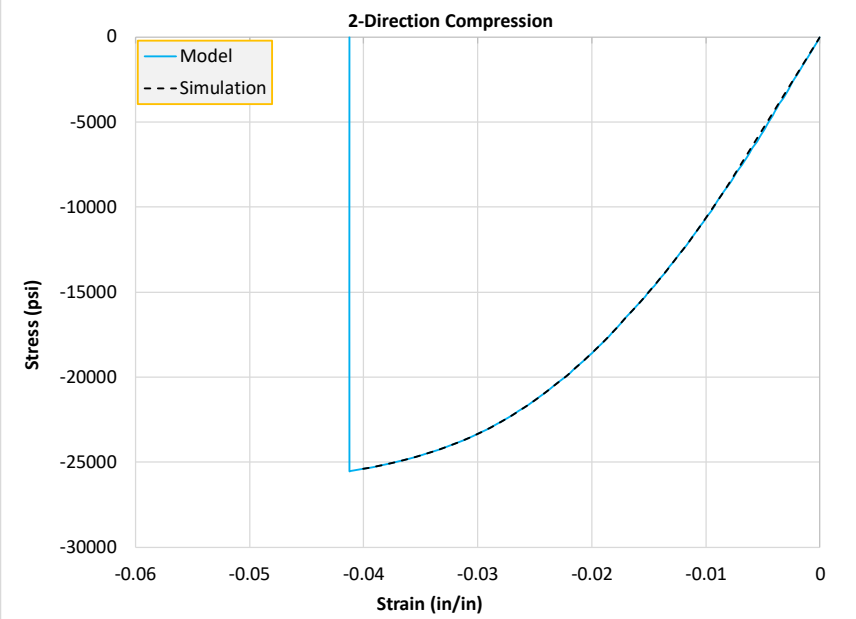

Figure 2-15. 2-Direction Compression Stress-Strain Plot

The simulation stress-strain curve in Figure 2-14 and Figure 2-15 remains linear until a strain value of 0.00267 and 0.0083, respectively, and then the plasticity can be observed.

2.3.2.3 3-Direction Tension Test and 3-Direction Compression Test

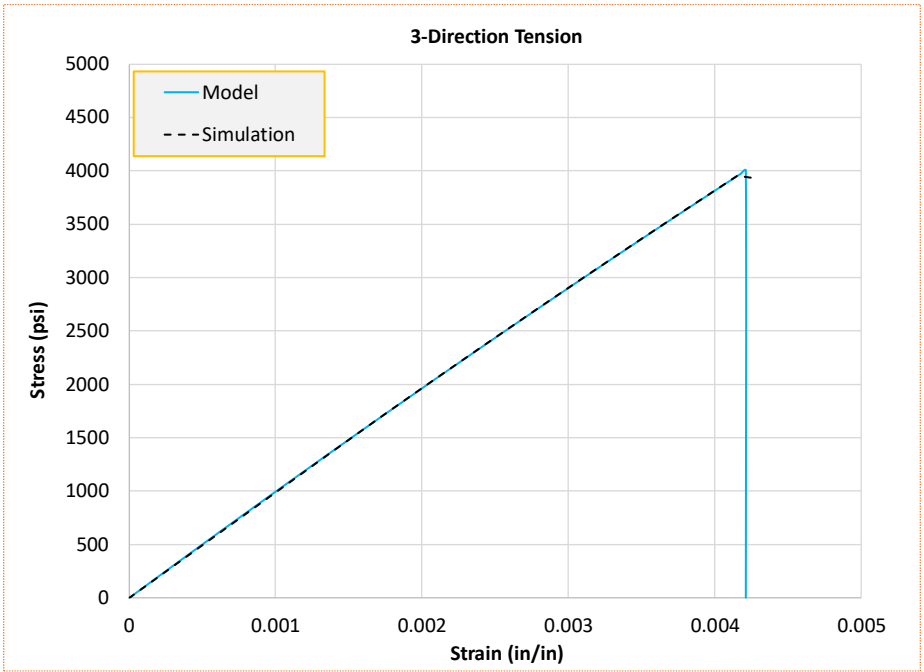

Figure 2-16. 3-Direction Tension Stress-Strain Plot

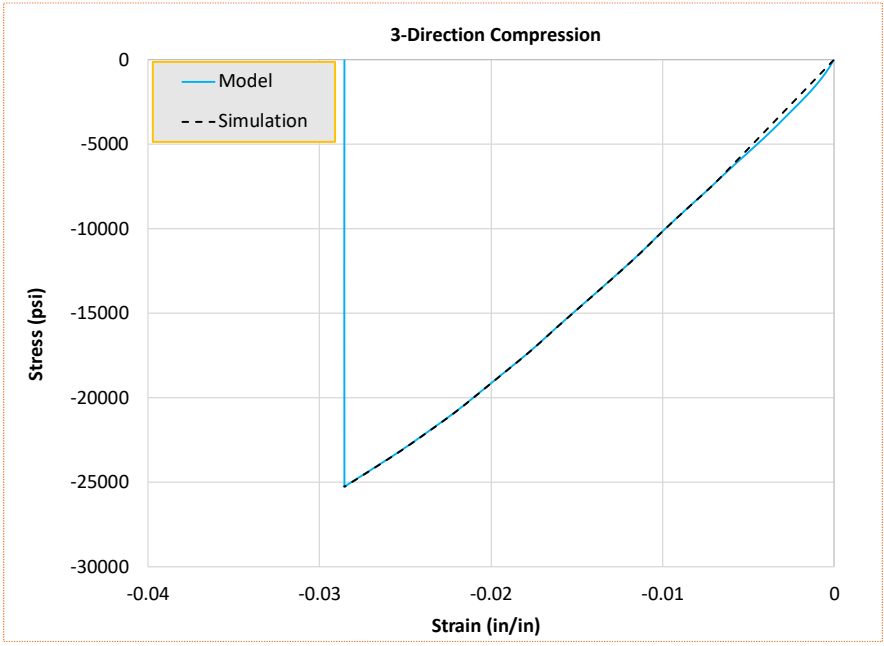

Figure 2-17. 3-Direction Compression Stress-Strain plot

The simulation stress-strain curve in Figure 2-16 and Figure 2-17 remains linear until strain values of 0.00160 and 0.00688, respectively, and then the plasticity is observed.

2.3.2.4 1-2 Plane Shear Test

For this test a load-controlled FE model is used to obtain a state of pure shear in the 1-2 plane.

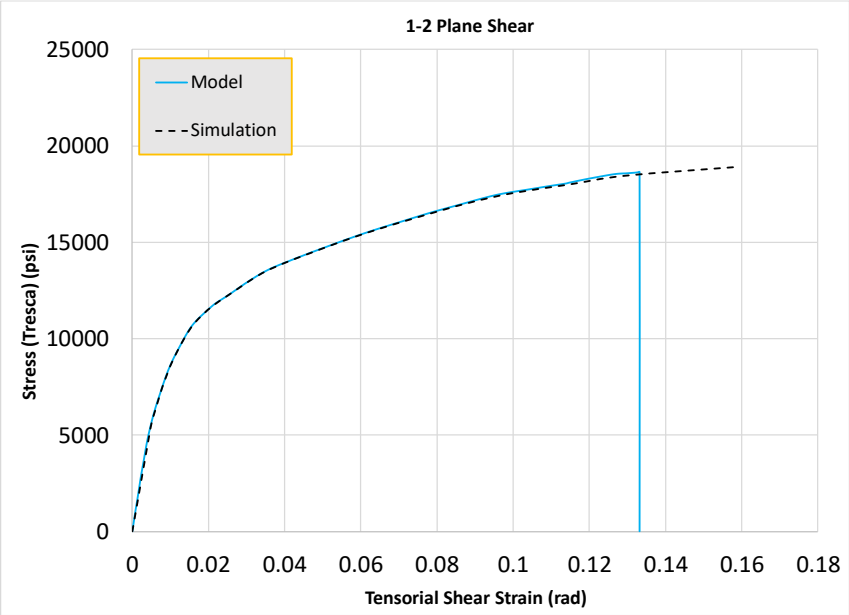

Figure 2-18. 1-2 Plane Shear Stress-Strain Plot

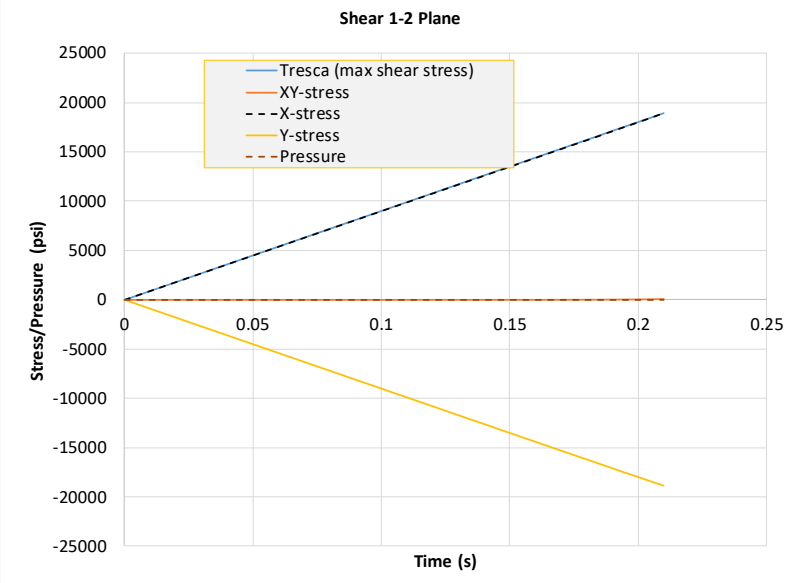

Figure 2-19. Stress/pressure quantity against time

The simulation stress-strain curve in Figure 2-18 is obtained by plotting Tresca stress against the strain in x-direction. Additional stress plots are shown in Figure 2-19 to check whether the model is in pure shear or not.

2.3.2.5 2-3 Plane Shear Test

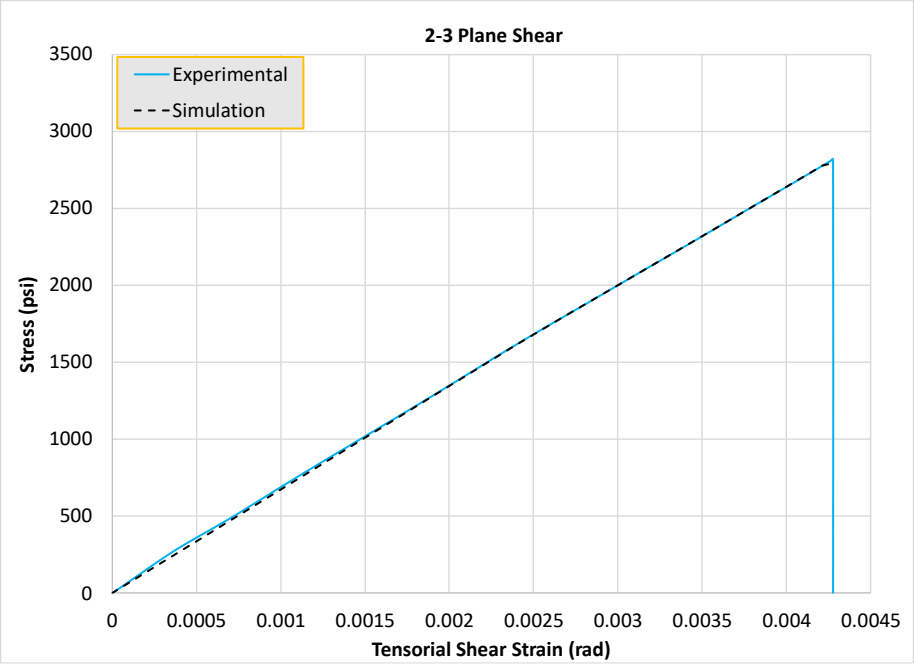

Figure 2-20. 2-3 Plane Shear Stress-Strain Plot

The simulation stress-strain curve remains linear until the strain reaches a value of 0.00245, after which plasticity is observed, although the curve looks linear throughout.

2.3.2.6 1-3 Plane Shear Test

The model used for this test is similar to the one used for the 1-2 plane shear test. The only difference is in the orientation of the PMDs.

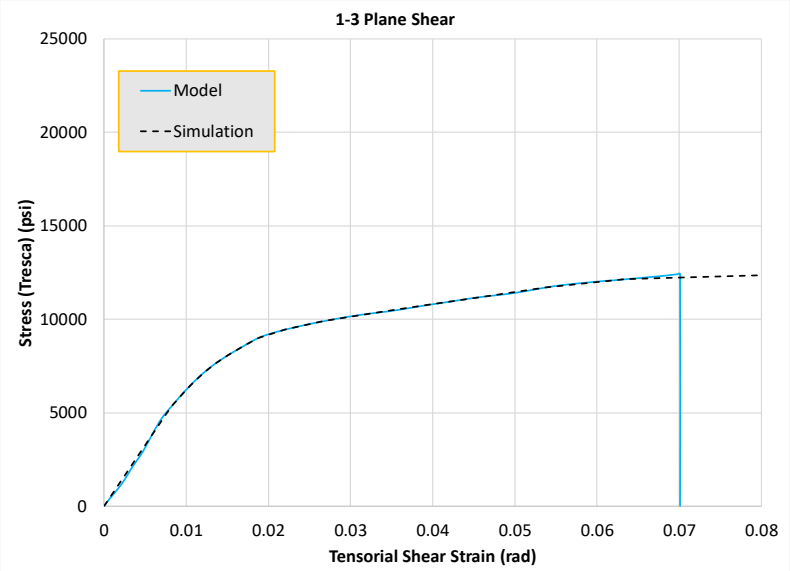

Figure 2-21. 1-3 Plane Shear Stress-Strain Plot

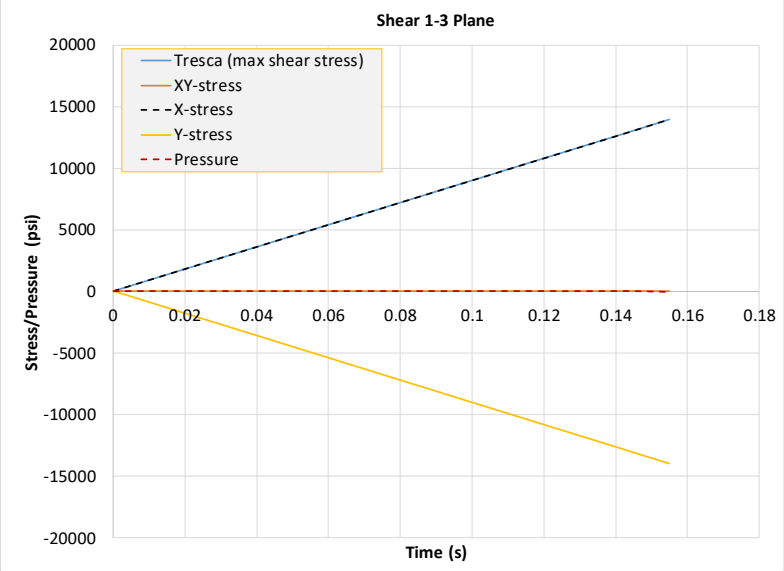

Figure 2-22. 1-3 Plane Shear Stress-Strain Plot

The simulation stress-strain curve in Figure 2-21 is obtained by plotting Tresca stress against the strain in x-direction. Additional stress plots are shown in Figure 2-22 to check whether the model is in pure shear.

2.3.2.7 1-2 Plane 45° Off-Axis Tension

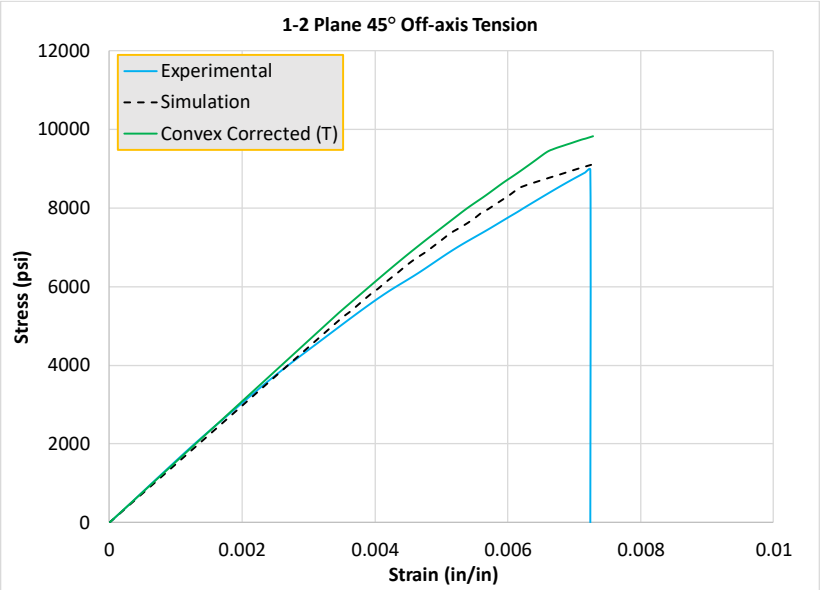

Figure 2-23. 1-2 Plane 45° Off-Axis Tension Stress-Strain Plot

The simulation stress-strain curve in Figure 2-23 remains linear until the strain reaches a value of 0.00160, after which plasticity is observed. The simulation curve has stress values higher than the input curve (blue color curve) because of the convexity correction applied. The green color plot represents the convex corrected curve calculated using the tension equation.

2.3.2.8 2-3 Plane 45° Off-Axis Compression

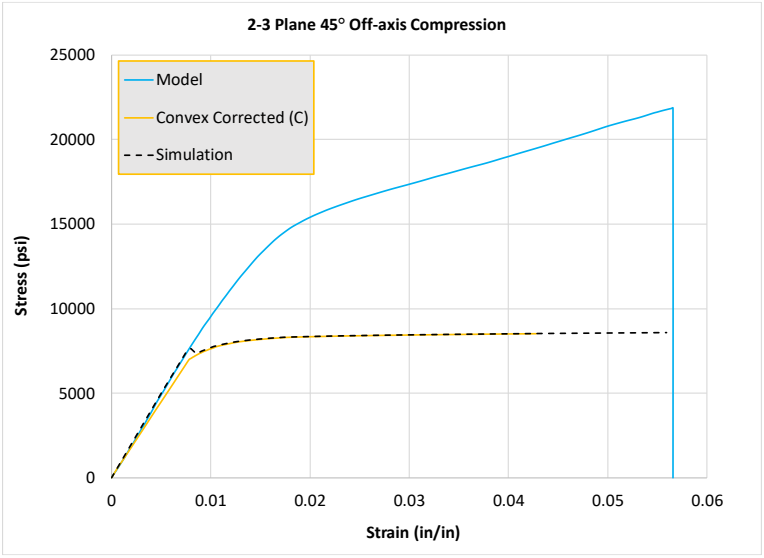

Figure 2-24. 2-3 Plane 45° Off-Axis Compression Stress-Strain Plot

The simulation stress-strain curve (Figure 2-24) remains linear until the strain reaches a value of 0.00160, after which plasticity is observed. The simulation curve (dashed black plot) overlaps the convex corrected curve (yellow color plot) using the compression equation as expected.

2.3.2.9 1-3 Plane 45° Off-Axis Compression

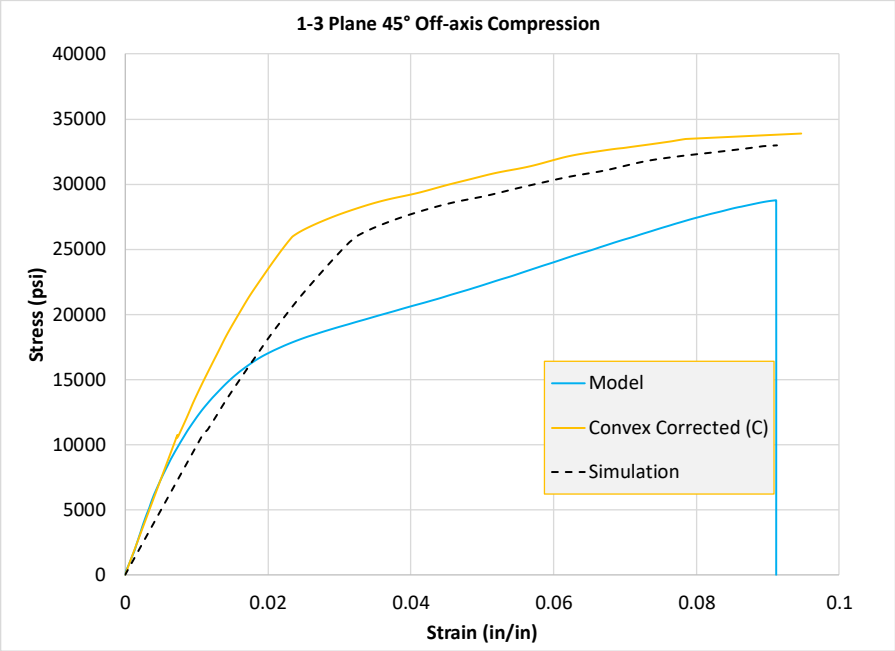

Figure 2-25. 1-3 Plane 45° Off-Axis Compression Stress-Strain Plot

The simulation curve (dashed black plot) as shown in Figure 2-25 is softer than the convex corrected curve (yellow plot) as the input curve is not directly used for the calculation of the initial stiffness.

2.3.3 Multi-Element Verification Test

For the multi-element verification tests, the experimental geometries were used to perform each respective simulation. All simulations utilized 8-noded hexahedron solid elements used with ELFORM 1 (1-direction tension, 2-direction tension, 3-direction tension, 1-2 plane 45° off-Axis tension) or ELFORM 2 (1-direction compression, 2-direction compression, 3-direction compression, 1-2 plane shear, 2-3 plane shear, 1-3 plane shear, 2-3 plane 45° off-axis compression, 1-3 plane 45° off-axis compression).

2.3.3.1 1-Direction Tension Test

The schematic diagram of the model used for this simulation is shown in Figure 2-26. The model dimensions are also shown. The green color lines represent the orientation of the fibers.

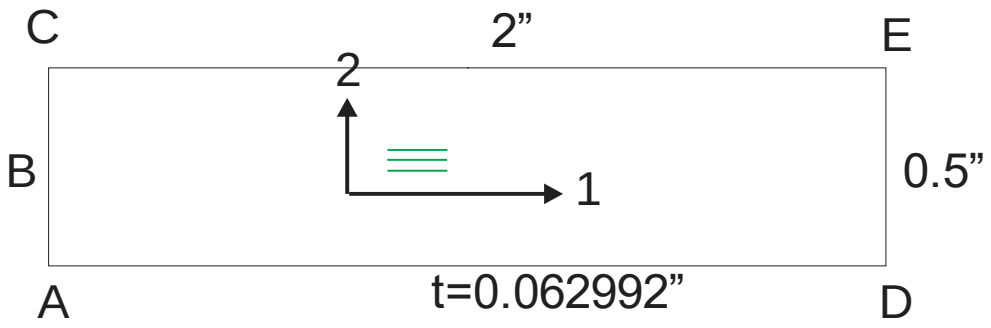

Figure 2-26. 1-direction tension model schematic diagram

The translational displacements along x-, y-, and z-directions are restrained at the pinned support. The translational displacement along x-direction is restrained at the roller supports. The FE model is shown in fFigure 2-27 along with the support representations. The total number of elements in the model is 64. There is 1 element through the thickness. Velocity of 0.5 in/s is applied at the nodes on the right face of the model in the positive x-direction.

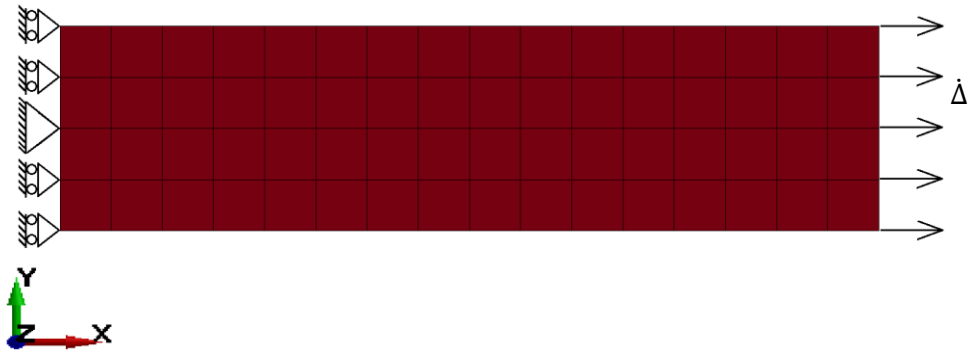

Figure 2-27. 1-direction tension FE model

The middle four elements are considered for the post-processing. The average of the stress-strain data of these four elements are taken into consideration. The stress-strain curve is shown in Figure 2-28. The blue curve represents the experimental data (input data for MAT213). The dotted black curve is obtained from MAT213 simulation.

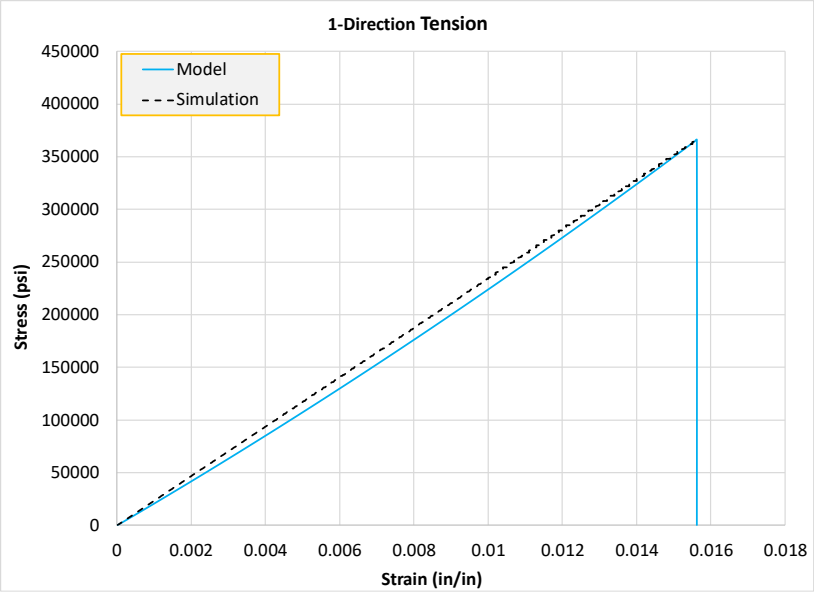

Figure 2-28. 1-direction tension stress-strain plot

The simulation stress-strain curve (Figure 2-28) obtained from the simulation remains linearly elastic because tension in 1-direction is set to be linearly elastic in the material card, i.e., the onset of initial plastic strain is set to a value of 1.

2.3.3.2 1-Direction Compression Test

The schematic diagram of the model used for this simulation is shown in Figure 2-29. The model dimensions are also shown. The green color lines represent the orientation of the fibers.

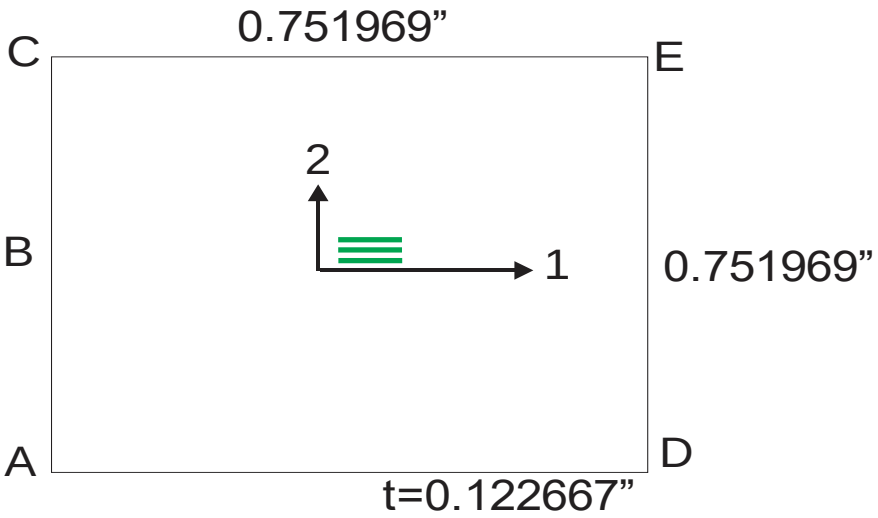

Figure 2-29. 1-direction compression model schematic diagram

The FE model used for this test is shown in Figure 2-30 along with the support representations. The total number of elements in the model is 64. There is 1 element through the thickness. Velocity of 0.5 in/s is applied at the nodes on the right face of the model in the negative x-direction.

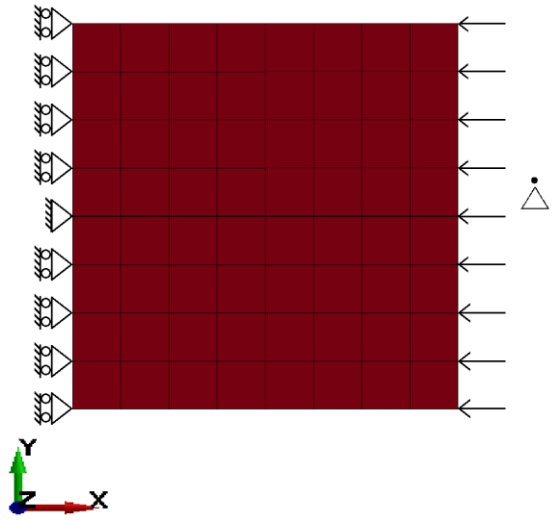

Figure 2-30. 1-direction compression FE model

The middle four elements are considered for the post-processing. The average of the stress-strain data of these four elements are taken into consideration. The stress-strain curve is shown in Figure 2.31. The blue curve represents the experimental data (input data for MAT213).

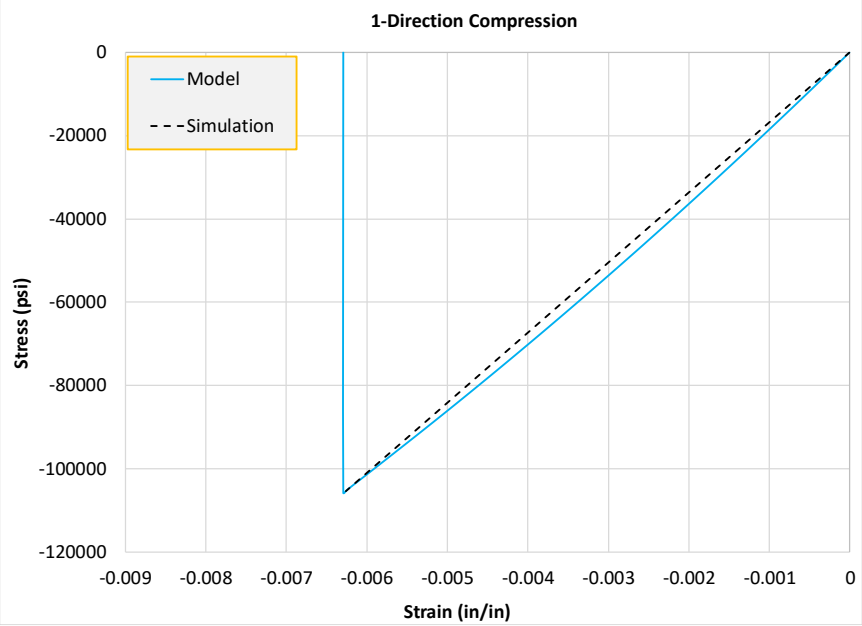

Figure 2.31. 1-direction compression stress-strain plot

The simulation stress-strain curve (Figure 2.31) obtained from the simulation remains linearly elastic because compression in 1-direction is set to be linear elastic in the material card, i.e., the onset of initial plastic strain is set to a value of 1.

2.3.3.3 2-Direction Tension Test

The schematic diagram of the model used for this simulation is shown in Figure 2-32. The model dimensions are also shown. The green color lines represent the orientation of the fibers.

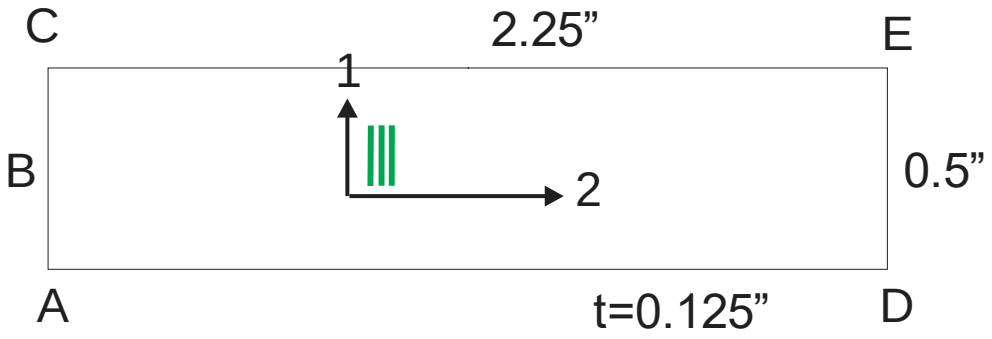

Figure 2-32. 2-direction tension schematic diagram

The FE model used for this test is shown in Figure 2-33 along with the support representations. The total number of elements in the model is 512. There are 2 elements through the thickness. There are 3 nodes through the thickness. Only the central node at the left face is pinned and the rest of the nodes on the left face have roller supports. Velocity of 0.5 in/s is applied at the nodes on the right face of the model in the positive x-direction.

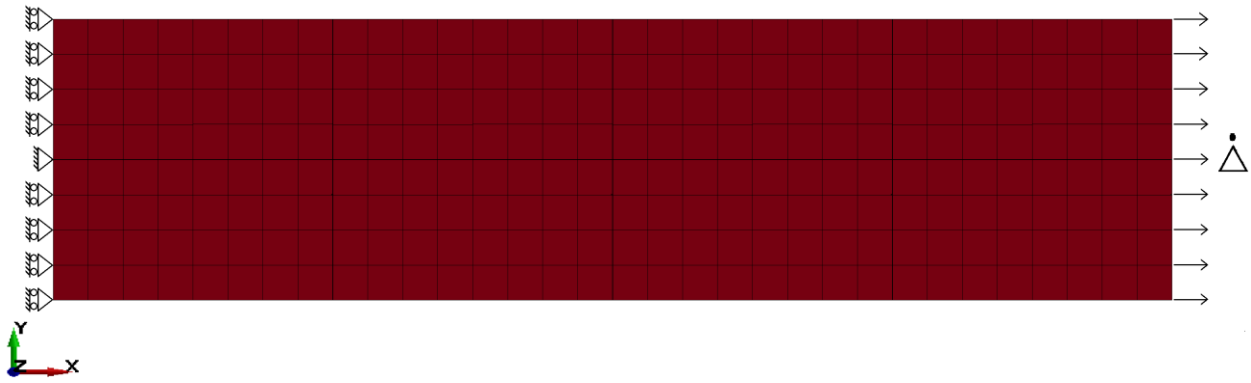

Figure 2-33. 2-direction tension FE model

The middle 8 elements are considered for the post-processing. The average of the stress-strain data of the middle 8 (2 elements through the thickness) elements are taken into consideration. The stress-strain curve is shown in Figure 2-34.

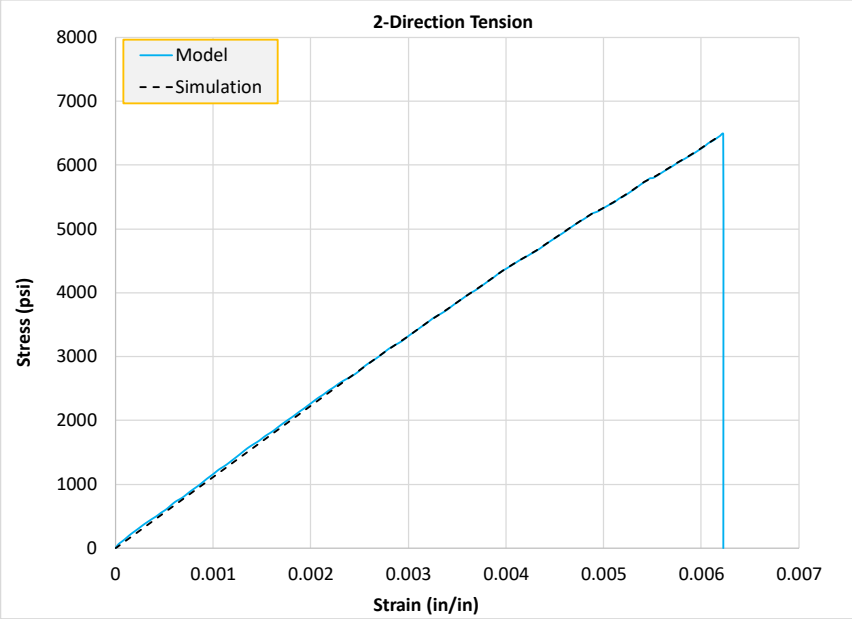

Figure 2-34. 2-direction tension stress-strain plot

The simulation stress-strain curve (Figure 2-34) remains linear until a strain value of 0.00267, and then the plasticity can be observed.

2.3.3.4 2-Direction Compression Test

The schematic diagram of the model used for this simulation is shown in Figure 2-35. The model dimensions are also shown. The green color lines represent the orientation of the fibers.

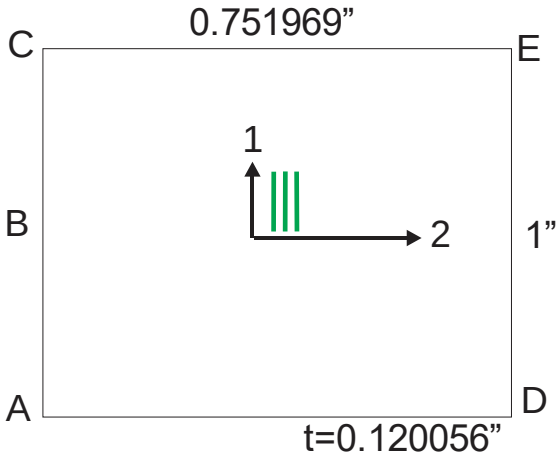

Figure 2-35. 2-direction compression model schematic diagram

The FE model used for this test along with the boundary conditions are shown in Figure 2-36. There is a total of 64 elements with 1 element through the thickness.

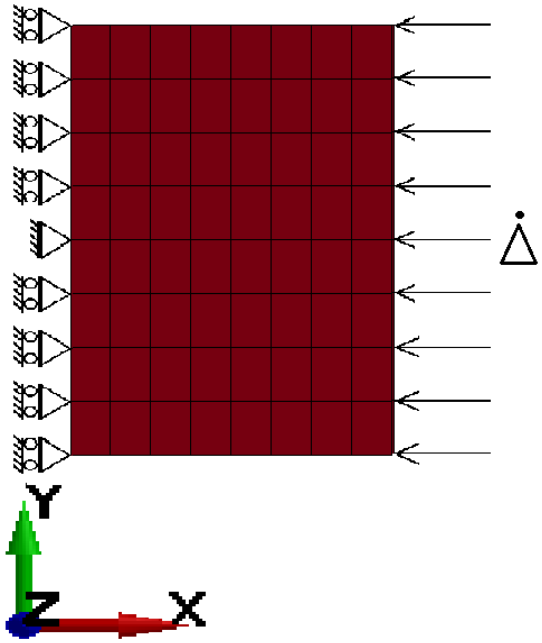

Figure 2-36. 2-direction compression FE model

The post-processing is done in a similar way as discussed for the 1-direction compression test. The stress-strain curve is shown in Figure 2-37.

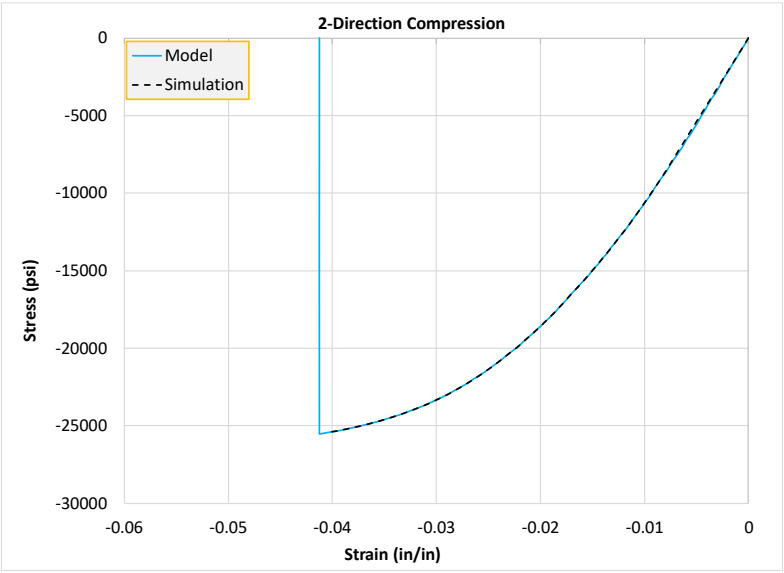

Figure 2-37. 2-direction compression stress-strain plot

The simulation stress-strain curve (Figure 2-37) remains linear until the strain reaches a value of 0.00830, after which plasticity is observed.

2.3.3.5 3-Direction Tension Test

The schematic diagram of the model used for this simulation is shown in Figure 2-38. The model dimensions are also shown. The green color lines represent the orientation of the fibers.

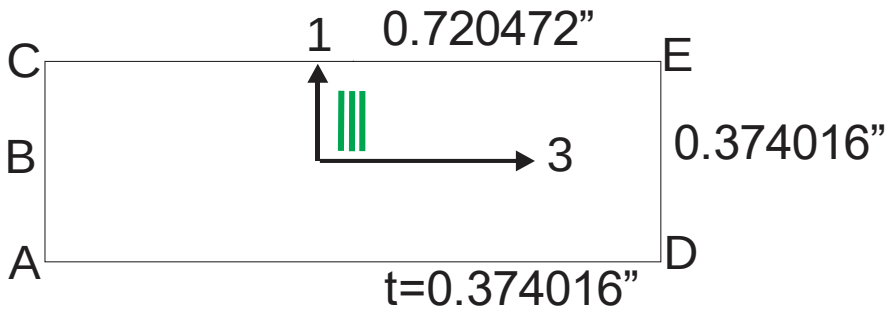

Figure 2-38. 3-direction tension schematic diagram

The FE model used for this test is shown in Figure 2-39 along with the support representations. The total number of elements in the model is 128. There are 4 elements through the thickness. There are 5 nodes through the thickness. Only the central node at the left face is pinned and the rest of the nodes on the left face have roller supports. Velocity of 0.5 in/s is applied at the nodes on the right face of the model in the positive x-direction.

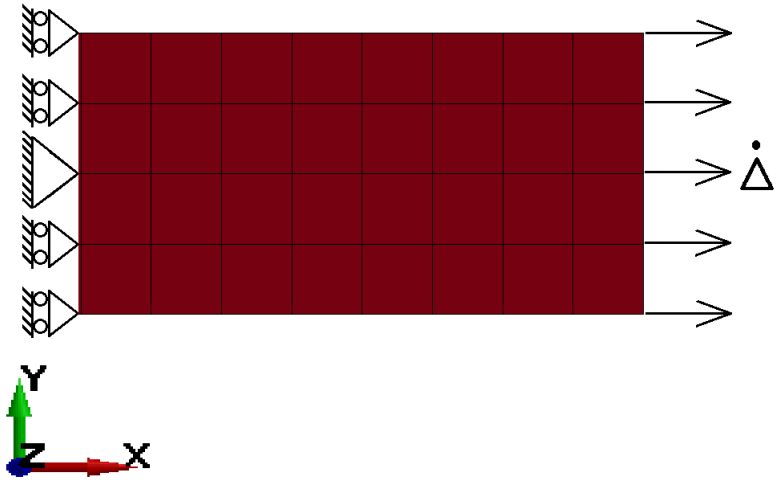

Figure 2-39. 3-direction tension FE model

The middle 8 (2 elements through the thickness) elements are considered for the post-processing. The average of the stress-strain curves of these 8 elements are taken into consideration and is shown in Figure 2-40.

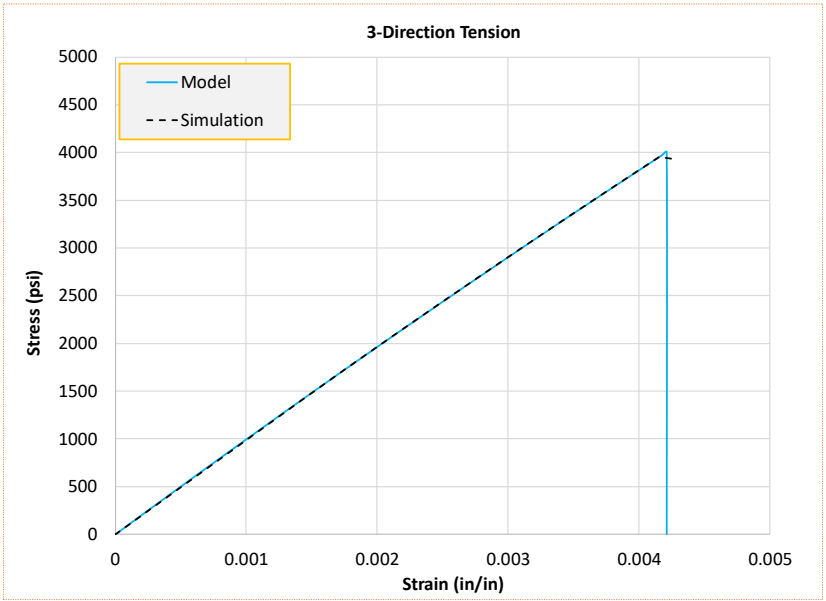

Figure 2-40. 3-direction tension stress-strain plot

The simulation stress-strain curve (Figure 2-40) remains linear until a strain value of 0.00160, and then the plasticity is observed, although the curve looks almost linear throughout.

2.3.3.6 3-Direction Compression Test

The schematic diagram of the model used for this simulation is shown in Figure 2-41. The model dimensions are also shown. The green color lines represent the orientation of the fibers.

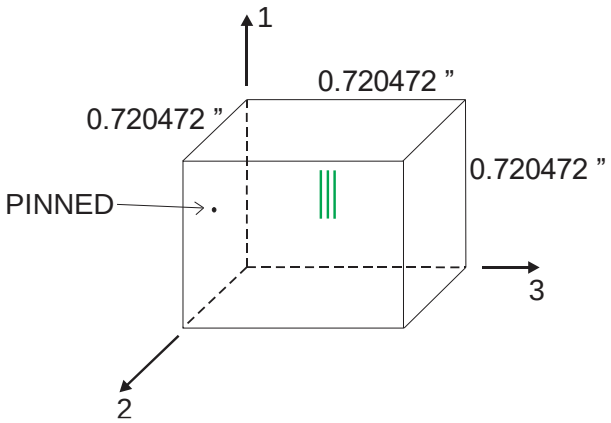

Figure 2-41. 3-Direction Compression Model Schematic Diagram

The FE model used for this test is shown in Figure 2-42 along with the support representations. The total number of elements in the model is 64. There are 4 elements through the thickness. There are 5 nodes through the thickness. Only the central node at the left face is pinned and the rest of the nodes on the left face have roller supports. Velocity of 0.5 in/s is applied at the nodes on the right face of the model in the negative x-direction.

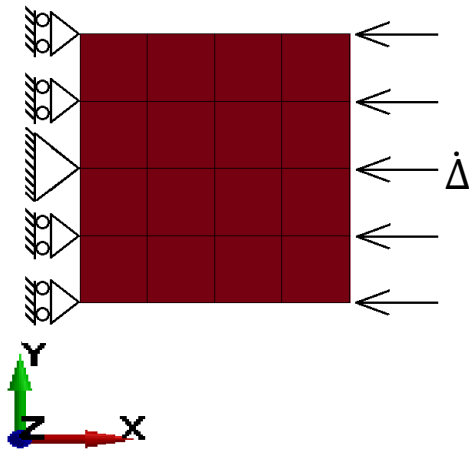

Figure 2-42. 3-Direction Compression FE model

The post-processing is done in a similar way discussed for 3-direction tension test. The stress-strain curve is shown in Figure 2-43.

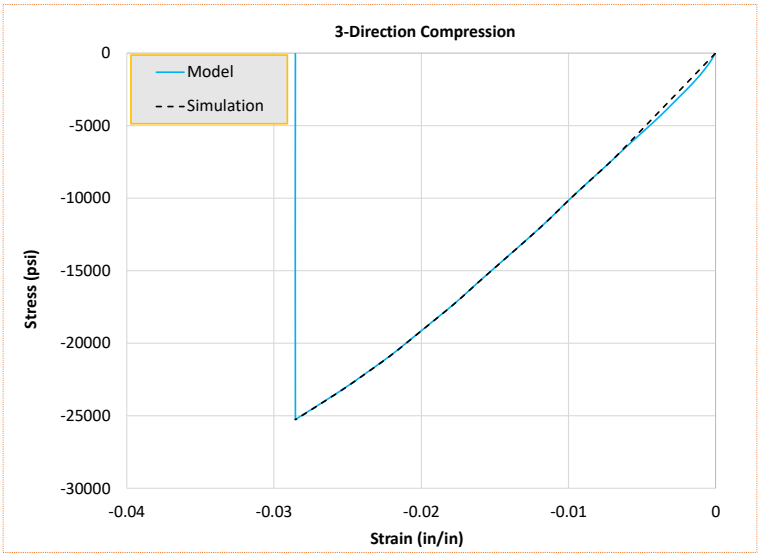

Figure 2-43. Stress-strain plot for 3-direction compression test

The simulation stress-strain curve (Figure 2-43) remains linear until the strain reaches a value of 0.00688, after which plasticity is observed.

2.3.3.7 1-2 Plane Shear

The schematic diagram of the model used for this simulation is shown in Figure 2-44. The model dimensions in inches are also shown.

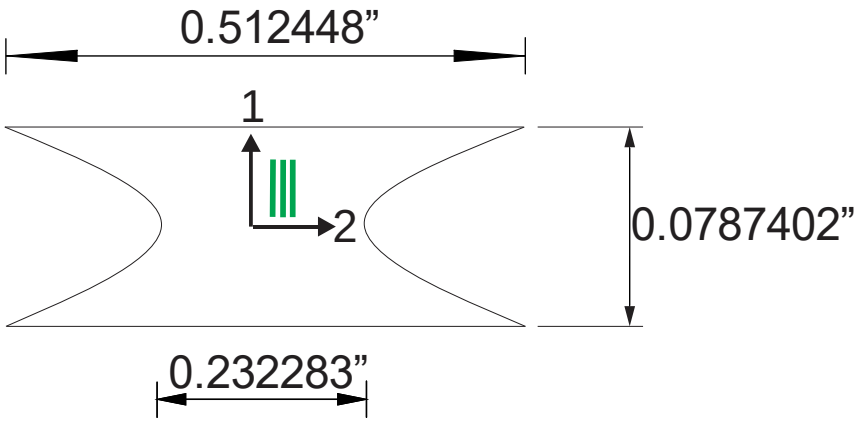

Figure 2-44. 1-2 plane shear model schematic diagram

The FE model used for this test is shown in Figure 2-45 along with the support representations. The translational displacement is free only along the direction of velocity at the roller supports. The total number of elements in the model is 80. There is 1 element through the thickness.

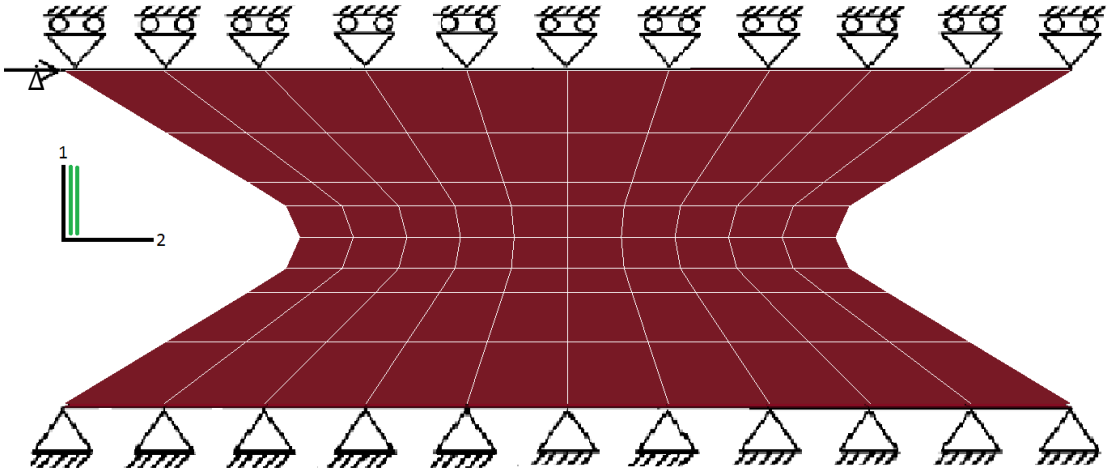

Figure 2-45. 1-2 plane shear model

The middle 4 elements are considered for the post-processing. The average of the stress-strain data of these four elements are taken into consideration. The stress-strain curves are shown in Figure 2-46.

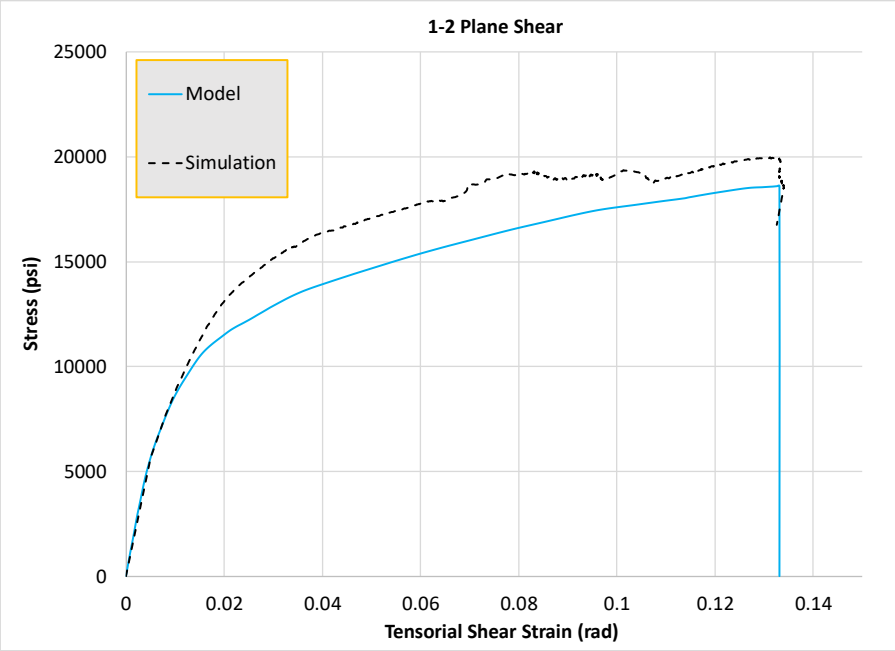

Figure 2-46. 1-2 plane shear stress-strain plot

The simulation result, which is represented by the dashed black plot, does not match with the input because the stresses are multi-axial in the model considered.

2.3.3.8 2-3 Plane Shear Test

The schematic diagram of the model used for this simulation is shown in Figure 2-47. The model dimensions are also shown. The green dots imply that the orientation of the fibers is into the plane.

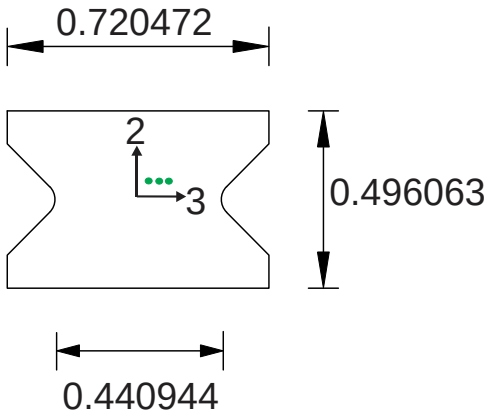

Figure 2-47. 2-3 plane shear model schematic diagram

The FE model used for this test is shown in Figure 2-48 along with the support representations. The number of elements in the model is 64. There is 1 element through the thickness. The translational displacement along x-, y-, and z-directions of the nodes

at the bottom face are restrained. For the nodes at the top face, the translational displacement along y- and z- directions are restrained. Velocity of 0.5 in/s is applied at the nodes on the top face of the model in the positive x-direction.

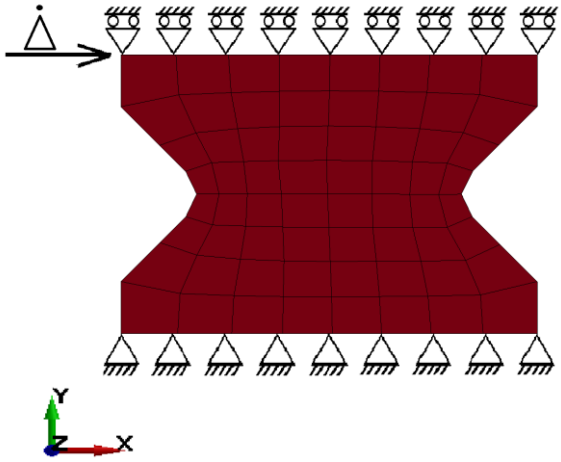

Figure 2-48. 2-3 plane shear FE model

The middle four elements are considered for the post-processing. The average of the stress-strain data of these four elements are taken into consideration. The stress-strain curve is shown in Figure 2-49.

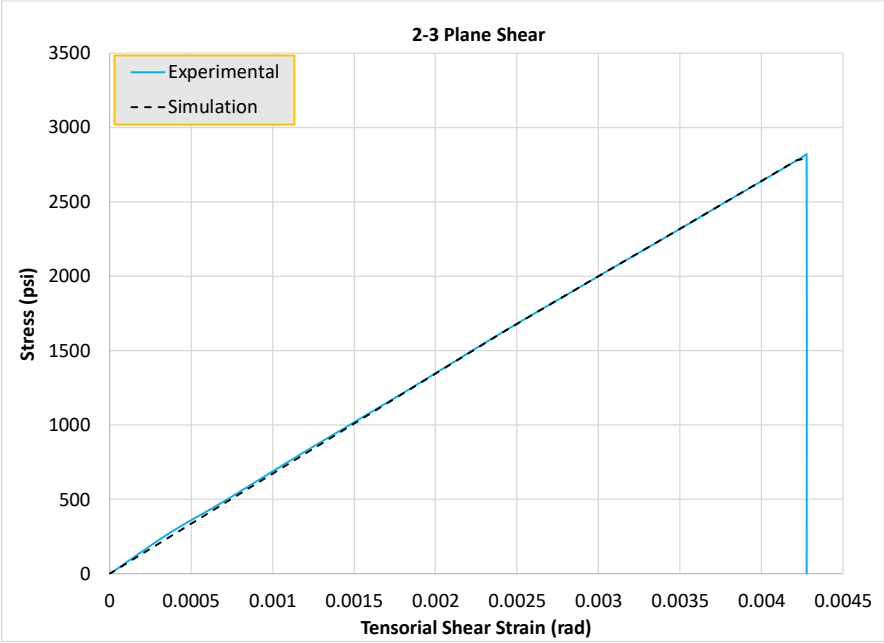

Figure 2-49. 2-3 plane shear stress-strain plot

The simulation stress-strain curve remains linear until the strain reaches a value of 0.00245, after which plasticity is observed, although the curve looks linear throughout.

2.3.3.9 1-3 Plane Shear

The schematic diagram of the model used for this simulation is shown in Figure 2-50. The model dimensions in inches are also shown.

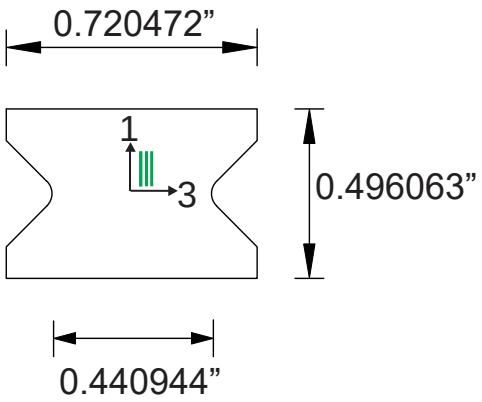

Figure 2-50. 1-3 plane shear model schematic diagram

Figure 2-51 shows the FE model used which is similar to the one discussed for 2-3 plane shear test except for the PMDs.

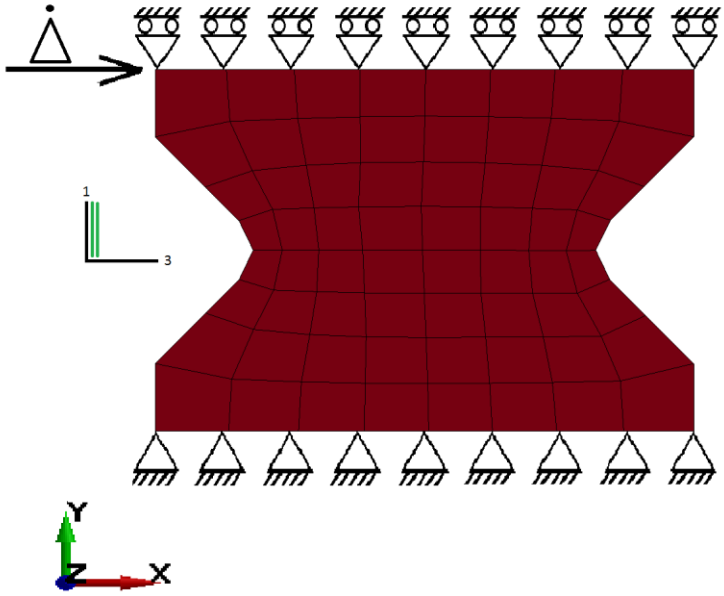

Figure 2-51. 1-3 plane shear model

The middle four elements are considered for the post-processing. The average of the stress-strain data of these four elements are taken into consideration. The stress-strain curves are shown in Figure 2-52.

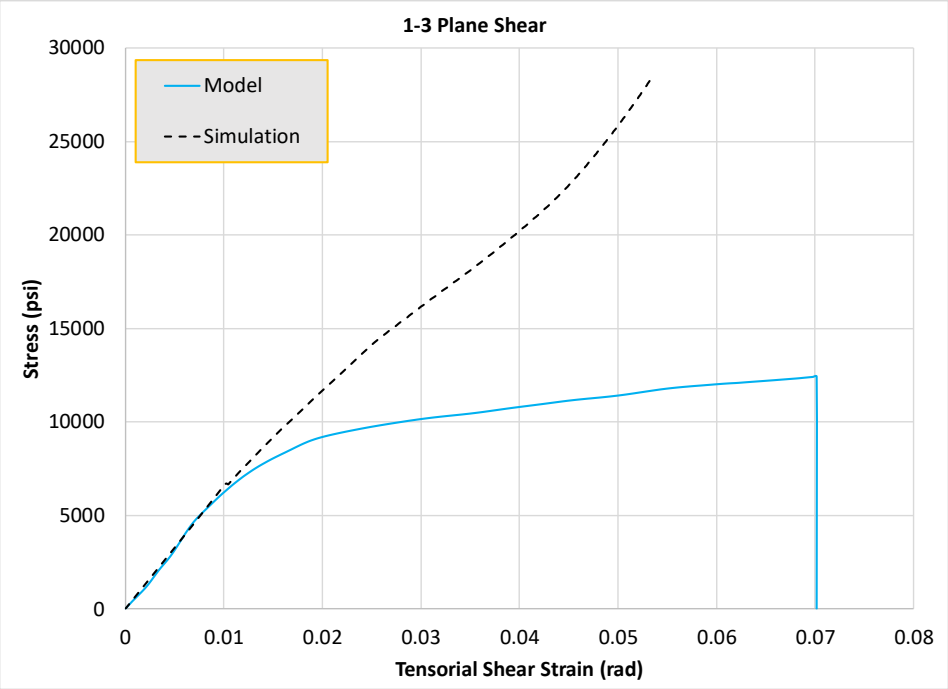

Figure 2-52. 1-3 plane shear stress-strain plot

The simulation results do not match the input because of a multi-axial state of stress in the model. The stress in 1-direction shoots up.

2.3.3.10 1-2 Plane 45° Off-Axis Tension

The schematic diagram of the model used for this simulation is shown in Figure 2-53. The model dimensions are also shown. The green color lines represent the orientation of the fibers.

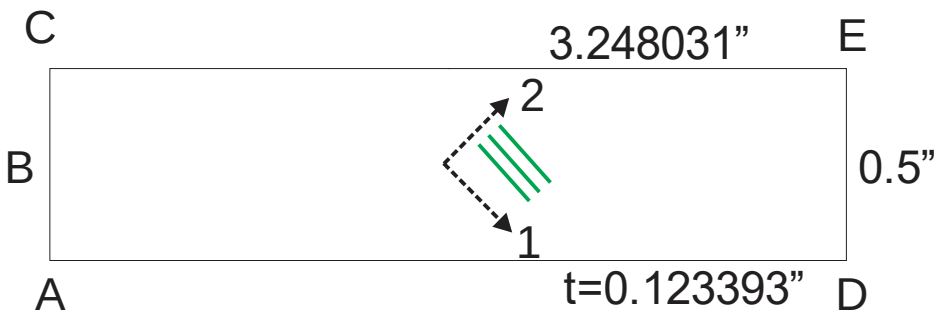

Figure 2-53. 1-2 plane 45° off-axis tension model schematic diagram

The FE model used for this test is similar to the one used for tension 1-direction except for the dimensions and the PMDs. The post-processing is done in a similar way discussed for the tension 1-direction test. The stress-strain curve is shown in Figure 2-54.

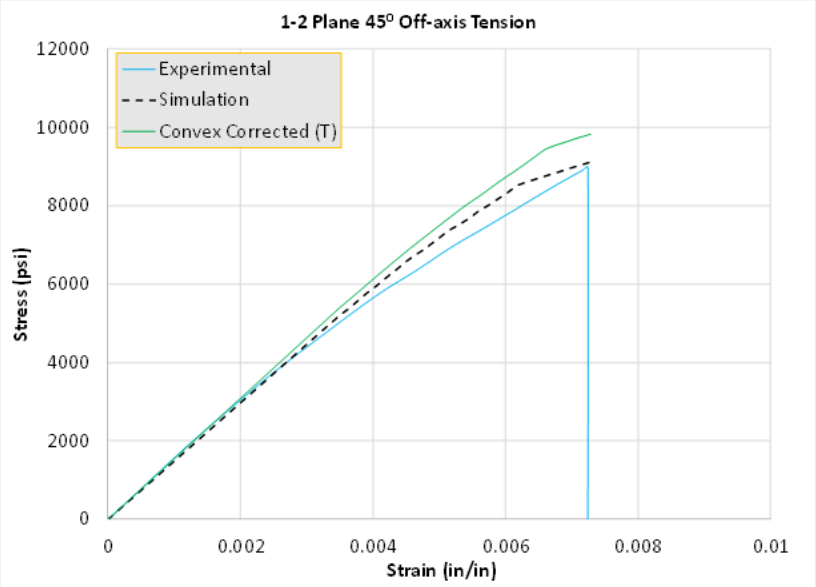

Figure 2-54. 1-2 plane 45° off-axis tension stress-strain plot

The simulation stress-strain curve (Figure 2-54) remains linear until the strain reaches a value of 0.00160, after which plasticity is observed. The simulation curve has stress values higher than the input curve (green color curve) because of the convexity correction applied.

2.3.3.11 2-3 Plane 45° Off-Axis Compression

The schematic diagram of the model used for this simulation is shown in Figure 2-55.

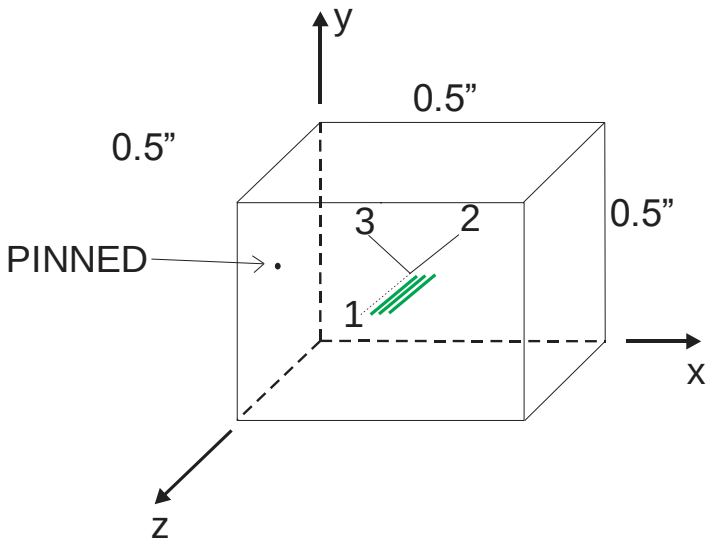

Figure 2-55. 2-3 Plane 45° Off-Axis Compression Model Schematic Diagram

The FE model used for this test is the similar to the one used for 3-direction compression test except for the dimensions and PMDs. The postprocessing is done in a similar way discussed for 3-direction compression test. The stress-strain curves are shown in Figure 2-56.

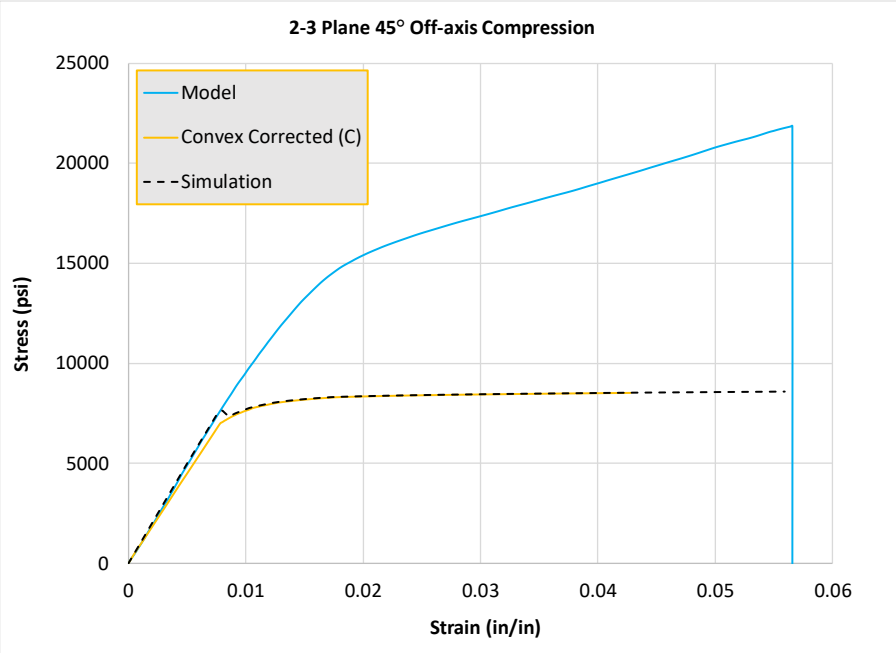

Figure 2-56. 2-3 plane 45° off-axis compression stress-strain plot

The simulation curve does not match the input curve because of convex correction.

2.3.3.12 1-3 Plane 45° Off-Axis Compression

The schematic diagram of the model used for this simulation is shown in Figure 2-57.

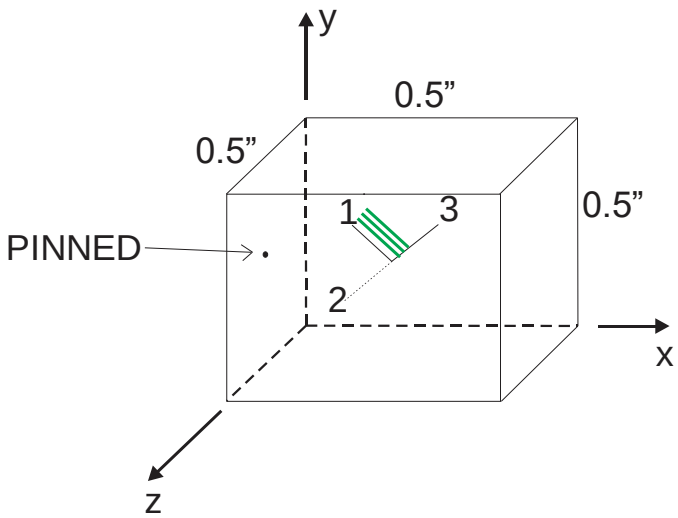

Figure 2-57. 1-3 plane 45° off-axis compression model schematic diagram

The FE model used for this test is similar to the one used for 3-direction compression test except for the dimensions and PMDs. The post-processing is done in a similar way discussed for 3-direction compression test. The stress-strain curves are shown in Figure 2-58.

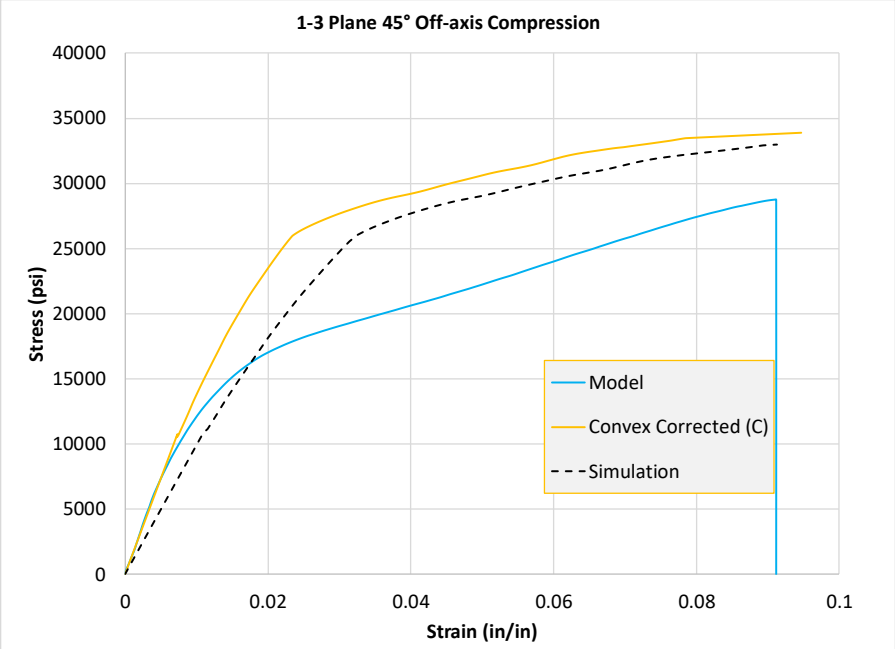

Figure 2-58. 1-3 plane 45° off-axis compression stress-strain plot

The simulation curve does not match the input curve because of convex correction.

3. DAMAGE SUB-MODEL

3.1 THEORETICAL BACKGROUND

The damage model [87] is used to relate the true stress space to the effective stress space. The true stress space is related directly to what is measured during the experiments. The effective stress space is related to the undamaged material. Essentially, the effective stress space is generated by assuming the inelastic deformations are due to both damage and plasticity. The true and effective stress spaces can be related by a damage tensor as:

$$\begin{pmatrix} \sigma_{11} \\ \sigma_{22} \\ \sigma_{33} \\ \sigma_{12} \\ \sigma_{23} \\ \sigma_{13} \end{pmatrix} = \begin{bmatrix} M_{11} & M_{12} & M_{13} & M_{14} & M_{15} & M_{16} \\ M_{21} & M_{22} & M_{23} & M_{24} & M_{25} & M_{26} \\ M_{31} & M_{32} & M_{33} & M_{34} & M_{35} & M_{36} \\ M_{41} & M_{42} & M_{43} & M_{44} & M_{45} & M_{46} \\ M_{51} & M_{52} & M_{53} & M_{54} & M_{55} & M_{56} \\ M_{61} & M_{62} & M_{63} & M_{64} & M_{65} & M_{66} \end{bmatrix} \begin{pmatrix} \sigma_{11}^{eff} \\ \sigma_{22}^{eff} \\ \sigma_{33}^{eff} \\ \sigma_{12}^{eff} \\ \sigma_{23}^{eff} \\ \sigma_{13}^{eff} \end{pmatrix} \tag{3.1}$$

where σ_{ij} is the true stress and σ_{ij}^{eff} is the effective stress. Equation 3.1 shows a full damage tensor which could lead to multiaxial stress states in the effective space that corresponds to uniaxial states in the true space. This is non-physical. Therefore, a semi-coupled, directionally dependent tensor is used in the current implementation as:

$$\begin{pmatrix} \sigma_{11} \\ \sigma_{22} \\ \sigma_{33} \\ \sigma_{12} \\ \sigma_{23} \\ \sigma_{13} \end{pmatrix} = \begin{bmatrix} M_{11} & 0 & 0 & 0 & 0 & 0 \\ 0 & M_{22} & 0 & 0 & 0 & 0 \\ 0 & 0 & M_{33} & 0 & 0 & 0 \\ 0 & 0 & 0 & M_{44} & 0 & 0 \\ 0 & 0 & 0 & 0 & M_{55} & 0 \\ 0 & 0 & 0 & 0 & 0 & M_{66} \end{bmatrix} \begin{pmatrix} \sigma_{11}^{eff} \\ \sigma_{22}^{eff} \\ \sigma_{33}^{eff} \\ \sigma_{12}^{eff} \\ \sigma_{23}^{eff} \\ \sigma_{13}^{eff} \end{pmatrix} \tag{3.2}$$

Each of the terms in the damage tensor in equation 4.2 are dependent on all the plastic strains that are induced in the material, for example:

$$M_{11} = M_{11}\left(\varepsilon_p^{11}, \varepsilon_p^{22}, \varepsilon_p^{33}, \varepsilon_p^{12}, \varepsilon_p^{23}, \varepsilon_p^{13}\right)$$

The damage parameters are tracked as a function of plastic strain since any damage incurred in the elastic regime is ignored in the current formulation. The semi-coupled nature of the damage tensor ensures that a uniaxial effective stress state does not result in a multiaxial true stress state. For full generalization, both normal and shear damage are attributed to all normal and shear terms. Additionally, no assumption is made regarding the symmetry of the material, meaning damage induced due to compression or tension loading in a given PMD is treated independently. The sign of the

stress is the metric used to differentiate between tension and compression regimes. Equation 3.3 shows the expressions used to update the damage parameters.

$$
\begin{aligned}
\sigma_{11} &= \begin{cases} if\ \sigma_{11} \geq 0 \rightarrow \left(1-d_{11_T}^{11_T}\left(\varepsilon_{11_T}^{p}\right)\right)\left(1-d_{11_C}^{11_T}\left(\varepsilon_{11_C}^{p}\right)\right)\left(1-d_{22_T}^{11_T}\left(\varepsilon_{22_T}^{p}\right)\right)\left(1-d_{22_C}^{11_T}\left(\varepsilon_{22_C}^{p}\right)\right)\left(1-d_{33_T}^{11_T}\left(\varepsilon_{33_T}^{p}\right)\right) \\ \quad \left(1-d_{33_C}^{11_T}\left(\varepsilon_{33_C}^{p}\right)\right)\left(1-d_{12}^{11_T}\left(\varepsilon_{12}^{p}\right)\right)\left(1-d_{23}^{11_T}\left(\varepsilon_{23}^{p}\right)\right)\left(1-d_{13}^{11_T}\left(\varepsilon_{13}^{p}\right)\right)\sigma_{11}^{eff} \\ if\ \sigma_{11} < 0 \rightarrow \left(1-d_{11_T}^{11_C}\left(\varepsilon_{11_T}^{p}\right)\right)\left(1-d_{11_C}^{11_C}\left(\varepsilon_{11_C}^{p}\right)\right)\left(1-d_{22_T}^{11_C}\left(\varepsilon_{22_T}^{p}\right)\right)\left(1-d_{22_C}^{11_C}\left(\varepsilon_{22_C}^{p}\right)\right)\left(1-d_{33_T}^{11_C}\left(\varepsilon_{33_T}^{p}\right)\right) \\ \quad \left(1-d_{33_C}^{11_C}\left(\varepsilon_{33_C}^{p}\right)\right)\left(1-d_{12}^{11_C}\left(\varepsilon_{12}^{p}\right)\right)\left(1-d_{23}^{11_C}\left(\varepsilon_{23}^{p}\right)\right)\left(1-d_{13}^{11_C}\left(\varepsilon_{13}^{p}\right)\right)\sigma_{11}^{eff} \end{cases} \\
\sigma_{22} &= \begin{cases} if\ \sigma_{22} \geq 0 \rightarrow \left(1-d_{11_T}^{22_T}\left(\varepsilon_{11_T}^{p}\right)\right)\left(1-d_{11_C}^{22_T}\left(\varepsilon_{11_C}^{p}\right)\right)\left(1-d_{22_T}^{22_T}\left(\varepsilon_{22_T}^{p}\right)\right)\left(1-d_{22_C}^{22_T}\left(\varepsilon_{22_C}^{p}\right)\right)\left(1-d_{33_T}^{22_T}\left(\varepsilon_{33_T}^{p}\right)\right) \\ \quad \left(1-d_{33_C}^{22_T}\left(\varepsilon_{33_C}^{p}\right)\right)\left(1-d_{12}^{22_T}\left(\varepsilon_{12}^{p}\right)\right)\left(1-d_{23}^{22_T}\left(\varepsilon_{23}^{p}\right)\right)\left(1-d_{13}^{22_T}\left(\varepsilon_{13}^{p}\right)\right)\sigma_{22}^{eff} \\ if\ \sigma_{22} < 0 \rightarrow \left(1-d_{11_T}^{22_C}\left(\varepsilon_{11_T}^{p}\right)\right)\left(1-d_{11_C}^{22_C}\left(\varepsilon_{11_C}^{p}\right)\right)\left(1-d_{22_T}^{22_C}\left(\varepsilon_{22_T}^{p}\right)\right)\left(1-d_{22_C}^{22_C}\left(\varepsilon_{22_C}^{p}\right)\right)\left(1-d_{33_T}^{22_C}\left(\varepsilon_{33_T}^{p}\right)\right) \\ \quad \left(1-d_{33_C}^{22_C}\left(\varepsilon_{33_C}^{p}\right)\right)\left(1-d_{12}^{22_C}\left(\varepsilon_{12}^{p}\right)\right)\left(1-d_{23}^{22_C}\left(\varepsilon_{23}^{p}\right)\right)\left(1-d_{13}^{22_C}\left(\varepsilon_{13}^{p}\right)\right)\sigma_{22}^{eff} \end{cases} \\
\sigma_{33} &= \begin{cases} if\ \sigma_{33} \geq 0 \rightarrow \left(1-d_{11_T}^{33_T}\left(\varepsilon_{11_T}^{p}\right)\right)\left(1-d_{11_C}^{33_T}\left(\varepsilon_{11_C}^{p}\right)\right)\left(1-d_{22_T}^{33_T}\left(\varepsilon_{22_T}^{p}\right)\right)\left(1-d_{22_C}^{33_T}\left(\varepsilon_{22_C}^{p}\right)\right)\left(1-d_{33_T}^{33_T}\left(\varepsilon_{33_T}^{p}\right)\right) \\ \quad \left(1-d_{33_C}^{33_T}\left(\varepsilon_{33_C}^{p}\right)\right)\left(1-d_{12}^{33_T}\left(\varepsilon_{12}^{p}\right)\right)\left(1-d_{23}^{33_T}\left(\varepsilon_{23}^{p}\right)\right)\left(1-d_{13}^{33_T}\left(\varepsilon_{13}^{p}\right)\right)\sigma_{33}^{eff} \\ if\ \sigma_{33} < 0 \rightarrow \left(1-d_{11_T}^{33_C}\left(\varepsilon_{11_T}^{p}\right)\right)\left(1-d_{11_C}^{33_C}\left(\varepsilon_{11_C}^{p}\right)\right)\left(1-d_{22_T}^{33_C}\left(\varepsilon_{22_T}^{p}\right)\right)\left(1-d_{22_C}^{33_C}\left(\varepsilon_{22_C}^{p}\right)\right)\left(1-d_{33_T}^{33_C}\left(\varepsilon_{33_T}^{p}\right)\right) \\ \quad \left(1-d_{33_C}^{33_C}\left(\varepsilon_{33_C}^{p}\right)\right)\left(1-d_{12}^{33_C}\left(\varepsilon_{12}^{p}\right)\right)\left(1-d_{23}^{33_C}\left(\varepsilon_{23}^{p}\right)\right)\left(1-d_{13}^{33_C}\left(\varepsilon_{13}^{p}\right)\right)\sigma_{33}^{eff} \end{cases} \\
\sigma_{12} &= \left(1-d_{11_T}^{12}\left(\varepsilon_{11_T}^{p}\right)\right)\left(1-d_{11_C}^{12}\left(\varepsilon_{11_C}^{p}\right)\right)\left(1-d_{22_T}^{12}\left(\varepsilon_{22_T}^{p}\right)\right)\left(1-d_{22_C}^{12}\left(\varepsilon_{22_C}^{p}\right)\right)\left(1-d_{33_T}^{12}\left(\varepsilon_{33_T}^{p}\right)\right) \\ &\quad \left(1-d_{33_C}^{12}\left(\varepsilon_{33_C}^{p}\right)\right)\left(1-d_{12}^{12}\left(\varepsilon_{12}^{p}\right)\right)\left(1-d_{23}^{12}\left(\varepsilon_{23}^{p}\right)\right)\left(1-d_{13}^{12}\left(\varepsilon_{13}^{p}\right)\right)\sigma_{12}^{eff} \\
\sigma_{23} &= \left(1-d_{11_T}^{23}\left(\varepsilon_{11_T}^{p}\right)\right)\left(1-d_{11_C}^{23}\left(\varepsilon_{11_C}^{p}\right)\right)\left(1-d_{22_T}^{23}\left(\varepsilon_{22_T}^{p}\right)\right)\left(1-d_{22_C}^{23}\left(\varepsilon_{22_C}^{p}\right)\right)\left(1-d_{33_T}^{23}\left(\varepsilon_{33_T}^{p}\right)\right) \\ &\quad \left(1-d_{33_C}^{23}\left(\varepsilon_{33_C}^{p}\right)\right)\left(1-d_{12}^{23}\left(\varepsilon_{12}^{p}\right)\right)\left(1-d_{23}^{23}\left(\varepsilon_{23}^{p}\right)\right)\left(1-d_{13}^{23}\left(\varepsilon_{13}^{p}\right)\right)\sigma_{23}^{eff} \\
\sigma_{13} &= \left(1-d_{11_T}^{13}\left(\varepsilon_{11_T}^{p}\right)\right)\left(1-d_{11_C}^{13}\left(\varepsilon_{11_C}^{p}\right)\right)\left(1-d_{22_T}^{13}\left(\varepsilon_{22_T}^{p}\right)\right)\left(1-d_{22_C}^{13}\left(\varepsilon_{22_C}^{p}\right)\right)\left(1-d_{33_T}^{13}\left(\varepsilon_{33_T}^{p}\right)\right) \\ &\quad \left(1-d_{33_C}^{13}\left(\varepsilon_{33_C}^{p}\right)\right)\left(1-d_{12}^{13}\left(\varepsilon_{12}^{p}\right)\right)\left(1-d_{23}^{13}\left(\varepsilon_{23}^{p}\right)\right)\left(1-d_{13}^{13}\left(\varepsilon_{13}^{p}\right)\right)\sigma_{13}^{eff}
\end{aligned}
\qquad 3.3
$$

Equation 3.3 shows 81 parameters that are used to describe the damaged state of the material. There are three additional parameters corresponding to uncoupled off-axis tests, $d_{12_{45^\circ}}^{12_{45^\circ}}$, $d_{23_{45^\circ}}^{23_{45^\circ}}$, and $d_{13_{45^\circ}}^{13_{45^\circ}}$, that are used to ensure convexity of the yield surface, for a total of 84 possible parameters. While the number of damage parameters appears to be large, we do not expect more than a handful of these parameters to be significant for a given composite. The effective stress rate is given by

$$\dot{\boldsymbol{\sigma}}^{eff} = \mathbf{C}\left(\dot{\boldsymbol{\varepsilon}} - \dot{\boldsymbol{\varepsilon}}_p\right) \qquad 3.4$$

Where $\mathbf{C}$ is the standard orthotropic elastic stiffness tensor and, by linearly decomposing the total strain rate tensor, the elastic strain rate is written as a function of the total strain rate, $\dot{\boldsymbol{\varepsilon}}$, and the plastic strain rate, $\dot{\boldsymbol{\varepsilon}}_p$. The expression for the effective stress assumes a strain equivalence between the true and effective stress space, thus allowing for all the plasticity computations to be performed in the effective stress space, essentially decoupling the plasticity and damage algorithms. The strain equivalence

assumption essentially assumes that all permanent strain in the material is caused by plastic deformation and the damage only effects the unloading path. Figure 3-1 shows the consequence of making a strain equivalence assumption.

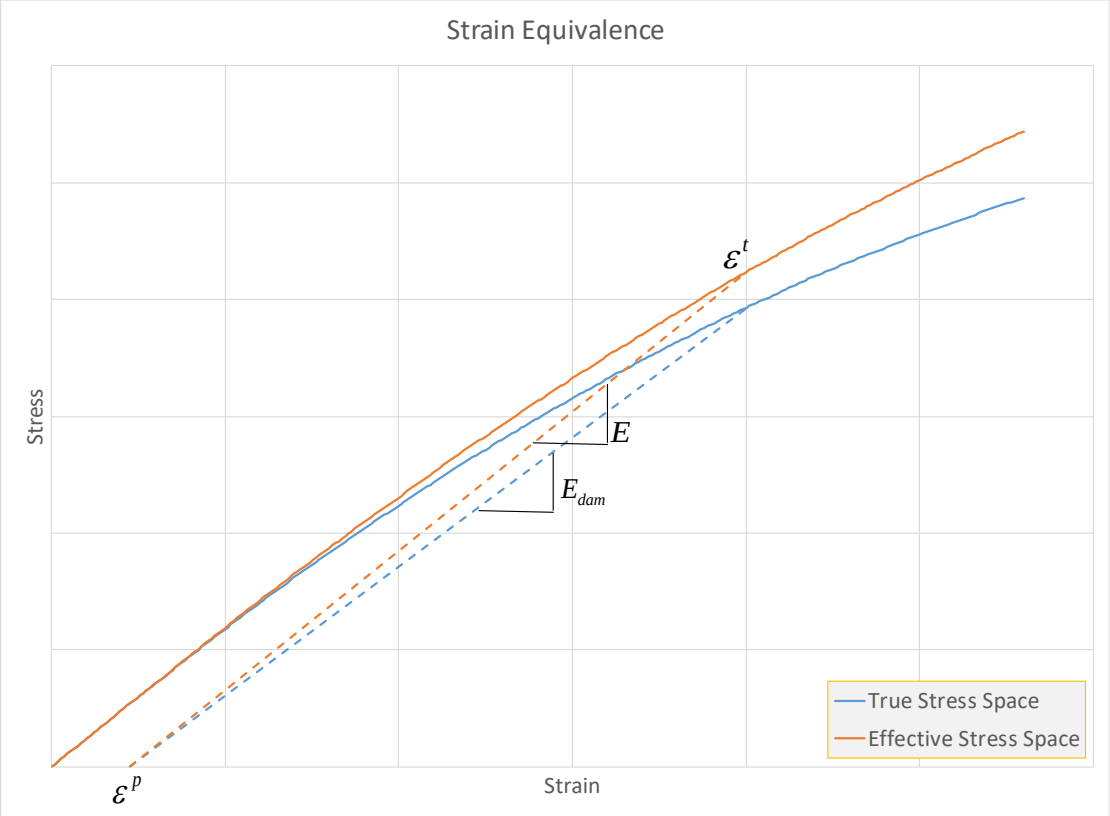

Figure 3-1. Consequence of strain equivalence assumption

3.2 IMPLEMENTATION DETAILS

The damage theory is incorporated into the pre-processing stage and the plasticity computations in MAT213. The following sections detail the approach used.

3.2.1 Pre-processing

Input curves are given as stress-total strain but need to be converted into effective-stress-effective-plastic strain. The total process is as follows: convert input curves from stress-total strain to effective-stress-total strain to effective-stress-plastic strain to effective-stress-effective plastic strain.

$$\sigma - \varepsilon_t \rightarrow \sigma^{eff} - \varepsilon_t \rightarrow \sigma^{eff} - \varepsilon_p \rightarrow \sigma^{eff} - \varepsilon_p^e \qquad 3.5$$

The first step, $\sigma - \varepsilon_t \rightarrow \sigma^{eff} - \varepsilon_t$, uses the damage parameters given as input. Only the corresponding uncoupled damage term is used to initially convert the curves into the effective stress space.

$$\sigma_{22_C}^{eff} = \frac{\sigma_{22_C}}{1 - d_{22_C}^{22_C}} \tag{3.6}$$

The second step, $\tilde{\sigma} - \varepsilon_t \rightarrow \tilde{\sigma} - \varepsilon_p$, uses the strain equivalence assumption to compute plastic strain as a function of total strain. This step uses effective stress and the undamaged modulus.

$$\varepsilon_{22_C}^{p} = \varepsilon_{22_C}^{t} - \frac{\sigma_{22_C}^{eff}}{E_{22_C}} \tag{3.7}$$

The final step, $\tilde{\sigma} - \varepsilon_p \rightarrow \tilde{\sigma} - \varepsilon_p^e$, is done in the same manner as previously documented, using plastic work equivalence. The effective stress is used to perform this conversion as well.

$$\varepsilon_p^e = \int \frac{\sigma_{22_C}^{eff} \, d\varepsilon_{22_C}^{P}}{\sqrt{H_{22}\left(\sigma_{22_C}^{eff}\right)^2}} \tag{3.8}$$

The resulting $\tilde{\sigma} - \varepsilon_p^e$ curves are used to track the yield stresses during the simulation.

3.2.2 Incorporation into Plasticity Algorithm

All plasticity computations are currently performed in the effective stress space. Denoting subscripts *t* as the previous instance of time and *t+1* as the current instance of time (that which is being solved for), the incremental algorithm is as follows. Additionally, $\boldsymbol{\sigma}$ refers to stresses in the true stress space while $\boldsymbol{\sigma}^{eff}$ refers to stresses in the effective stress space.

1. Obtain damage parameters as a function of the plastic strain at the end of the previous time step. This is done to obtain the trial state.

$$d_{t+1} = d\left(\varepsilon_t^p\right) \tag{3.9}$$

2. Stresses from the end of the previous time step are converted from the true stress space to the effective stress space as a function of the corresponding coupled and uncoupled terms. For a given PMD, the sign of the stress in the PMD at the end of the previous time step dictates whether the tension or compression damage terms are used.

$$if\ \sigma_t^{22} \geq 0 \rightarrow \left(\sigma_t^{22}\right)^{eff} = \sigma_t^{22} \Bigg/ \begin{bmatrix} \left(1-d_{11_T}^{22_T}\left(\left(\varepsilon_{11_T}^{p}\right)_t\right)\right)\left(1-d_{11_C}^{22_T}\left(\left(\varepsilon_{11_C}^{p}\right)_t\right)\right)\left(1-d_{22_T}^{22_T}\left(\left(\varepsilon_{22_T}^{p}\right)_t\right)\right)\left(1-d_{22_C}^{22_T}\left(\left(\varepsilon_{22_C}^{p}\right)_t\right)\right) \\ \left(1-d_{33_T}^{22_T}\left(\left(\varepsilon_{33_T}^{p}\right)_t\right)\right)\left(1-d_{33_C}^{22_T}\left(\left(\varepsilon_{33_C}^{p}\right)_t\right)\right)\left(1-d_{12}^{22_T}\left(\left(\varepsilon_{12}^{p}\right)_t\right)\right)\left(1-d_{23}^{22_T}\left(\left(\varepsilon_{23}^{p}\right)_t\right)\right) \\ \left(1-d_{13}^{22_T}\left(\left(\varepsilon_{13}^{p}\right)_t\right)\right) \end{bmatrix} \tag{3.10}$$

$$if\ \sigma_t^{22} < 0 \rightarrow \left(\sigma_t^{22}\right)^{eff} = \sigma_t^{22} \Bigg/ \begin{bmatrix} \left(1-d_{11_T}^{22_C}\left(\left(\varepsilon_{11_T}^{p}\right)_t\right)\right)\left(1-d_{11_C}^{22_C}\left(\left(\varepsilon_{11_C}^{p}\right)_t\right)\right)\left(1-d_{22_T}^{22_C}\left(\left(\varepsilon_{22_T}^{p}\right)_t\right)\right)\left(1-d_{22_C}^{22_C}\left(\left(\varepsilon_{22_C}^{p}\right)_t\right)\right) \\ \left(1-d_{33_T}^{22_C}\left(\left(\varepsilon_{33_T}^{p}\right)_t\right)\right)\left(1-d_{33_C}^{22_C}\left(\left(\varepsilon_{33_C}^{p}\right)_t\right)\right)\left(1-d_{12}^{22_C}\left(\left(\varepsilon_{12}^{p}\right)_t\right)\right)\left(1-d_{23}^{22_C}\left(\left(\varepsilon_{23}^{p}\right)_t\right)\right) \\ \left(1-d_{13}^{22_C}\left(\left(\varepsilon_{13}^{p}\right)_t\right)\right) \end{bmatrix}$$

where $\boldsymbol{\sigma}_t^{eff}$ is from the end of the previous time step and is in the effective stress space. The full damage tensor, equation 4.2, is referred to as $\mathbf{M}_t$ or $\mathbf{M}_{t+1}$ allowing for the computation to be stated generally as:

$$\boldsymbol{\sigma}_t^{eff} = \mathbf{M}_t^{-1}\boldsymbol{\sigma}_t \tag{3.11}$$

The trial stress is computed using the total strain rate, given by LS-DYNA, and the undamaged stiffness matrix.

$$\left(\boldsymbol{\sigma}_{t+1}^{trial}\right)^{eff} = \boldsymbol{\sigma}_t^{eff} + \mathbf{C} : \dot{\boldsymbol{\varepsilon}}_{t+1}^{total}\Delta t \tag{3.12}$$

After converging to a value of the plastic multiplier increment, $\Delta\lambda_{t+1}$, the final stress state is computed using the flow rule and by using a linear decomposition of the total strain into elastic and plastic components:

$$\boldsymbol{\sigma}_{t+1}^{eff} = \left(\boldsymbol{\sigma}_{t+1}^{trial}\right)^{eff} - \Delta\lambda_{t+1}\mathbf{C} : \frac{\partial g}{\partial\left(\boldsymbol{\sigma}_{t+1}^{trial}\right)^{eff}} \tag{3.13}$$

The plastic strains are then updated using the value of $\Delta\lambda_{t+1}$ and the flow rule:

$$\boldsymbol{\varepsilon}_{t+1}^{p} = \boldsymbol{\varepsilon}_t^{p} + \Delta\lambda_{t+1} abs\left(\frac{\partial g}{\partial\left(\boldsymbol{\sigma}_{t+1}^{trial}\right)^{eff}}\right) \tag{3.14}$$

The tension and compression plastic strains in the PMDs are individually incremented and stored in order to track the damage, based on the sign of $\tilde{\boldsymbol{\sigma}}_{t+1}$. For example, in the case of the 2-direction:

$$
if \begin{cases}
\left(\sigma_{t+1}^{22}\right)^{eff} \geq 0 \rightarrow \left(\varepsilon_{t+1}^{p}\right)^{22_C} = \left(\varepsilon_{t}^{p}\right)^{22_C} \\
\qquad \left(\varepsilon_{t+1}^{p}\right)^{22_T} = \left(\varepsilon_{t}^{p}\right)^{22_T} + \Delta\lambda_{t+1} abs\left(\dfrac{\partial g}{\partial\left(\sigma_{t+1}^{trial}\right)_{22}^{eff}}\right) \\
\left(\sigma_{t+1}^{22}\right)^{eff} < 0 \rightarrow \left(\varepsilon_{t+1}^{p}\right)^{22_T} = \left(\varepsilon_{t}^{p}\right)^{22_T} \\
\qquad \left(\varepsilon_{t+1}^{p}\right)^{22_C} = \left(\varepsilon_{t}^{p}\right)^{22_C} + \Delta\lambda_{t+1} abs\left(\dfrac{\partial g}{\partial\left(\sigma_{t+1}^{trial}\right)_{22}^{eff}}\right)
\end{cases}
\tag{3.15}
$$

The damage parameters are then updated based on the value of $\boldsymbol{\varepsilon}_{t+1}^{p}$.

$$
\mathbf{M}_{t+1} = \mathbf{M}_{t+1}\left(\boldsymbol{\varepsilon}_{t+1}^{p}\right) \tag{3.16}
$$

Finally, the stresses are converted from the effective stress space into the true stress space and passed back to LS-DYNA.

$$
\boldsymbol{\sigma}_{t+1} = \mathbf{M}_{t+1}\boldsymbol{\sigma}_{t+1}^{eff} \tag{3.17}
$$

3.3 MODEL VERIFICATION

Single element verification tests were performed to ensure the theory was implemented correctly into MAT213. The simulations include both monotonic and cyclic loading. The monotonic loading tests are used to illustrate that, even with the inclusion of damage, the nonlinear response remains unaffected. The cyclic loading tests illustrate that during unloading the stiffness reduction takes place according to the input curves. Examples of both an uncoupled and a coupled simulation are presented for the monotonic and cyclic loading test cases. Figure 3-2 shows a schematic of the unit volume cube finite element model used for both verification tests.

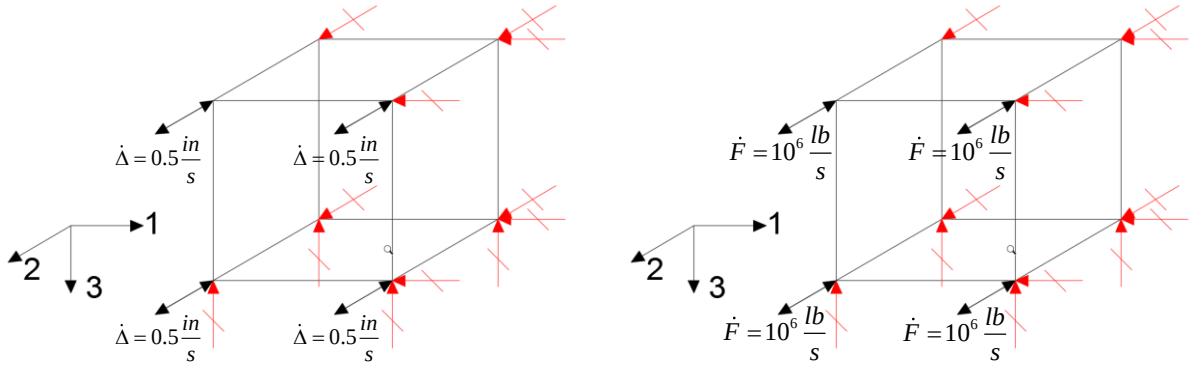

(a) (b)

Figure 3-2. SE verification test finite element model schematic with boundary conditions (a) displacement-controlled simulations and (b) load-controlled simulations. (Arrows which have been crossed out represent restrained degrees of freedom)

3.3.1 Uncoupled 2-direction Compression

The uncoupled 2-direction compression verification simulation uses the damage data presented in Khaled et al. [33]. The simulations were performed under displacement control. The results of the verification tests for both the monotonic and cyclic loading cases as well as with deformation and damage (Def+Dam) and without damage (Def) included in the input are shown in
Figure 3-3.

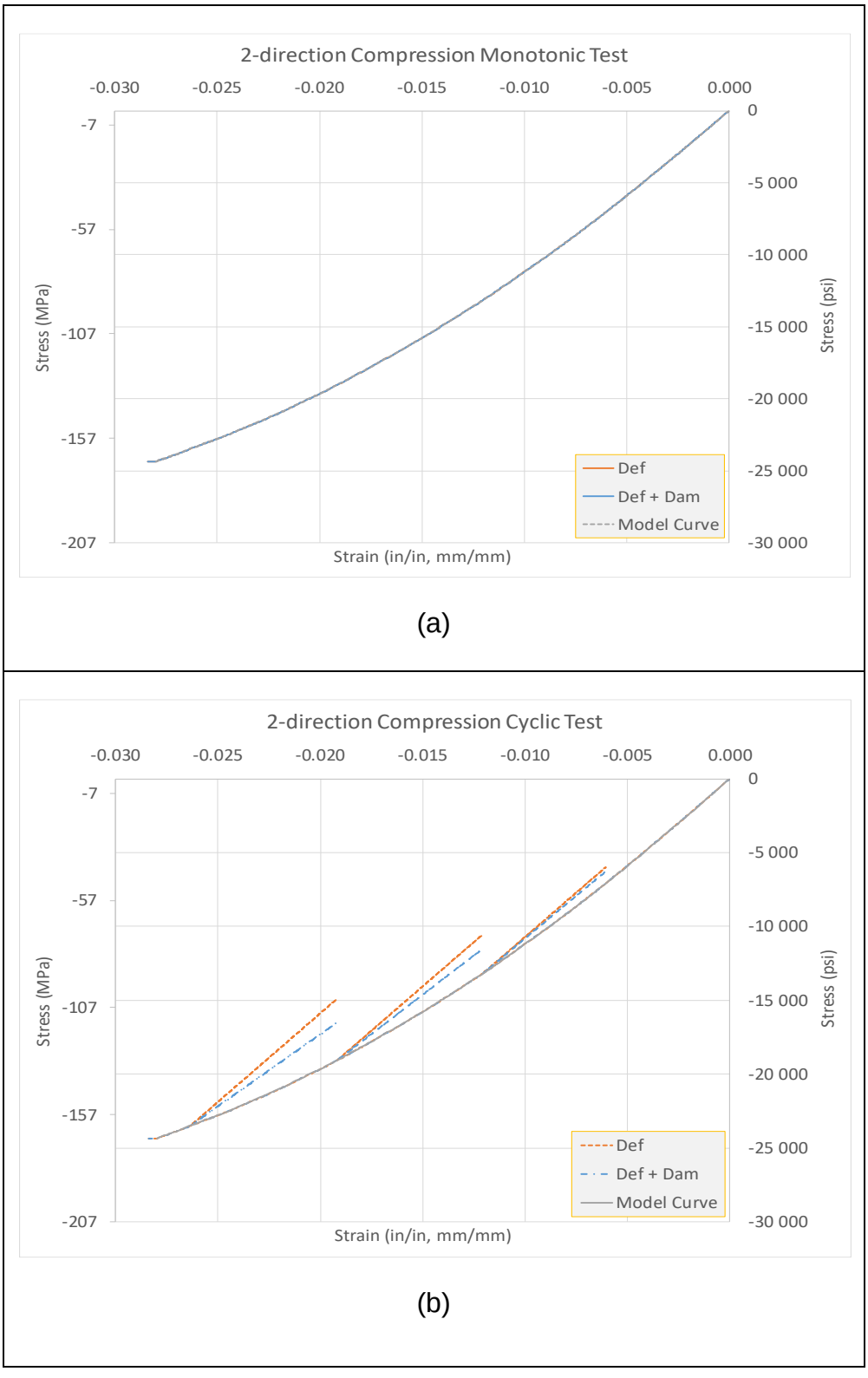

Figure 3-3. Uncoupled damage SE verification test results (a) monotonic loading and (b) cyclic loading

Figure 3-3(b) shows that the cyclic loading curves are enveloped by the corresponding input 2-direction compression stress-strain curve that is consistent with the theory as well as the experimental results presented in the previous section. The cyclic loading curve, with damage included in the model, exhibits a more compliant elastic unloading path consistent with the input damage parameter-total strain curve.

3.3.2 Coupled 2-direction Compression 2-direction Tension

The coupled 2-direction compression 2-direction tension verification test uses the damage data presented in Khaled et al. [33] (i.e., only using $d_{22_C}^{22_T}$). The simulations were performed under load control in order to avoid accidently entering the plastic regime when the stress reversal occurs. Damage is induced by loading the model in compression and interrogating the elastic tension regime. The unload path in the compression regime (i.e., negative stress) follows the undamaged modulus while the elastic regime in the tension regime (i.e., positive stress) follows the damaged modulus. The results of the SE verification test for both the monotonic and cyclic loading cases as well as with deformation and damage (Def+Dam) and without damage (Def) included in the input are shown in Figure 3-4.

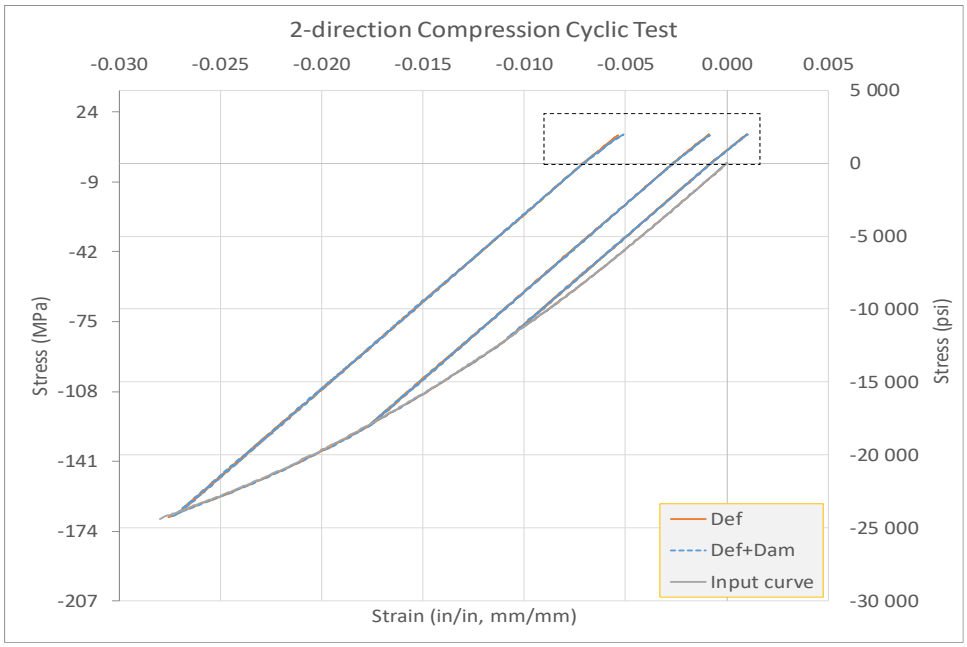

(a)

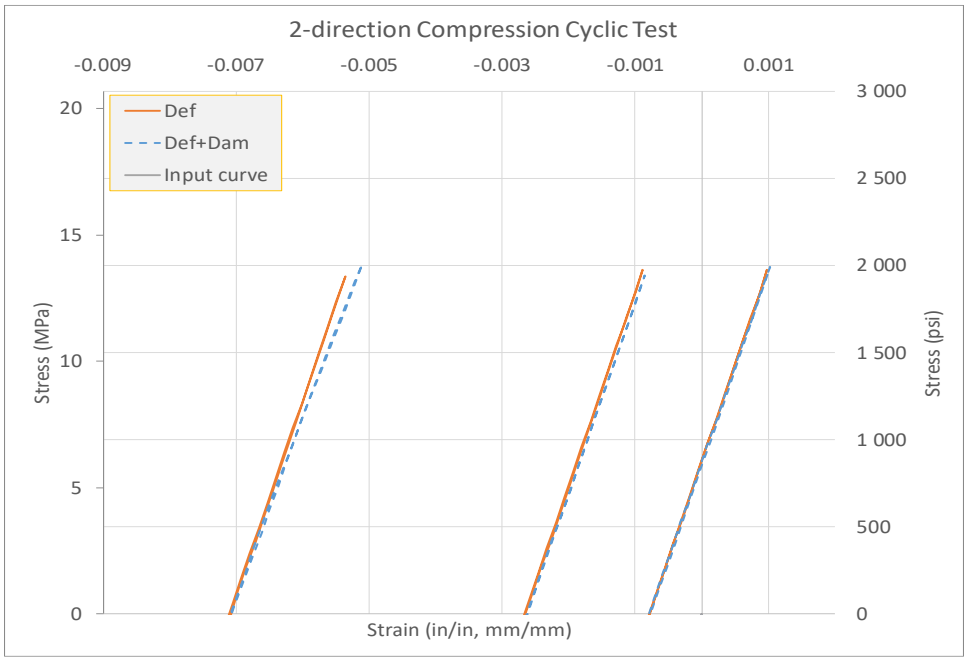

(b)

Figure 3-4. Coupled damage SE verification test results (a) full stress-strain response and (b) close up tension regime

Figure 3-4 shows a clear reduction in the elastic tension stiffness as the plastic strain in compression increases. The difference in the elastic stiffness is small but consistent with the input data shown in Khaled et al. [33]. A second verification test was performed under displacement control to illustrate how coupled damage affects the yield surface. While the compression yield stress remains unchanged between the two simulations, the tension yield stress is expected to show softening when the coupled damage term is included. Figure 3-5 shows the results of the verification tests.

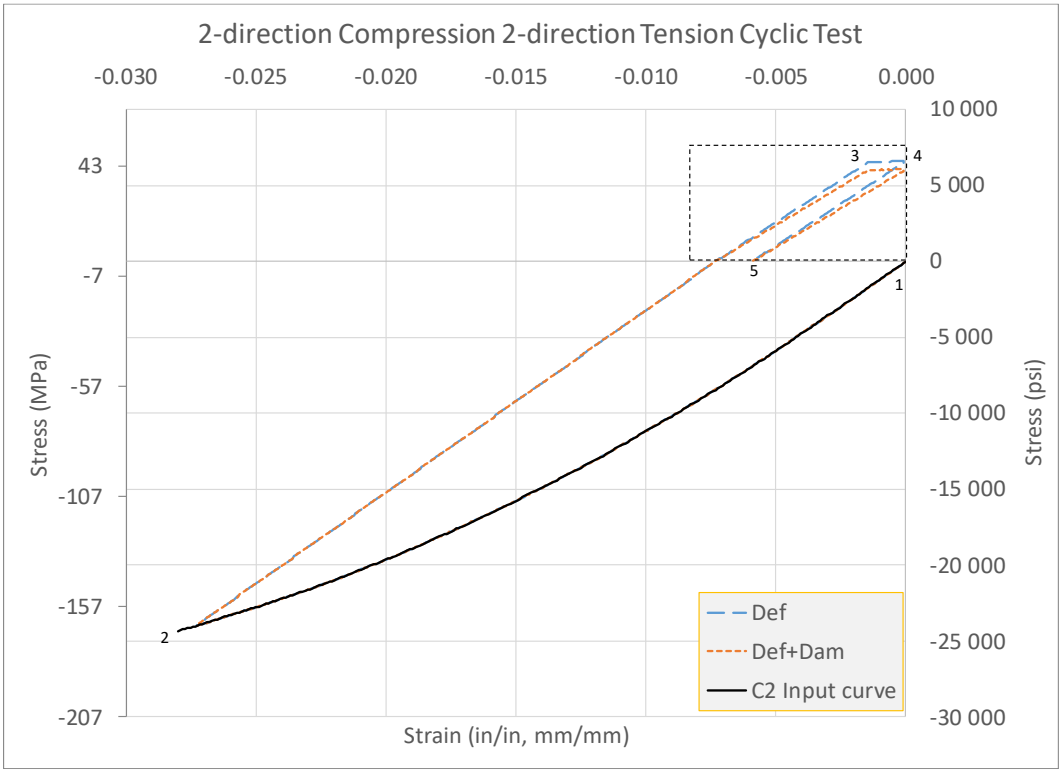

Figure 3-5. Stress strain responses of the simulations. Loading goes in the following order 1 → 2 → 3 → 4 → 5

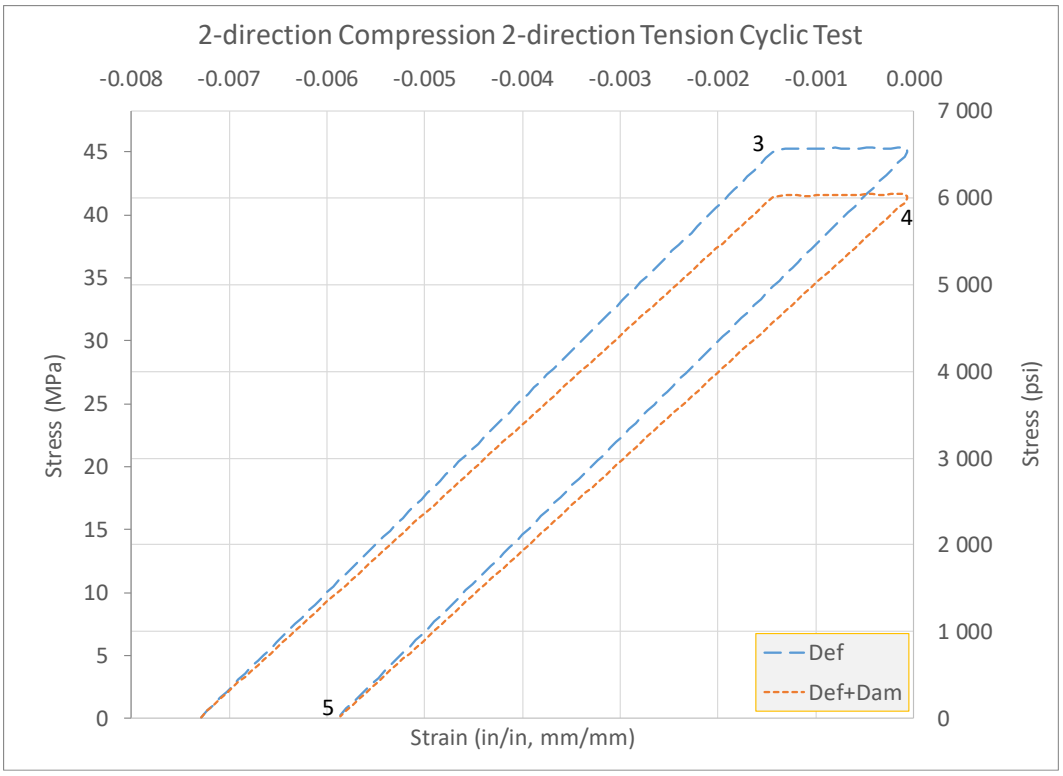

Figure 3-6. Close-up of tension regime of the full stress-strain curve shown in Figure 3-5

The results shown in Figure 3-5 and Figure 3-6 indicate that there is inherent softening of the material when coupled damage is included. The percent reduction in the yield value is equivalent to the percent reduction in the stiffness. This is to be expected since the 2-direction tension input curve does not account for coupled damage during the preprocessing step where the curves are converted from true stress to effective stress space. Only uncoupled damage terms are used in the initial conversion since, during the actual monotonic loading experiment, only uncoupled damage is being induced in the specimen. Thus, the 2-direction tension yield surfaces for the deformation only simulation (Def) and the deformation and coupled damage simulation (Def+Dam) are the same. However, during the unloading from point 4 to 5 in Figure 3-6, the paths finally converge to the same strain value indicating that the strain equivalence assumption holds true.

4. FAILURE SUB-MODEL

4.1 THEORETICAL BACKGROUND

The failure models implemented into MAT213 are discussed in the following sections.

4.1.1 Principal strain failure criterion (PSFC)

This is a strain-based failure model [34]. The failure is assumed to take place if the strain in any of the PMDs exceeds the ultimate strain obtained from the experiments in the given direction. The failure criterion is satisfied if any one of the equations 4.1 or 4.3 is satisfied.

$$\frac{\varepsilon_{ii}}{\left(\varepsilon_u\right)_{ii}} - 1 \geq 0 \quad i = 1,2,3 \tag{4.1}$$

where:

$$\left(\varepsilon_u\right)_{ii} = \begin{cases} \left(\varepsilon_u^t\right)_{ii} \; if \; \varepsilon_{ii} > 0 \\ \left(\varepsilon_u^c\right)_{ii} \; if \; \varepsilon_{ii} < 0 \end{cases} \tag{4.2}$$

or:

$$\frac{\left|\varepsilon_{ij}\right|}{\left(\varepsilon_u\right)_{ij}} - 1 \geq 0 \quad , ij = 12, 23, 13 \tag{4.3}$$

where ε_u is the ultimate strain obtained from experiments.

4.1.2 Tsai-Wu failure criterion (TWFC)

As mentioned earlier, Tsai-Wu failure criterion [35] is an interactive second order tensor polynomial criterion which considers the interaction of stresses. The failure criterion is satisfied if $f\left(\sigma\right) > 0$, where:

$$\begin{aligned} f\left(\sigma\right) = -1 &+ F_1\sigma_{11} + F_2\sigma_{22} + F_3\sigma_{33} + F_{11}\sigma_{11}^2 + F_{22}\sigma_{22}^2 + F_{33}\sigma_{33}^2 \\ &+ F_{44}\sigma_{12}^2 + F_{55}\sigma_{23}^2 + F_{66}\sigma_{13}^2 + 2F_{12}\sigma_{11}\sigma_{22} + 2F_{23}\sigma_{22}\sigma_{33} + 2F_{13}\sigma_{11}\sigma_{33} \end{aligned} \tag{4.4}$$

where

$$\begin{aligned} F_1 &= \frac{1}{\hat{\sigma}_{11}^T} - \frac{1}{\hat{\sigma}_{11}^C} & F_{11} &= \frac{1}{\hat{\sigma}_{11}^T\hat{\sigma}_{11}^C} & F_{44} &= \frac{1}{\hat{\sigma}_{12}^2} \\ F_2 &= \frac{1}{\hat{\sigma}_{22}^T} - \frac{1}{\hat{\sigma}_{22}^C} & F_{22} &= \frac{1}{\hat{\sigma}_{22}^T\hat{\sigma}_{22}^C} & F_{55} &= \frac{1}{\hat{\sigma}_{23}^2} \\ F_3 &= \frac{1}{\hat{\sigma}_{33}^T} - \frac{1}{\hat{\sigma}_{33}^C} & F_{33} &= \frac{1}{\hat{\sigma}_{33}^T\hat{\sigma}_{33}^C} & F_{66} &= \frac{1}{\hat{\sigma}_{13}^2} \end{aligned} \tag{4.5}$$

$$F_{12} = -\frac{1}{2}\sqrt{F_{11}F_{22}} \quad 4.6$$

$$F_{23} = -\frac{1}{2}\sqrt{F_{22}F_{33}} \quad 4.7$$

$$F_{13} = -\frac{1}{2}\sqrt{F_{11}F_{33}} \quad 4.8$$

$\hat{\sigma}$ denotes the stress value corresponding to failure obtained from experiments.

4.2 IMPLEMENTATION DETAILS

4.2.1 Algorithm used for PSFC and TWFC

The failure criterion is checked at a given integration point. Failure is assumed to take place if the stress/strain state at the given integration point satisfies equations 4.1 or 4.3 for PSFC and equation 4.4 for TWFC. The current implementation is such that if any of these integration points fails, the element corresponding to this integration point(s) is deleted.

4.3 MODEL VERIFICATION

The four failure models discussed in sections 4.1 and 4.2 have been verified and presented in this section. The FE models used for the verification for the combined deformation and the failure model are the same as the ones used in section 2.3 The strength parameters of the T800/F3900 composite obtained from the experiments on coupon level are listed in Table 4-1.

Table 4-1. T800S/F3900 strength parameters

Component	Failure/Ultimate strain		Failure stress (psi)	
Tension 1-direction	$\left(\varepsilon_u^t\right)_{ii}$	0.01561	$\hat{\sigma}_{11}^T$	366097
Tension 2-direction	$\left(\varepsilon_u^t\right)_{ii}$	0.00622	$\hat{\sigma}_{22}^T$	6491
Tension 3-direction	$\left(\varepsilon_u^t\right)_{ii}$	0.00421	$\hat{\sigma}_{33}^T$	4002
Compression 1-direction	$\left(\varepsilon_u^c\right)_{ii}$	0.00629	$\hat{\sigma}_{11}^C$	105765
Compression 1-direction	$\left(\varepsilon_u^c\right)_{ii}$	0.04127	$\hat{\sigma}_{22}^C$	25548
Compression 1-direction	$\left(\varepsilon_u^c\right)_{ii}$	0.02856	$\hat{\sigma}_{33}^C$	25261
Shear 1-2 plane	$\left(\varepsilon_u\right)_{12}$	0.13316	$\hat{\sigma}_{12}$	18624
Shear 2-3 plane	$\left(\varepsilon_u\right)_{23}$	0.00428	$\hat{\sigma}_{23}$	2816
Shear 1-3 plane	$\left(\varepsilon_u\right)_{13}$	0.07015	$\hat{\sigma}_{13}$	12429

4.3.1 Single Element Verification Test

4.3.1.1 1-Direction Tension Test and 1-Direction Compression Test

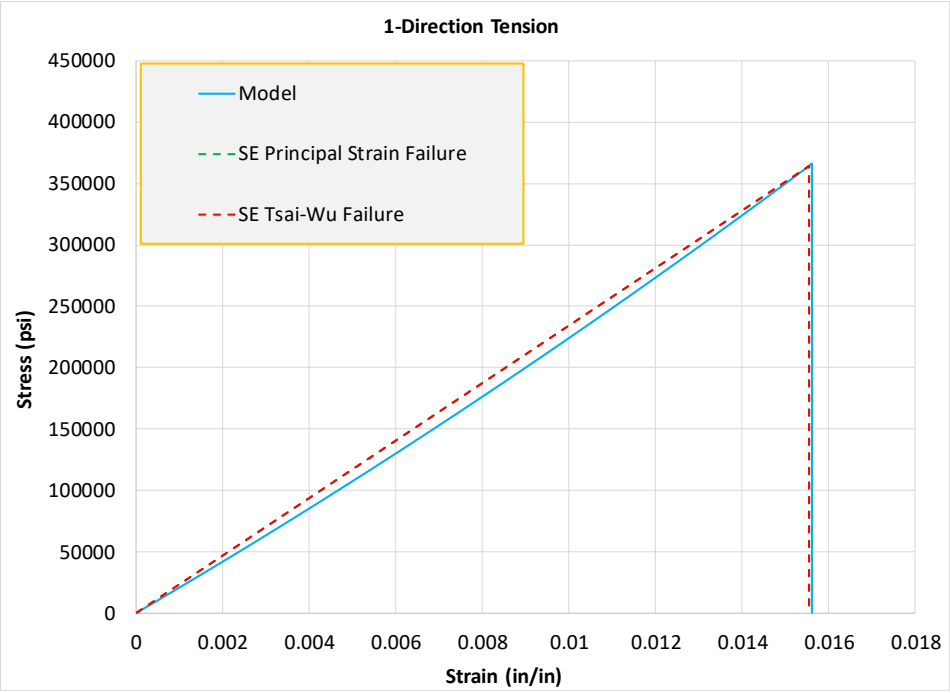

Figure 4-1. 1-Direction Tension Stress-Strain Plot

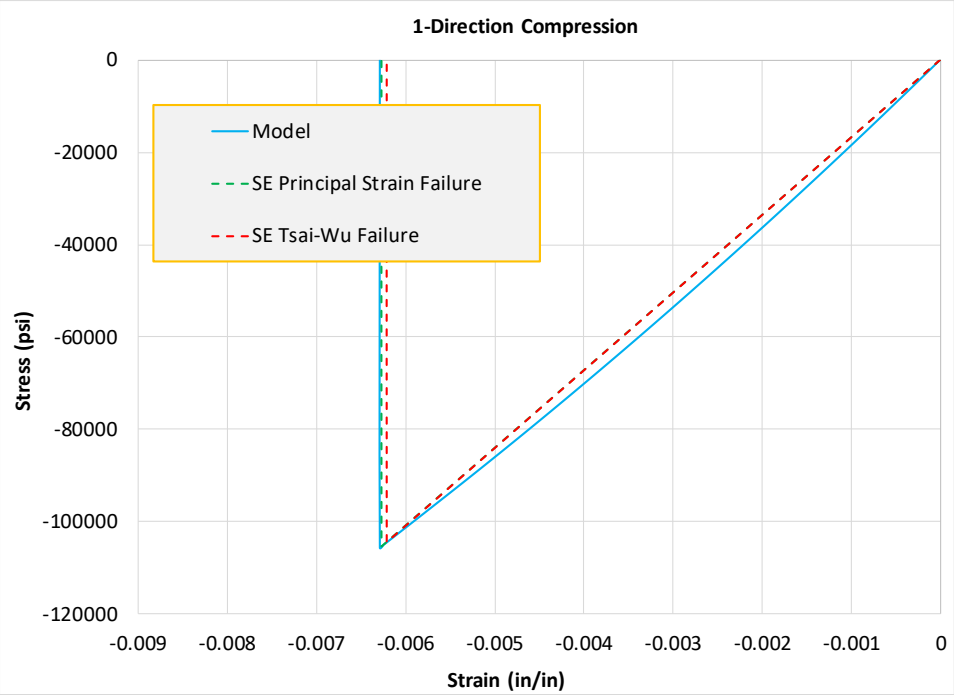

Figure 4-2. 1-Direction Compression Stress-strain plot

The results show that the failure models are correctly implemented.

4.3.1.2 2-Direction Tension Test and 2-Direction Compression Test

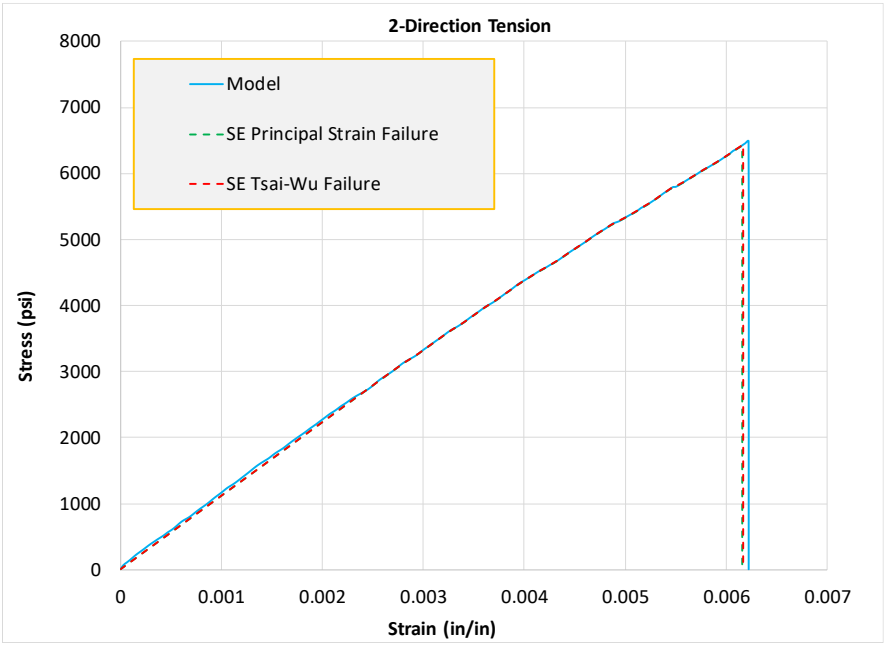

Figure 4-3. 2-Direction Tension Stress-Strain Plot

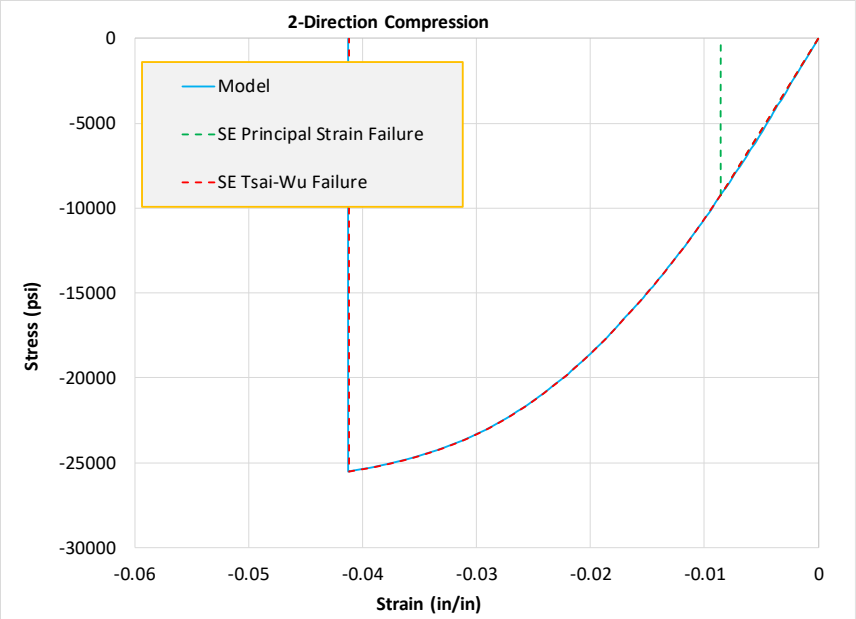

Figure 4-4. 2-Direction Compression Stress-Strain Plot

For 2-direction compression, principal strain failure is detected in the element as the normal (tensile) strain in the 3-direction exceeds the failure strain (0.00421) in that direction. This is due to Poisson's effect $\left(\nu_{23}^{T}=0.484,\nu_{32}^{T}=0.439\right)$. The results show that the failure models are correctly implemented.

4.3.1.3 3-Direction Tension Test and 3-Direction Compression Test

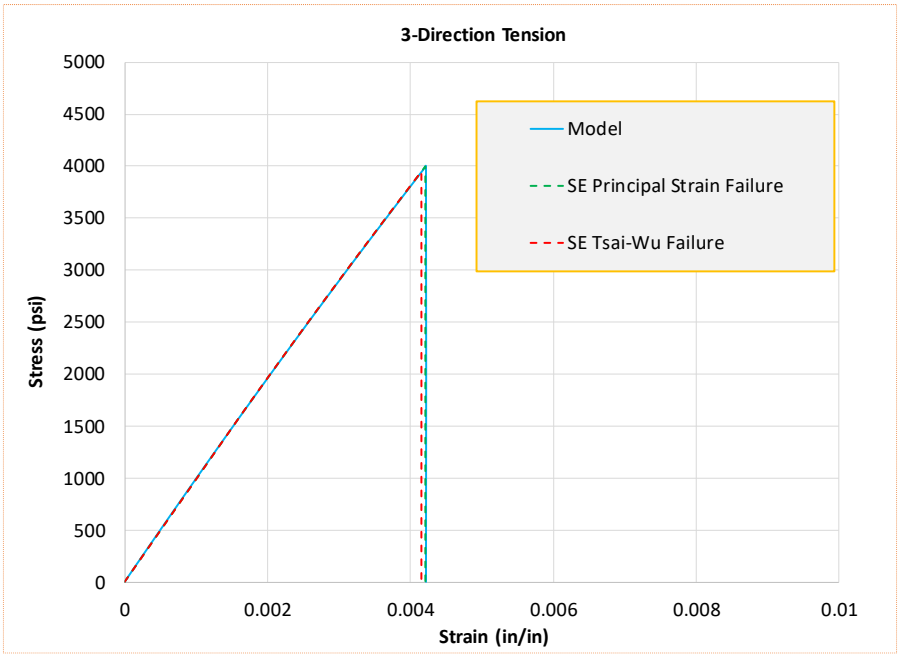

Figure 4-5. 3-Direction Tension Stress-Strain Plot

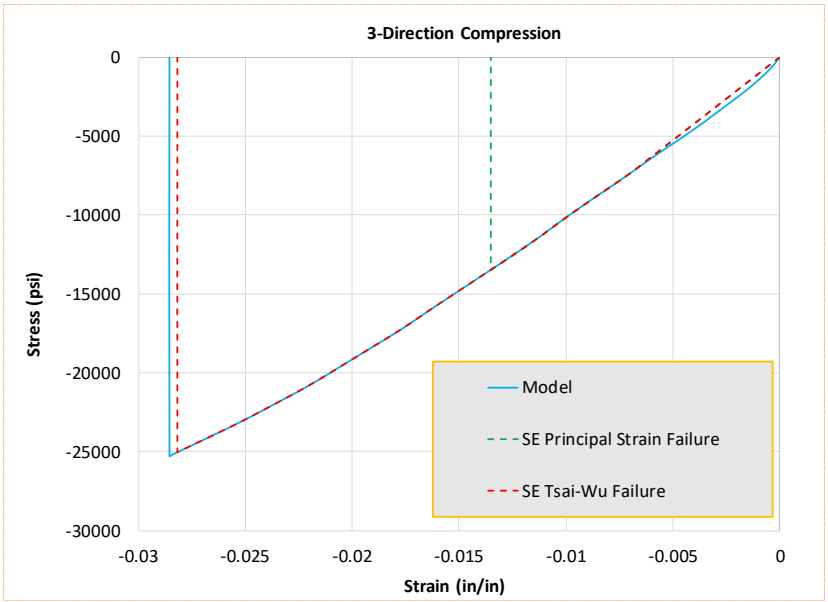

Figure 4-6. 3-Direction Compression Stress-Strain plot

For 3-direction compression, principal strain failure is detected in the element as the normal (tensile) strain in the 2-direction exceeds the failure strain in that direction (0.00622). This is due to Poisson's effect $\left(\nu_{23}^{T}=0.484,\nu_{32}^{T}=0.439\right)$. The results show that the failure models are correctly implemented.

4.3.1.4 1-2 Plane Shear Test

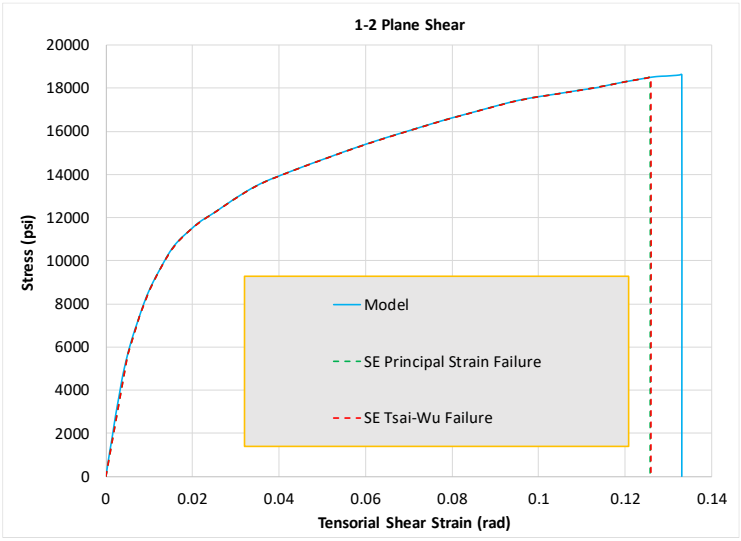

Figure 4-7. 1-2 Plane Shear Stress-Strain Plot

The results show that the failure models are correctly implemented.

4.3.1.5 2-3 Plane Shear Test

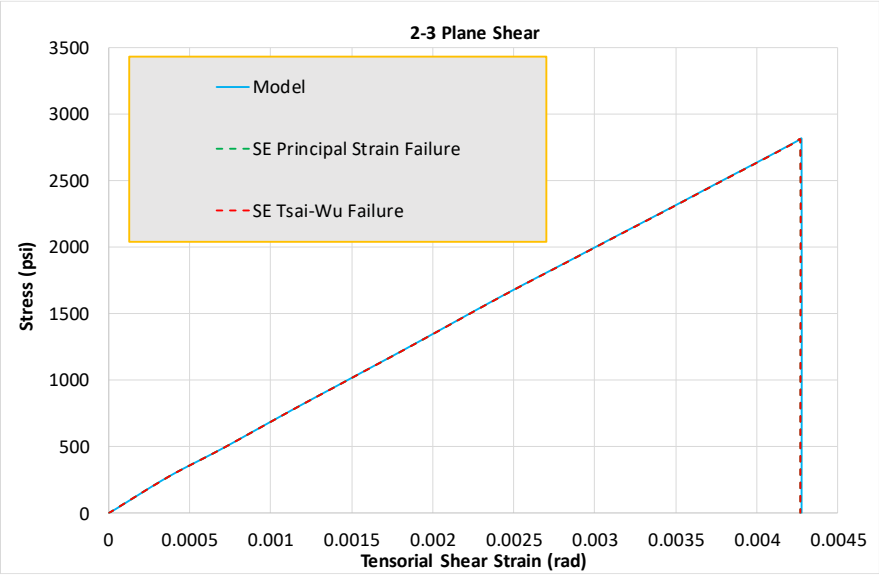

Figure 4-8. 2-3 Plane Shear Stress-Strain Plot

The results show that the failure models are correctly implemented.

4.3.1.6 1-3 Plane Shear Test

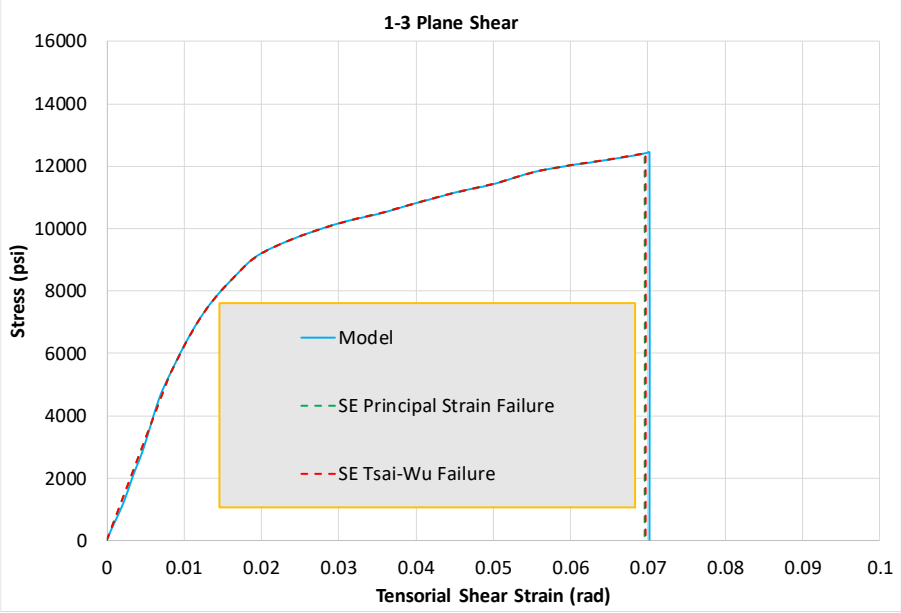

Figure 4-9. 1-3 Plane Shear Stress-Strain Plot

The results show that the failure models are correctly implemented.

4.3.1.7 1-2 Plane 45° Off-Axis Tension

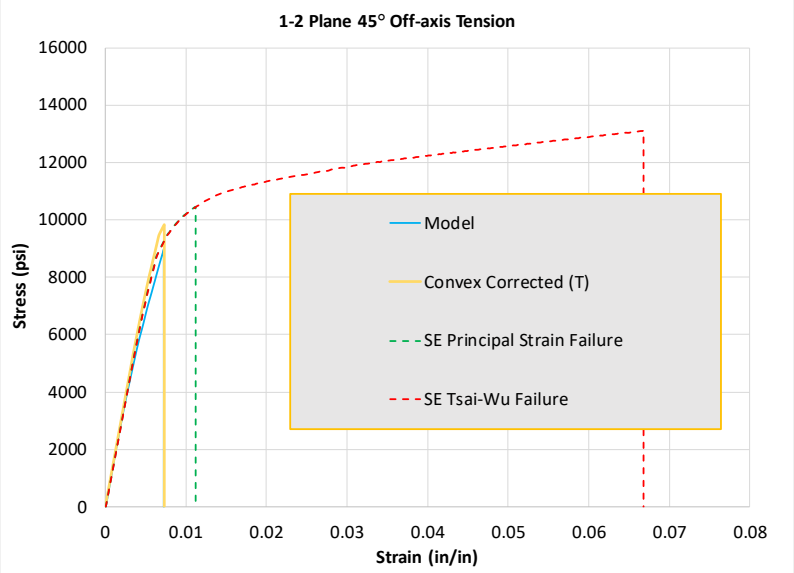

Figure 4-10. 1-2 Plane 45° Off-Axis Tension Stress-Strain Plot

The late failure taking place is due to the convex correction [36].

4.3.1.8 2-3 Plane 45° Off-Axis Compression

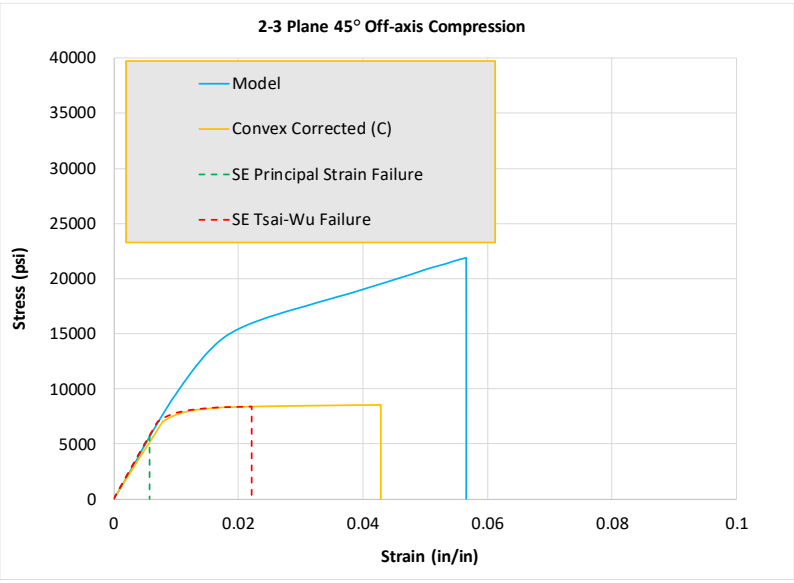

Figure 4-11. 2-3 Plane 45° Off-Axis Compression Stress-Strain Plot

The premature failure occurs in case of PSFC because the model fails in shear 2-3 strain component. The failure takes place prematurely using TWFC due to the convex correction [36].

4.3.1.9 1-3 Plane 45° Off-Axis Compression

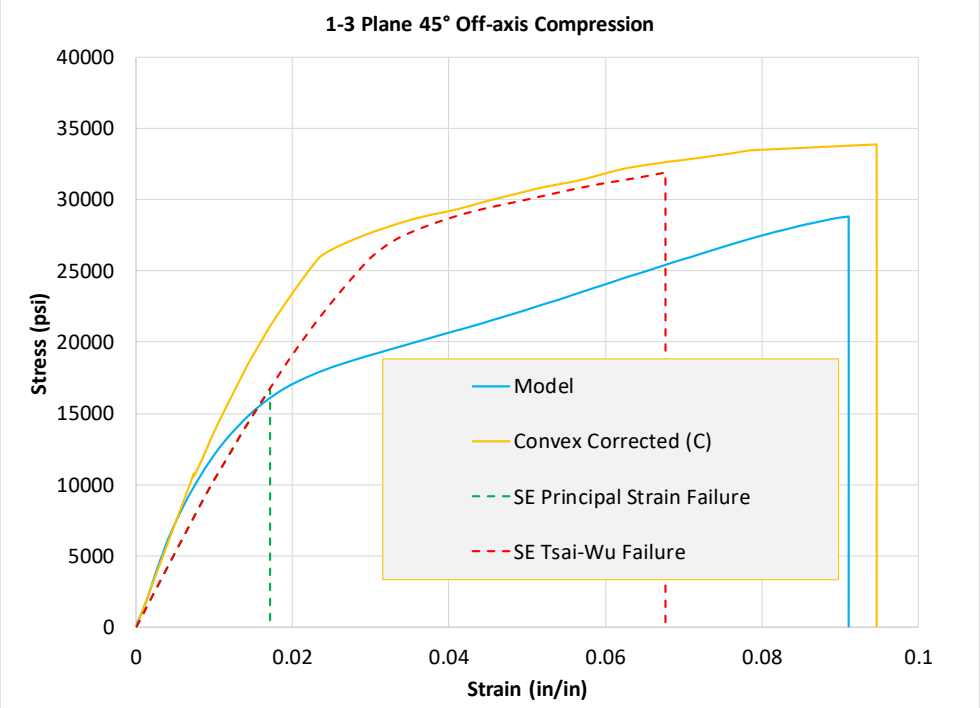

Figure 4-12. 1-3 Plane 45° Off-Axis Compression Stress-Strain Plot

The premature failure occurs in case of PSFC because the model fails in shear 2-3 strain component. The failure takes place prematurely using TWFC due to the convex correction.

4.3.2 Multi-Element Verification Test

4.3.2.1 1-Direction Tension Test

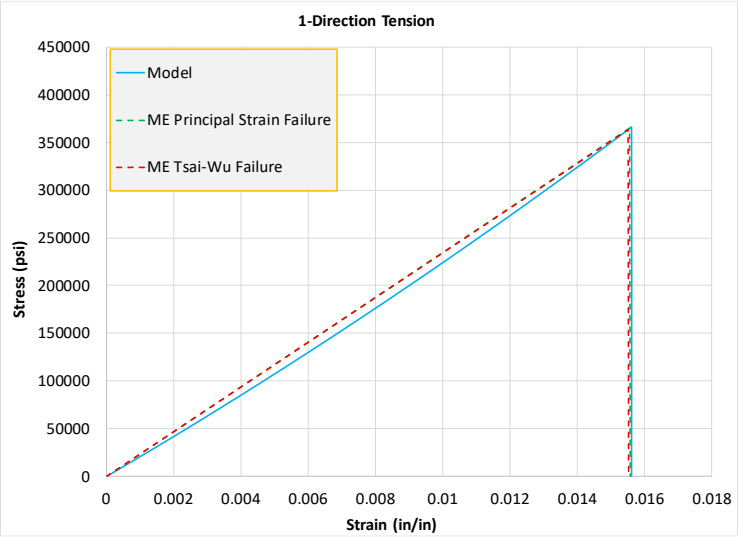

Figure 4-13. 1-direction tension stress-strain plot

The results show that the failure models are correctly implemented.

4.3.2.2 1-Direction Compression Test

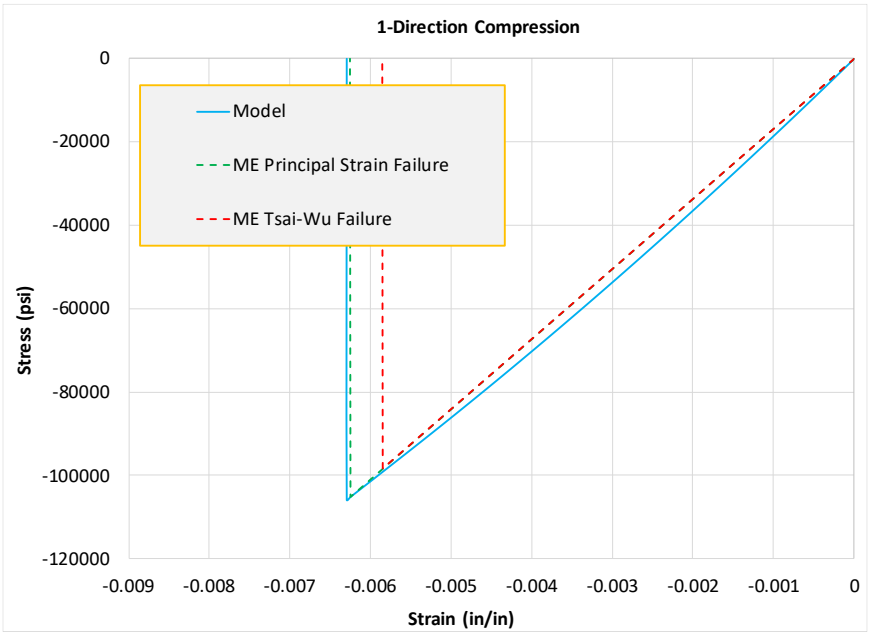

Figure 4-14. 1-direction compression stress-strain plot

The results show that the failure models are correctly implemented.

4.3.2.3 2-Direction Tension Test

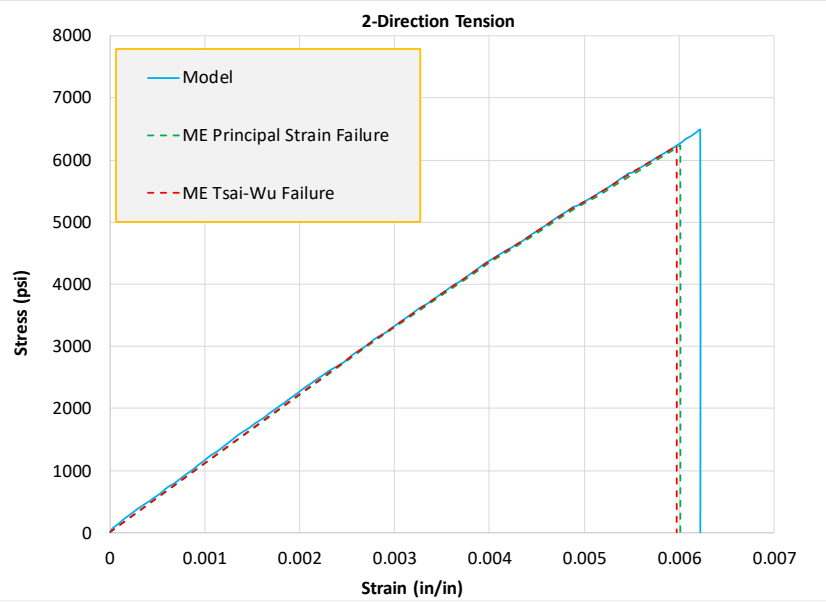

Figure 4-15. 2-direction tension stress-strain plot

The results show that the failure models are correctly implemented.

4.3.2.4 2-Direction Compression Test

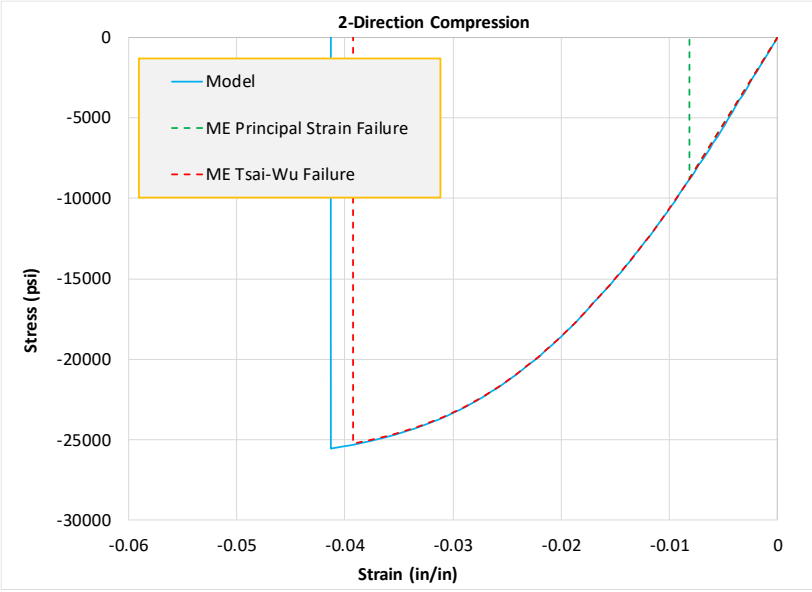

Figure 4-16. 2-direction compression stress-strain plot

The premature failure exhibited by the FE simulation using PSFC is caused by the strain concentration present near the boundary. The elements fail due to exceeding the allowable tension strain in the 3-direction.

4.3.2.5 3-Direction Tension Test

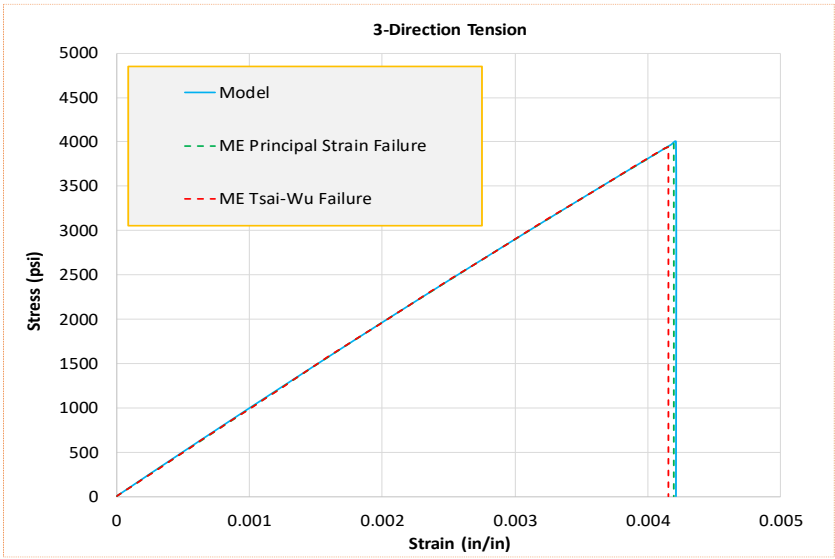

Figure 4-17. 3-direction tension stress-strain plot

The results show that the failure models are correctly implemented.

4.3.2.6 3-Direction Compression Test

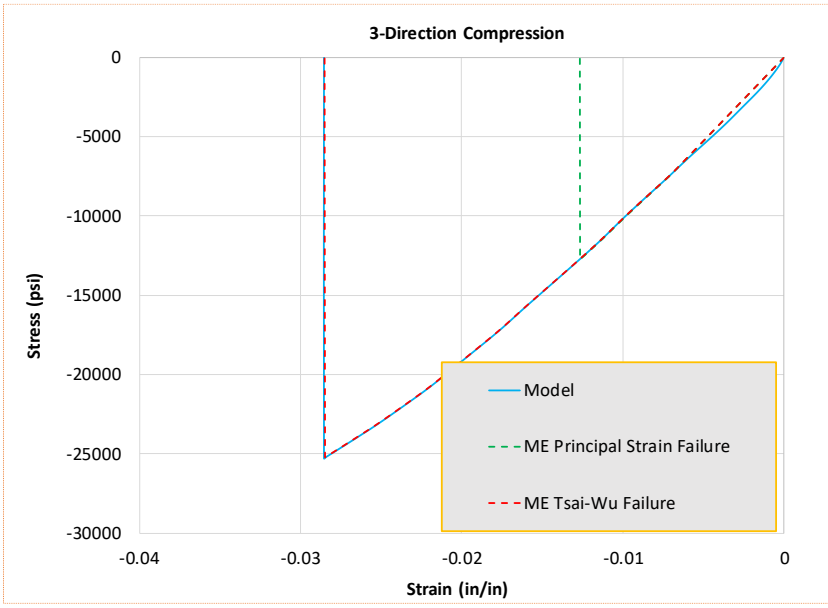

Figure 4-18. Stress-strain plot for 3-direction compression test

The FE models fail prematurely with PSFC because the allowable tension strain in the 2-direction was exceeded.

4.3.2.7 1-2 Plane Shear

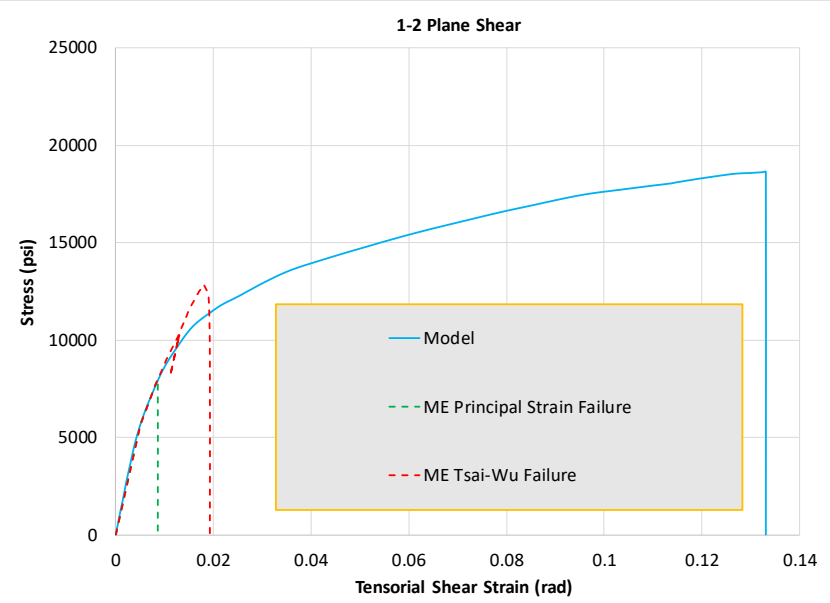

Figure 4-19. 1-2 plane shear stress-strain plot

The FE models fail prematurely because elements near the notch root begin to fail. This behavior is consistent with the experimental observations.

4.3.2.8 2-3 Plane Shear Test

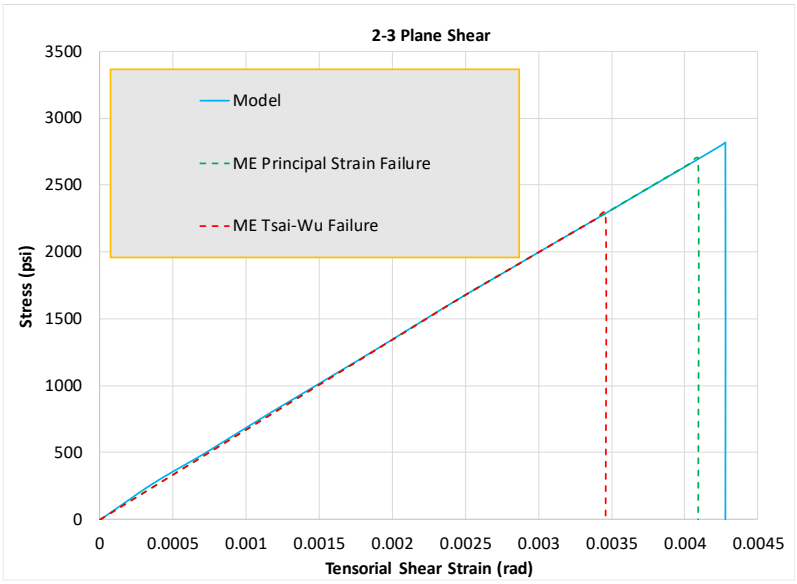

Figure 4-20. 2-3 plane shear stress-strain plot

The FE models fail prematurely because elements near the notch root begin to fail.

4.3.2.9 1-3 Plane Shear

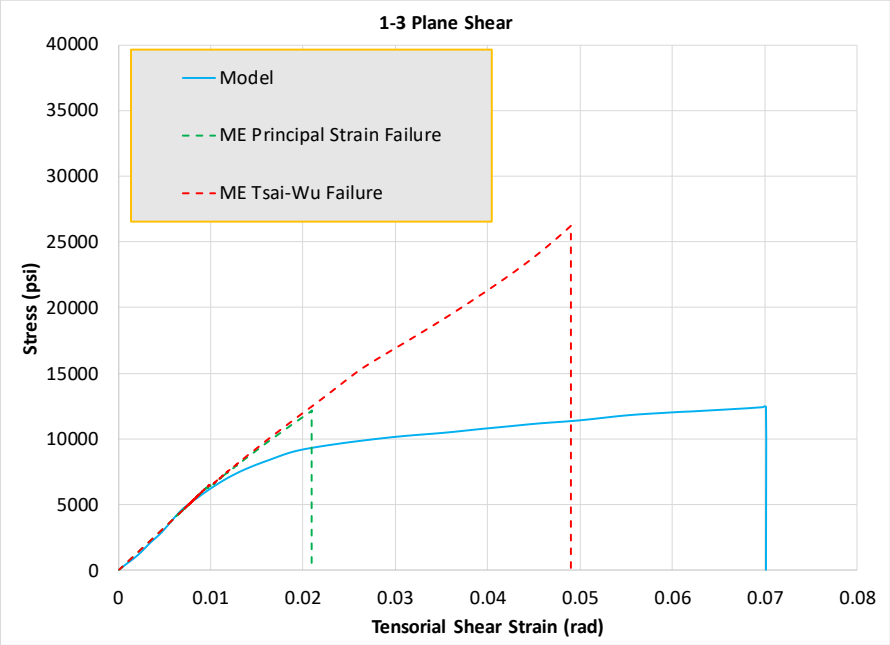

Figure 4-21. 1-3 plane shear stress-strain plot

4.3.2.10 1-2 Plane 45° Off-Axis Tension

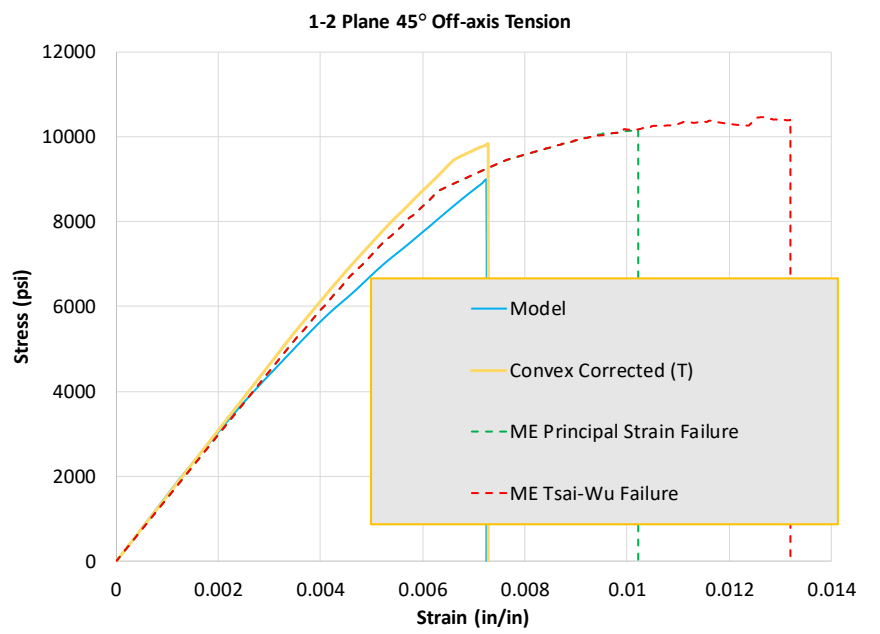

Figure 4-22. 1-2 plane 45° off-axis tension stress-strain plot

There is late failure because of the convex correction.

4.3.2.11 2-3 Plane 45° Off-Axis Compression

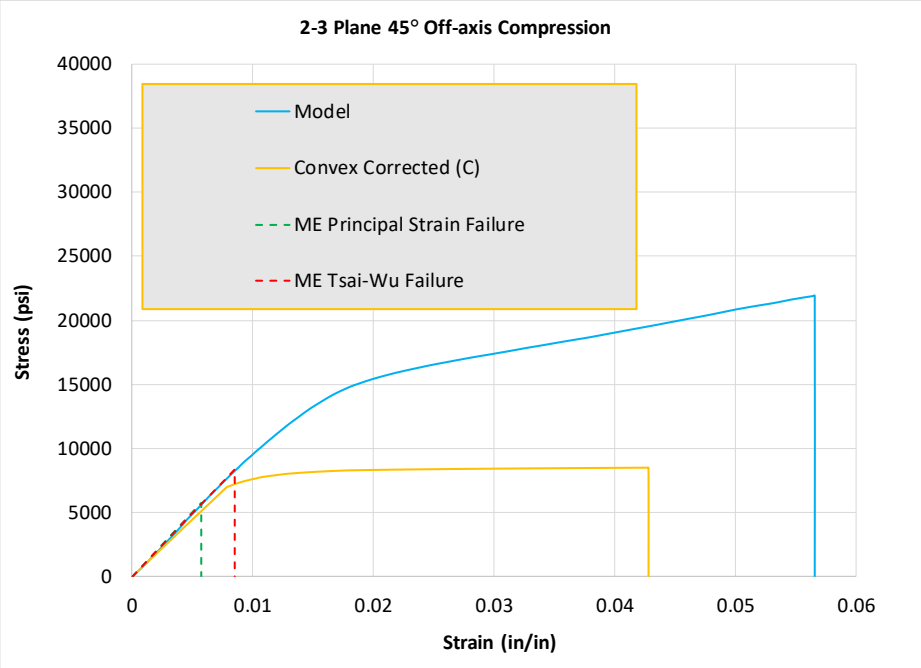

Figure 4-23. 2-3 plane 45° off-axis compression stress-strain plot

The premature failure occurs in the case of PSFC because the elements in the model start failing in shear 2-3 strain component. The failure takes place prematurely using TWFC due to the convex correction.

4.3.2.12 1-3 Plane 45° Off-Axis Compression

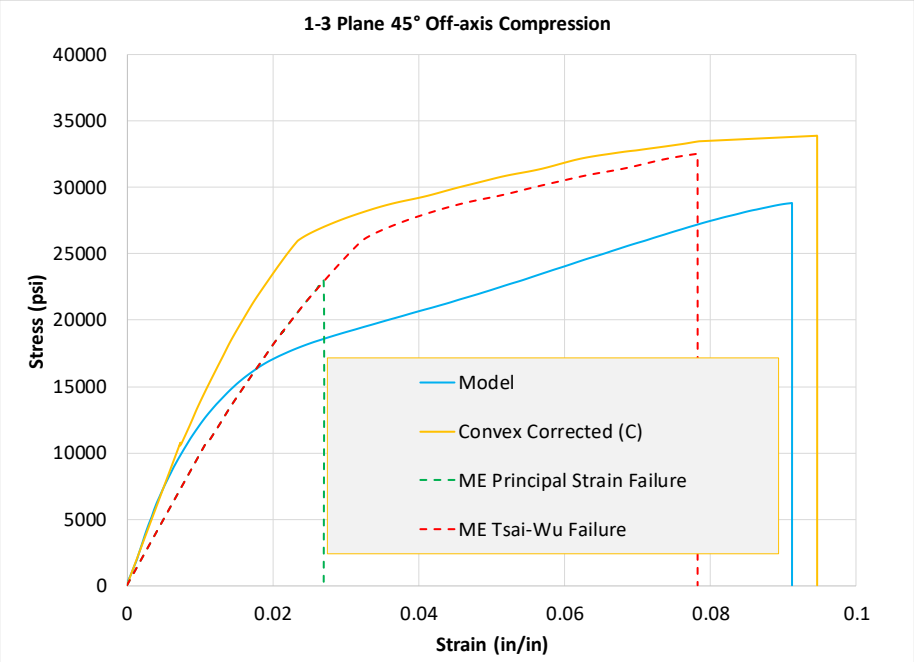

Figure 4-24. 1-3 plane 45° off-axis compression stress-strain plot

The premature failure occurs in case of PSFC because the elements in the model starts failing in shear 2-3 strain component. The failure takes place prematurely using TWFC due to the convex correction.

5. MODEL VALIDATION

Several impact validation tests were performed in order to exercise the deformation and damage sub-models of MAT213. The experiments, which were used to compare with the simulations, were performed at the NASA-GRC Ballistic Impact Lab. Extensive experimental details are provided in ASTM D8101/D8101-17 [37]. Each respective experiment underwent varying degrees of deformation and damage during the impact event. All validation simulations used experimental data corresponding to the T800/F3900 unidirectional composite that can be found in Khaled et al. [38] and Khaled et al. [33].

A similar experimental setup was used for all impact tests. Digital image correlation (DIC) was used to track both strain and displacement fields throughout the duration of the experimental event. Figure 5-1(a) shows the clamping mechanism used to hold the composite panel during the experiment. Figure 5-1(b) shows the aluminum impactor used as the projectile for the experiment. The impactor had a mass of 50 g.

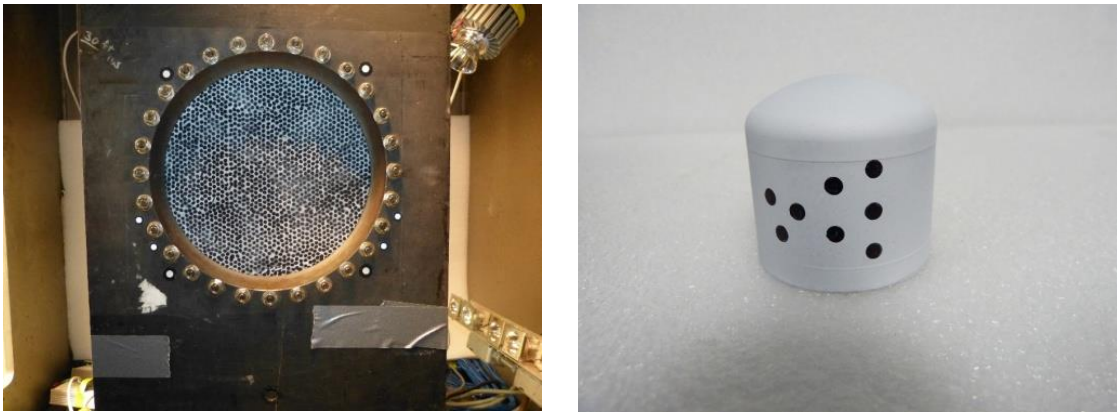

(a) (b)

Figure 5-1. Experimental setup (a) clamping system and (b) aluminum projectile

Figure 5-2 shows the T800/F3900 composite panels used in the experiment. Figure 5-2(a) shows the panel used in the LVG 906 experiment, while Figure 5-2(b) shows the composite panel used for both LVG 1064 and LVG 1071.

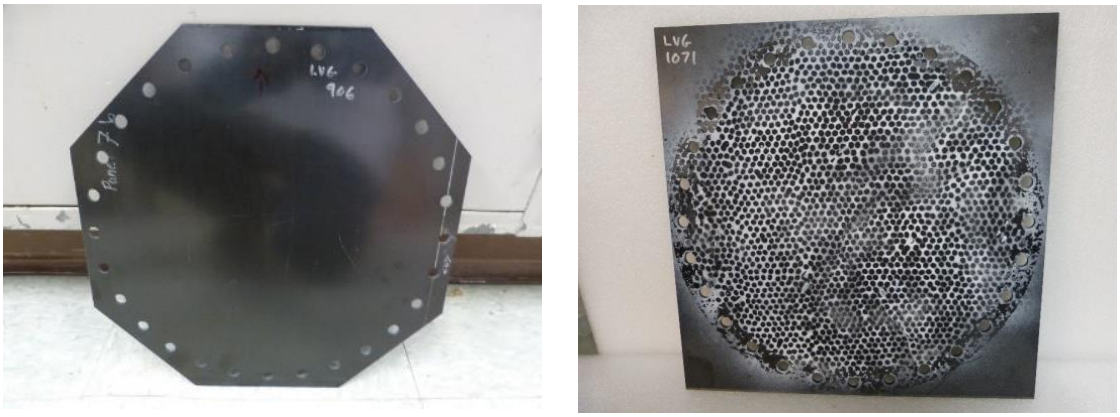

(a) (b)

Figure 5-2. Composite panels used in experiments (a) LVG 906 and (b) LVG 1064 and LVG 1071

Table 5-1 gives the details of the projectile velocity at impact for each experiment being assessed.

Table 5-1. Summary of Aluminum Projectile Impact Velocity

Simulation	Impact Velocity
LVG 906	8.35 m/s (27.4 ft/s)
LVG 1064	71.94 m/s (236 ft/s)
LVG 1071	47.25 m/s (155 ft/s)

The same constitutive properties were used for the aluminum projectile in each of the three simulations. The projectile is modeled using 17,040 8-noded hexahedral elements with a single integration point. A piecewise linear plasticity material model (LS-DYNA Mat 24) was used. Table 5-2 gives the properties used to drive the model.

Table 5-2. MAT024 Properties for Aluminum Impactor

Model Parameter	Value
Mass density ($\frac{lb \cdot s^2/in}{in^3}$)	2.539(10^{-4})
E (psi)	10.30(10^6)
ν	0.334
Yield Stress, SIGY (psi)	42500
Tangent Modulus, ETAN (psi)	42000

The panel used in the LVG 906 experiment was comprised of a $[0]_{16}$ layup, while the panels used for both the LVG 1064 and LVG 1071 experiments were comprised of a $[(0/90/45/-45)_2]_S$ layup. All of the respective panels were approximately 3.1 mm in thickness (0.122 in).

5.1 LVG 906

To strike a balance between accuracy and computational efficiency, a convergence study was carried out to find the optimal mesh to use in the LVG 906 impact simulation. The study yielded a mesh with 214,752 8-noded hexahedral elements with one-integration point and LS-DYNA hourglass control type 6. Three elements were used through the thickness to model 16 plies.
Figure 5-3 shows the nodes meant to mimic the restraints imposed by the bolted connection in the experiment. All nodes highlighted in
Figure 5-3 are restrained completely from translation.

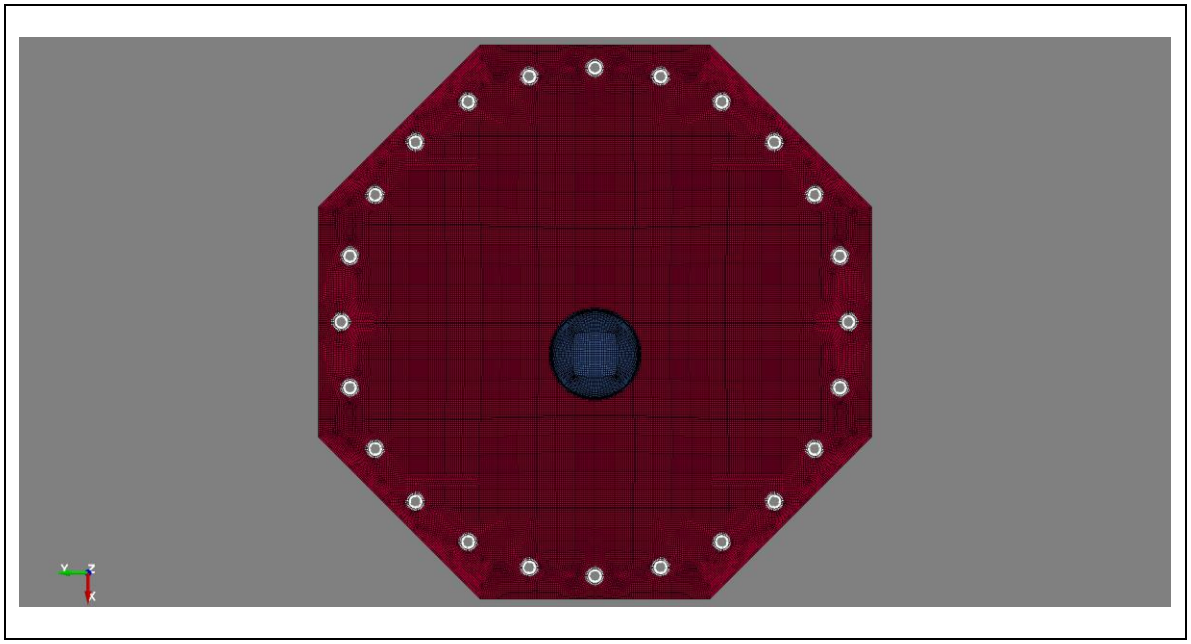

Figure 5-3. FE model showing constrained nodes

A comparison of the out-of-plane displacement contour at the time of maximum displacement for both the experiment, captured using DIC, and the finite element simulation is shown in Figure 5-4.

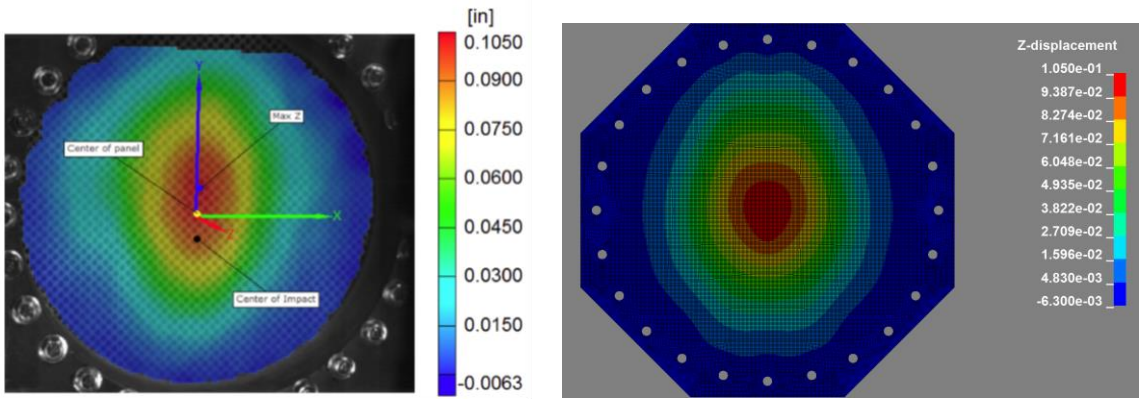

(a) (b)

Figure 5-4. Contour of out of plane displacement at t=0.0007 s (a) experiment, and (b) finite element simulation

Qualitatively, the contour plots shown in Figure 5-4 are similar. A comparison of the out-of-plane displacement plots for both the finite element simulation and the experiment throughout the duration of the event is shown in Figure 5-5. “Max” refers to the node at which the maximum displacement occurs, and “Center” refers to displacement at the center of the panel.

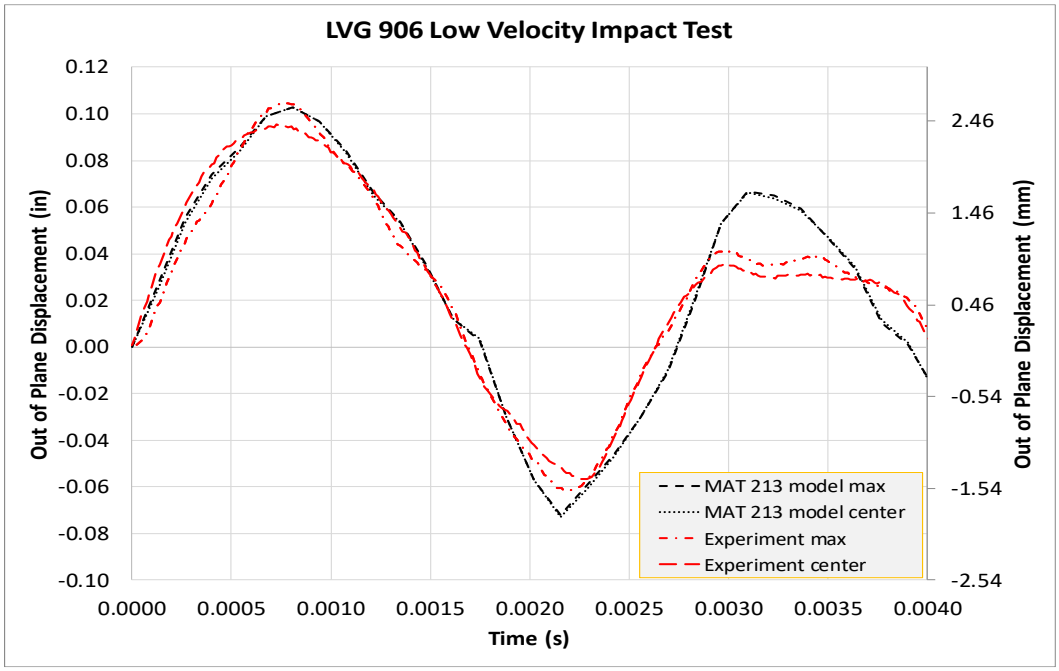

Figure 5-5. Comparison of out of plane displacement data for both the experiment and the finite element simulations

The simulation shows good agreement with the experimental data. The first positive peak values are relatively close. The first negative peak value is slightly over-predicted, but the period match is good even for the second positive peak. However, the second positive peak displacement is larger than the experimental value. The differences may be attributed to the following differences between the experiment and the simulation. First, the impact was not a direct hit – the roll, pitch, and yaw angles of the impactor were not all zero. In the simulation, these values were assumed to be zero. Second, it is possible that there was small permanent damage in the panel, though not visible to the eye. Lastly, since no damping parameters were included in the model, both the first negative and the second positive peak values are greater than the experiment.

5.2 LVG1071

A convergence study was performed to obtain the optimal mesh to use for the composite panel in the LVG 1071 simulation. The study yielded a mesh comprised of 370,184 8-noded hexahedral elements for the composite plies with 16 elements through the thickness to represent each of the 16 plies. These 16 plies were modeled using MAT213 with the respective orientation of the fibers in each ply being properly accounted for. Figure 5-6 shows the FE model along with the nodes given translational restraints to mimic the bolts and clamp in the experiment. The nodes highlighted in Figure 5-6(a) were fixed from in-plane translations while the nodes highlighted in Figure 5-6(b) were fixed from out-of-plane translations. These restraints were obtained from a study performed to observe how sensitive the finite element model response is to changes in the boundary conditions.

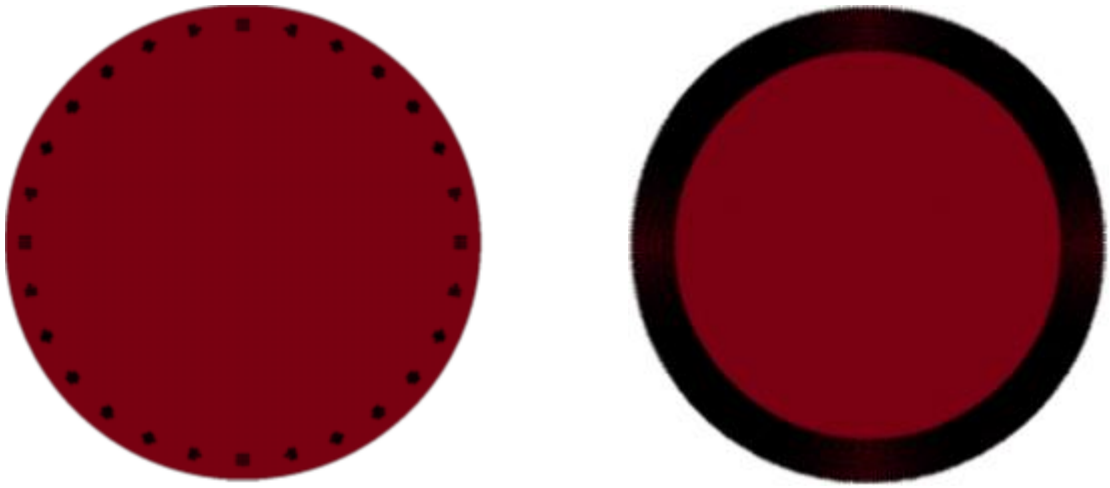

(a) (b)

Figure 5-6. LS-DYNA finite element model (a) back view, (b) side view

Cohesive zone elements, with a thickness of 10^{-4} in, were used between each of the adjacent composite plies to capture any delamination that may have occurred. The cohesive elements were modeled using 8-noded hexahedral elements with MAT 138. The MAT 138 properties are given in Table 5-3.

Table 5-3. Cohesive Zone Model Parameters Used with MAT 138

Parameter	Value
$G_{IC}\ \left(J/mm^2, (lb\cdot in)/in^2\right)$	0.75, 4.28
$G_{IIC}\ \left(J/mm^2, (lb\cdot in)/in^2\right)$	2.54, 14.50
$E_N\ \left(MPa/mm, \left(lb/in^2\right)/in\right)$	$1.67(10)^5$, $6.16(10)^8$
$E_T\ \left(MPa/mm, \left(lb/in^2\right)/in\right)$	$1.67(10)^5$, $6.16(10)^8$
T $\left(MPa, lb/in^2\right)$	28, 4000
S $\left(MPa, lb/in^2\right)$	56, 8000
XMU	1.00

The *CONTACT_ERODING_ SURFACE_TO_SURFACE contact definition was used to handle contact between the aluminum impactor and composite panel while the *CONTACT_ERODING_SINGLE_ SURFACE contact definition was used to handle contact between the individual plies of the composite panel. During the experiment, the projectile was completely contained by the composite panel. An ultrasonic scan of the panel after testing, Figure 5-7, shows minor damage near the impact zone illustrated by the dark grey region near the center of the panel.

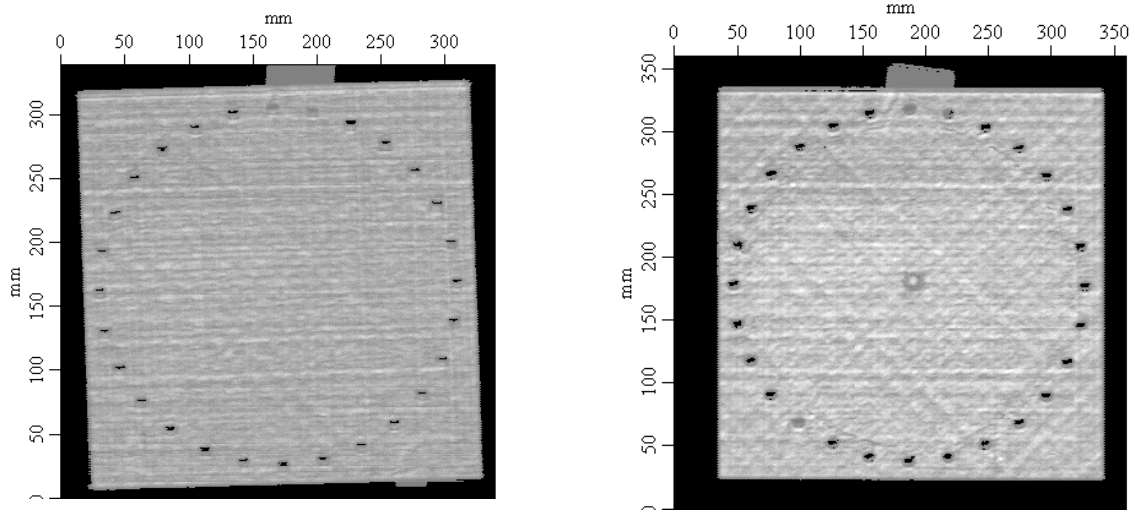

(a) (b)

Figure 5-7. Ultrasonic scan images of the plate (a) before impact (b) after impact

The projectile was completely contained by the composite plate, however, since there was some observable damage shown in the ultrasonic scan, both the deformation and damage sub models were exercised in the LVG 1071 simulations.

Several simulations were performed to exercise both the deformation and damage sub models with the goal of determining which parameters had the most significant effect on the response of the composite panel. Nominally, it would be expected for a unidirectional composite to be transversely isotropic. However, micrograph images along with experimental data [22] show that this is likely not the case for this particular composite at the laminate level. “Fully orthotropic” (Table 5.4) indicates the input used for the model was taken directly from the results of the corresponding experiments. “Transversely isotropic” indicates that all 3-direction parameters were set to the 2-direction counterparts. Optical micrographs show that, at the ply level, the 2-direction and 3-direction are indistinguishable.

The experimental results from tests in the 3-direction inherently account for the laminated nature of the composite since part of the response is caused by delamination between the plies. Including this data in the material model input in addition to cohesive zone elements would essentially mean compounding these effects. The 2-direction provides a better representation of the transverse behavior, as it is less affected by the laminated nature of the test coupons as the loading is parallel to the ply boundaries and the interlaminar stresses are likely to be lower. Damage data has been experimentally obtained for a subset of the in-plane damage parameters, which may be defined in MAT213: $d_{22_C}^{22_C}$, d_{12}^{12}, $d_{22_C}^{22_T}$, and $d_{22_C}^{12}$. Using the transverse isotropy assumption, $d_{33_C}^{33_C}$, d_{13}^{13}, $d_{33_C}^{33_T}$, and $d_{33_C}^{13}$ may also be included in the simulation by setting them equal to their in-plane counterparts and a model including out-of-plane damage would use these parameters. Several configurations were devised and are summarized in Table 5.4 below.

Table 5.4. Material Models Exercised in the Finite Element Simulations

Material Model ID	Model Characteristics	Included Damage Parameters
FOMND	Fully orthotropic model with no damage parameters	N/A
FOMID	Fully orthotropic model with in-plane damage parameters only	$d_{22_C}^{22_C}$, d_{12}^{12}
TIMND	Transversely isotropic model with no damage parameters	N/A
TIMIOD	Transversely isotropic with in-plane and out-of-plane damage parameters	$d_{22_C}^{22_C}$, d_{12}^{12}, $d_{33_C}^{33_C}$, d_{13}^{13}

Only uncoupled damage terms were included in the corresponding simulations for ease of analysis and comparison. A comparison of the out-of-plane displacement contour at the time of maximum displacement for both the experiment, captured using DIC, and the finite element simulation is shown in Figure 5-8.

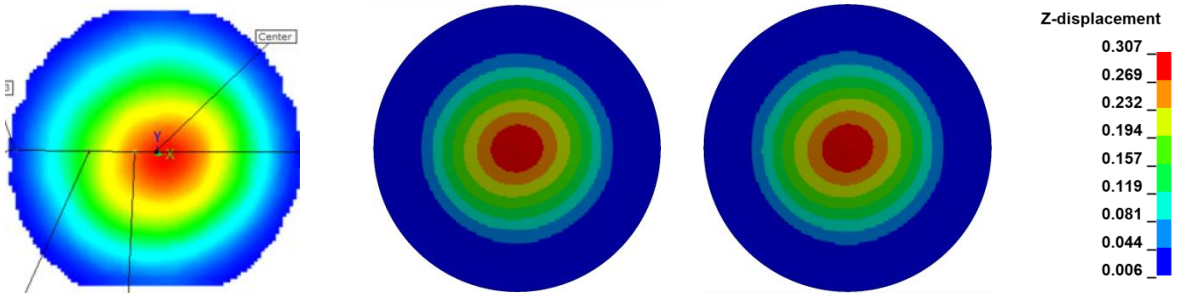

(a) (b) (c) (d)

Figure 5-8. Contour of the maximum out of plane displacement obtained during (a) experiment, (b) TIMND simulation, and (c) TIMIOD simulation (all plots taken at same instance of time)

Qualitatively, Figure 5-8 shows good agreement between the experimental and simulation results. Though the contours are only shown for the TIMND and TIMIOD simulations, the fully orthotropic simulations showed similar results.

Figure 5-9 gives a quantitative comparison of the out-of-plane displacement time history for the center of the composite plate.

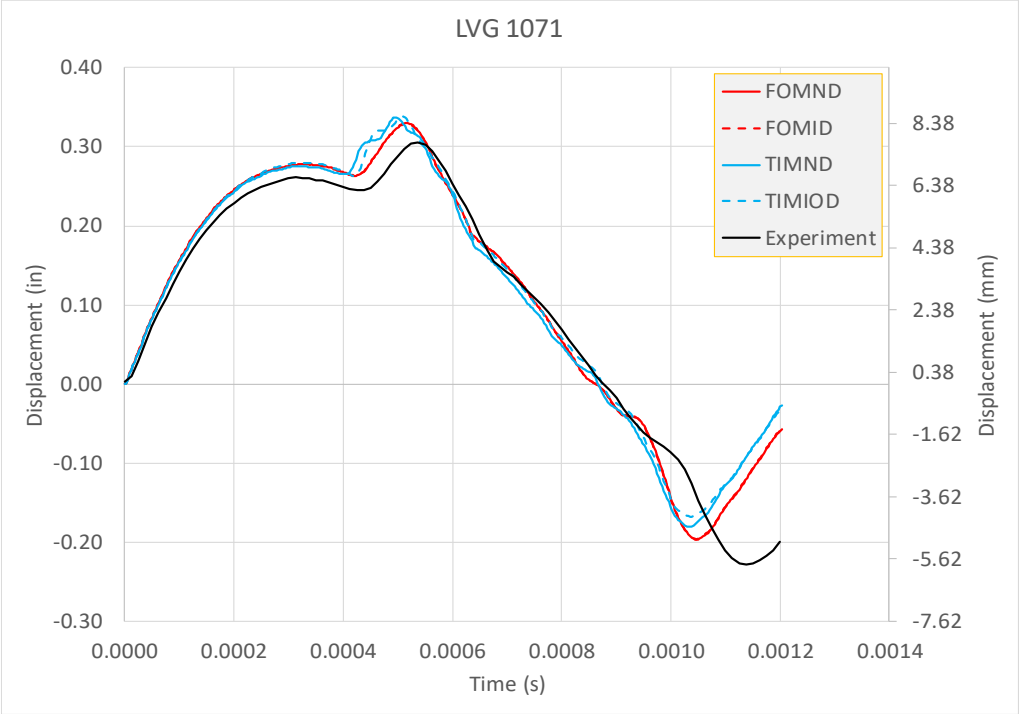

Figure 5-9. Comparison of out-of-plane (z) displacement versus time plot obtained from simulation and experiment

Figure 5-8 and figure 5-9 show that the damage sub-model had little impact on the results of the simulation. This would indicate that there is no significant damage present in model or experiment, i.e., it is highly localized. In addition to out-of-plane displacements, the major principal strain and horizontal strains are compared between the experiment and simulation below.

Figure 5-10 shows a comparison of the major principal strain contour at the instance of time when the maximum value occurs.

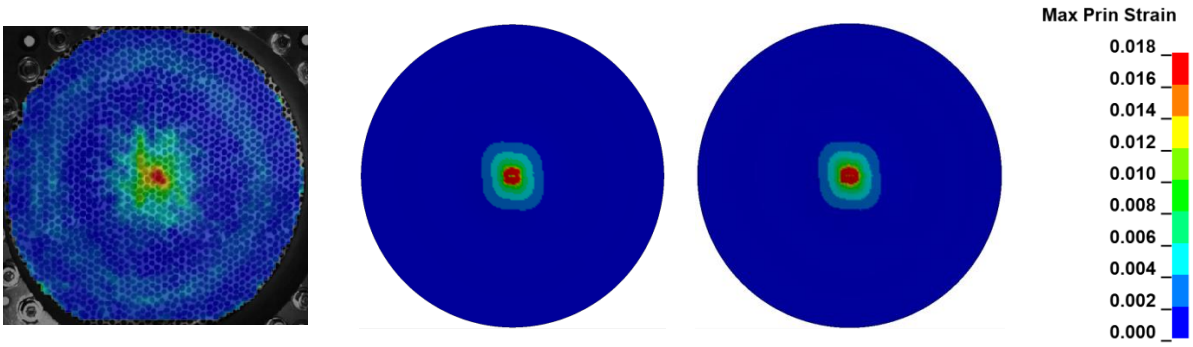

(a) (b) (c) (d)

Figure 5-10. Maximum principal strain contour (a) experiment, (b) TIMND simulation, (c) TIMIOD simulation, and (d) scale for all plots

Figure 5-11. provides a quantitative comparison of the time histories of the major principal strain at the center of the plate between the experiment and simulation.

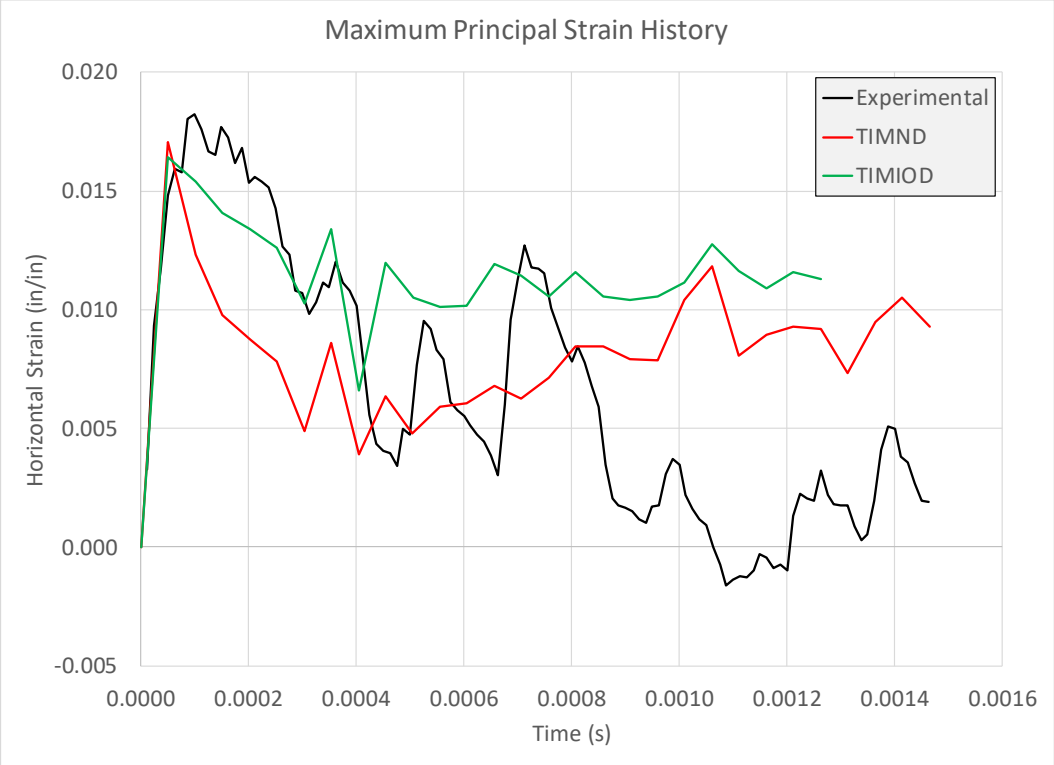

Figure 5-11. Maximum principal strain time history comparison

Figure 5-12. shows a comparison of the horizontal strain contour at the instance of time when the maximum value occurs.

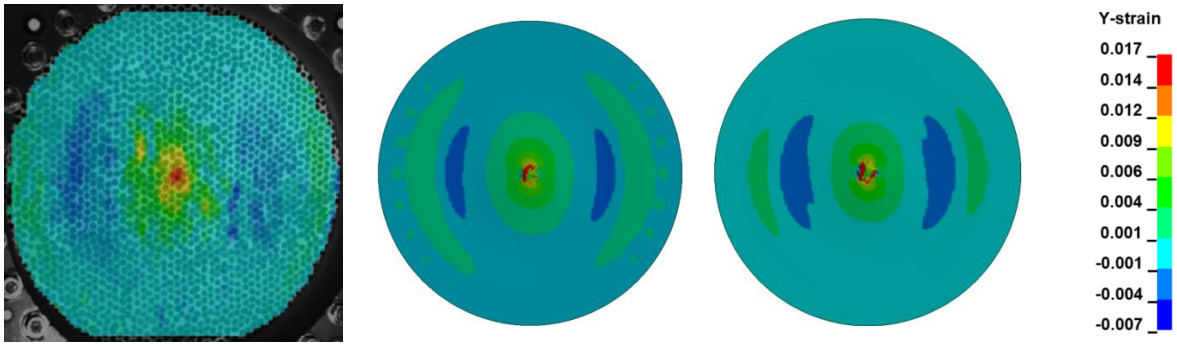

(a) (b) (c) (d)

Figure 5-12. Horizontal strain contour (a) experiment, (b) TIMND simulation, (c) TIMIOD simulation, and (d) scale for all plots

Figure 5-13 provides a quantitative comparison of the time histories of the horizontal strain at the center of the plate between the experiment and simulation.

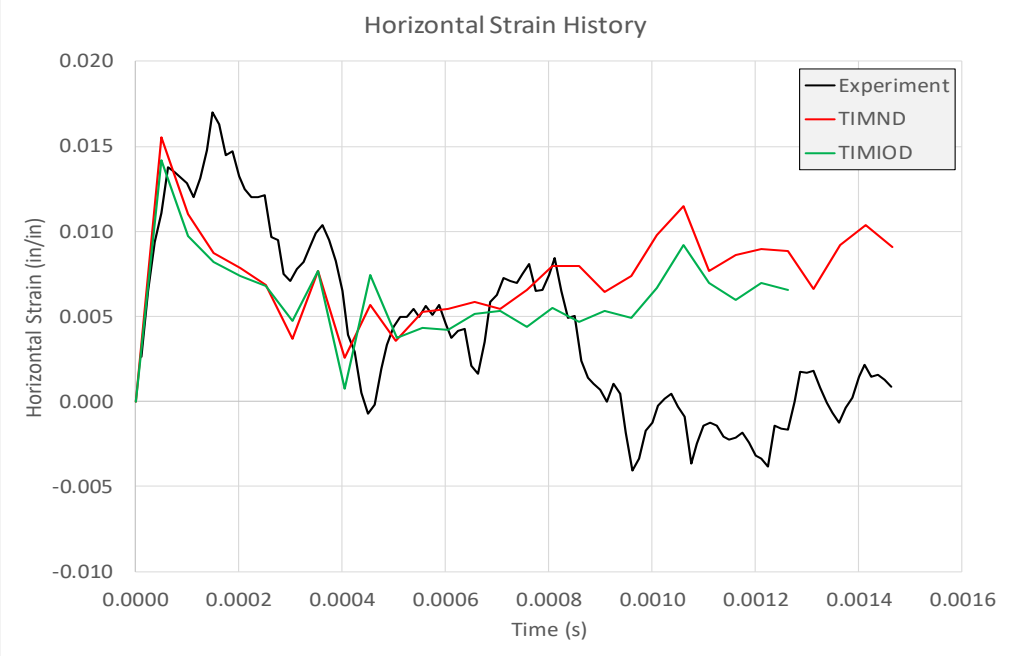

Figure 5-13. Horizontal strain time history comparison

Figure 5-14 shows a comparison of the delamination observed in the experiment and the delamination predicted by erosion of cohesive zone elements in the TIMIOD simulation.

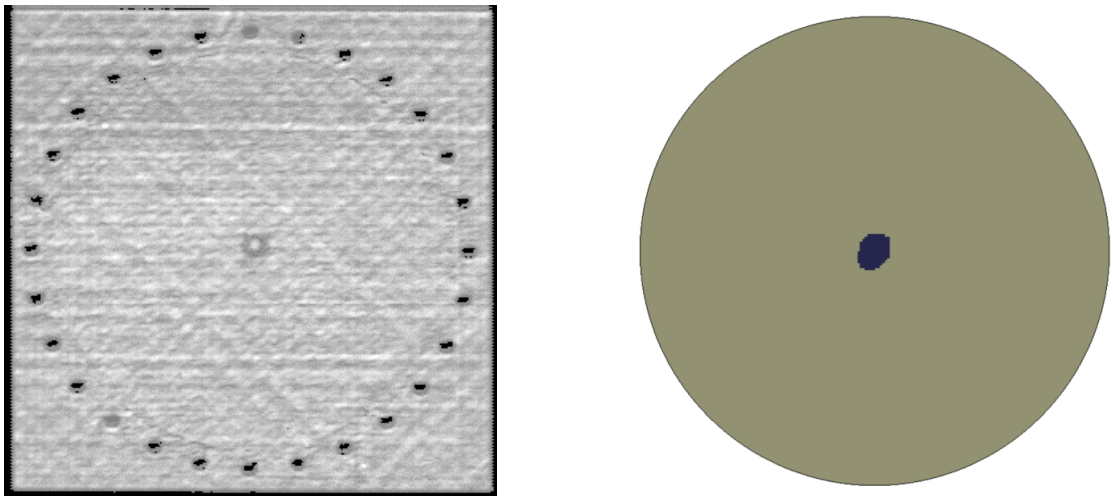

(a) (b)

Figure 5-14. Comparison of delamination damage (a) experiment and (b) TIMIOD simulation

5.3 LVG 1064

The LVG 1064 simulation utilized the same FE model as the LVG 1071 simulation. However, significant damage was observed in the experimental panel after testing. Figure 5-15 shows an ultrasonic scan of the panel after testing, with the dark grey region near the center indicating damage near the impact zone.

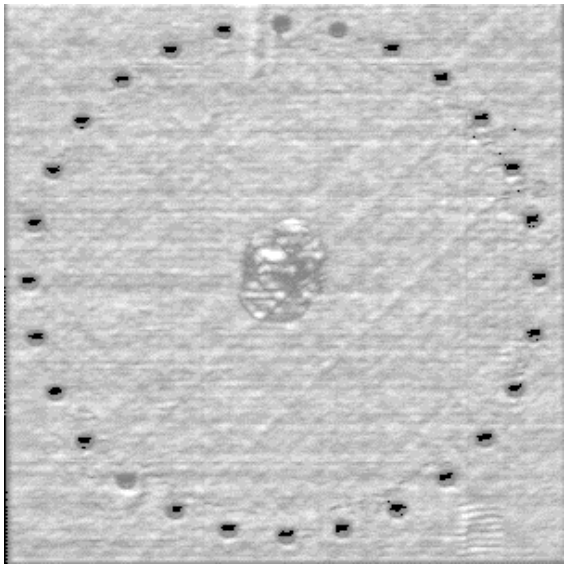

Figure 5-15. Ultrasonic scan image of the plate after impact

Due to the extent of the damage observed, the MAT213 damage sub-model was active during the experiment, along with the cohesive zone elements which were previously included.

Like LVG 1071, several runs were performed to exercise the deformation and damage sub models using different combinations of material data input. Table 5-5 summarizes the five runs that were performed, each using a distinct combination of input parameters.

Table 5-5 Material Models Exercised in the Finite Element Simulations

Material Model ID	Model Characteristics	Parameters
FOMND	Fully orthotropic model with no damage parameters	N/A
FOMID	Fully orthotropic model with in-plane damage parameters only	$d_{22_C}^{22_C}$, d_{12}^{12}
TIMND	Transversely isotropic model with no damage parameters	N/A
TIMID	Transversely isotropic model with in-plane damage parameters only	$d_{22_C}^{22_C}$, d_{12}^{12} , $d_{22_C}^{22_T}$, $d_{22_C}^{12}$.
TIMIOD	Transversely isotropic with in-plane and out-of-plane damage parameters	$d_{22_C}^{22_C}$, d_{12}^{12} , $d_{22_C}^{22_T}$, $d_{22_C}^{12}$, $d_{33_C}^{33_C}$, d_{13}^{13} , $d_{33_C}^{33_T}$, $d_{33_C}^{13}$

Fully coupled damage parameters were used in both the TIMID and TIMIOD simulations to investigate how coupled damage affects the simulations results.

5.4 SIMULATION RESULTS

In this section, the FE simulation results and comparison with experimental data are discussed. These discussions are divided into three categories or metrics for comparison: out-of-plane displacements, surface strains, and delamination and damage. It should be noted that all displacement and strain contours are obtained from the rear side of the panel.

5.4.1 Out-of-Plane Displacements:

Figure 5-16 shows the out-of-plane displacement field captured from the experiment and the simulations at the instance of time when the peak displacement occurs.

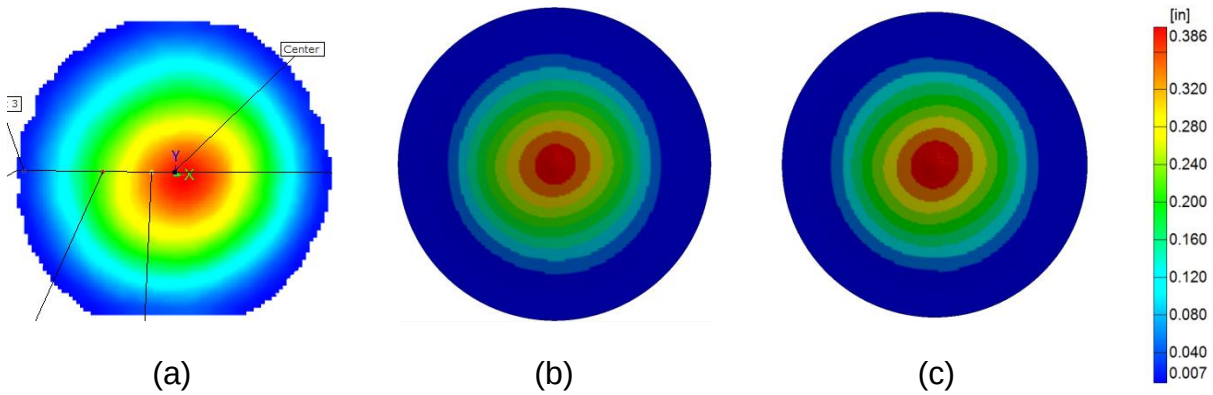

(a) (b) (c)

Figure 5-16. Out of plane displacement contour (a) experiment, (b) TIMID simulation, and (c) TIMIOD simulation (t=4.75(10)-4)

Qualitatively, the contours produced by the simulation in Figure 5-16 are consistent with the experiment. Figure 5-17 provides a quantitative comparison of the out-of-plane displacement of the center point of the panel in both the experiment and the simulations.

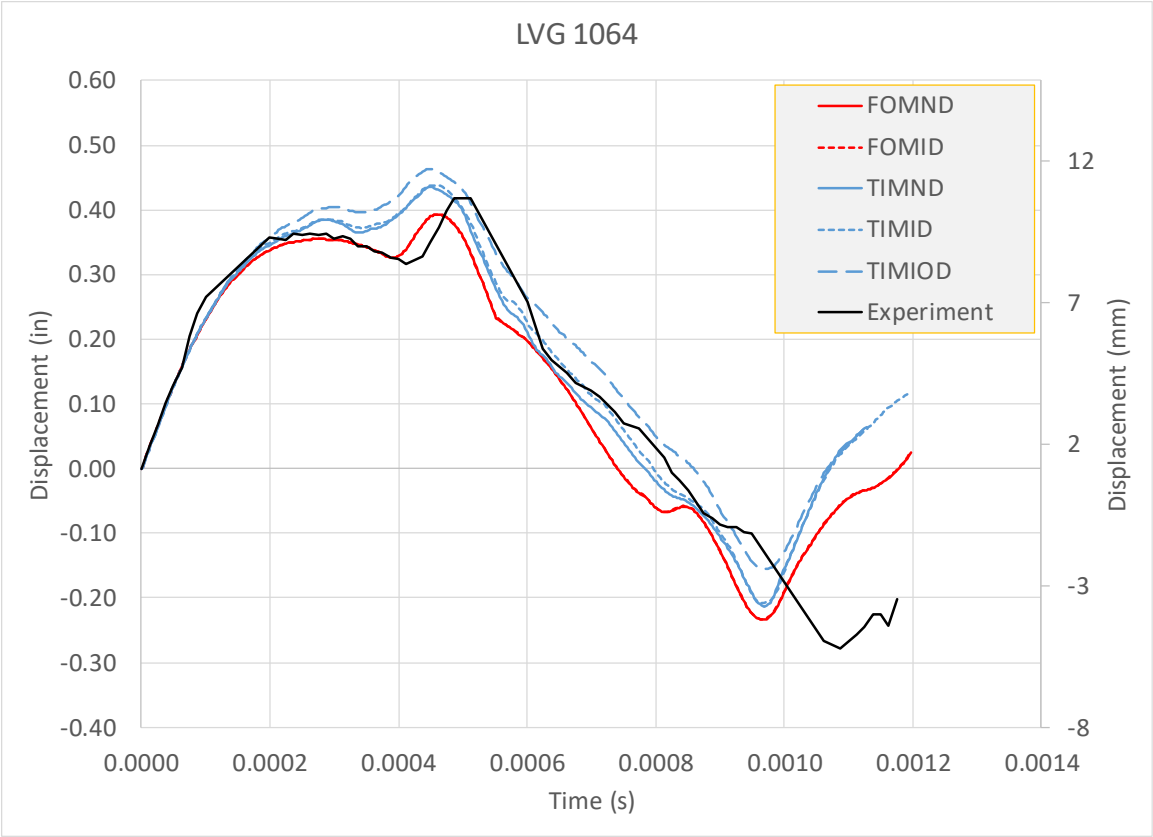

Figure 5-17. Out-of-plane displacement time history comparison of the center of the composite plate

The experimental data shown in Figure 5-17 is choppy because the small surface cracks at the impact location caused DIC data to be lost. The simulations were all terminated before the composite panel stopped oscillating since most of the damage observed in the experiment happened near the time of impact. Models utilizing only in-plane damage parameters show little to no change when compared with deformation only runs. Inclusion of the 3-direction damage parameters has the largest effect on the response of the system as is evidenced by the difference in the response between TIMID and TIMIOD. TIMIOD yields a higher estimate of the peak displacement than TIMND. This is expected, as the stiffness of the material has been reduced. Additionally, the out-of-plane displacement graphs of the transverse isotropy models which include damage (TIMID, TIMIOD), match the experimental data better than the deformation only models. Both the impacted panel and the simulation showed negligible permanent deformations that were too small to compare against each other.

5.4.2 Maximum Principal Surface Strain

Figure 5-18 shows the maximum principal strain field from the experiment and the simulations at the instance of time when the peak value occurs.

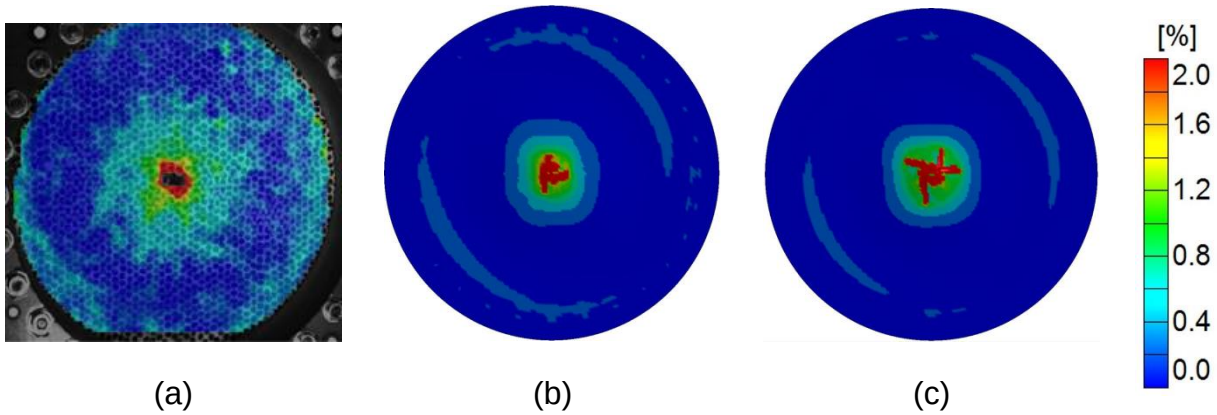

(a) (b) (c)

Figure 5-18. Maximum principal strain contour (a) experiment, (b) TIMID simulation, and (c) TIMIOD simulation (t=1.76(10)-4 s)

The contour in Figure 5-18(b) and Figure 5-18(c) shows a slightly larger area of maximum value than the contour shown in Figure 5-18(a).

Figure 5-19 provides a quantitative comparison of the maximum principal strain of a point to the right of center in both the experiment and the simulations respectively.

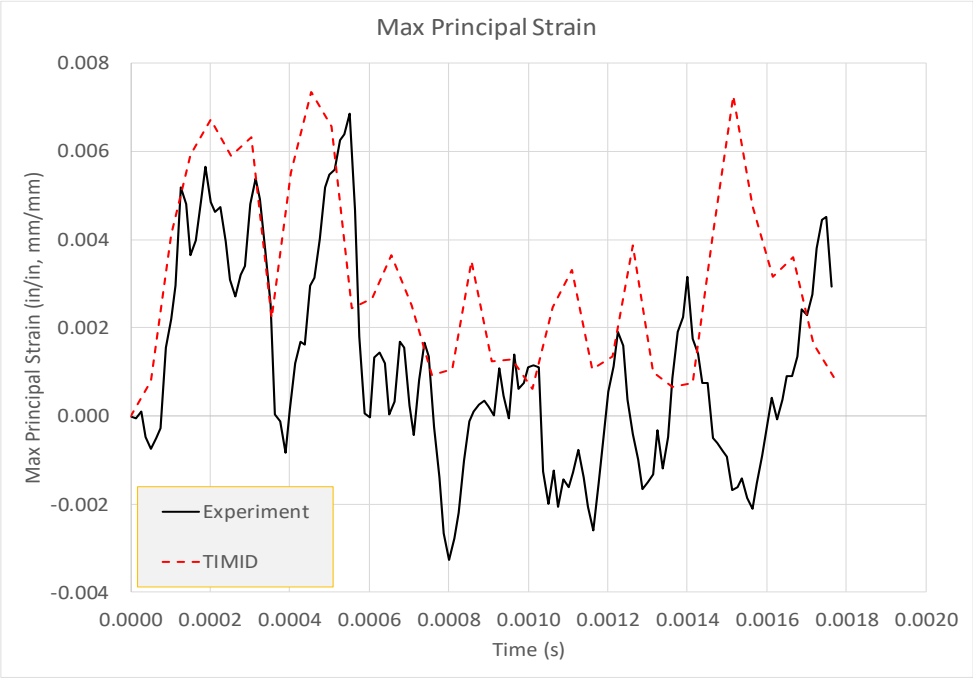

(a)

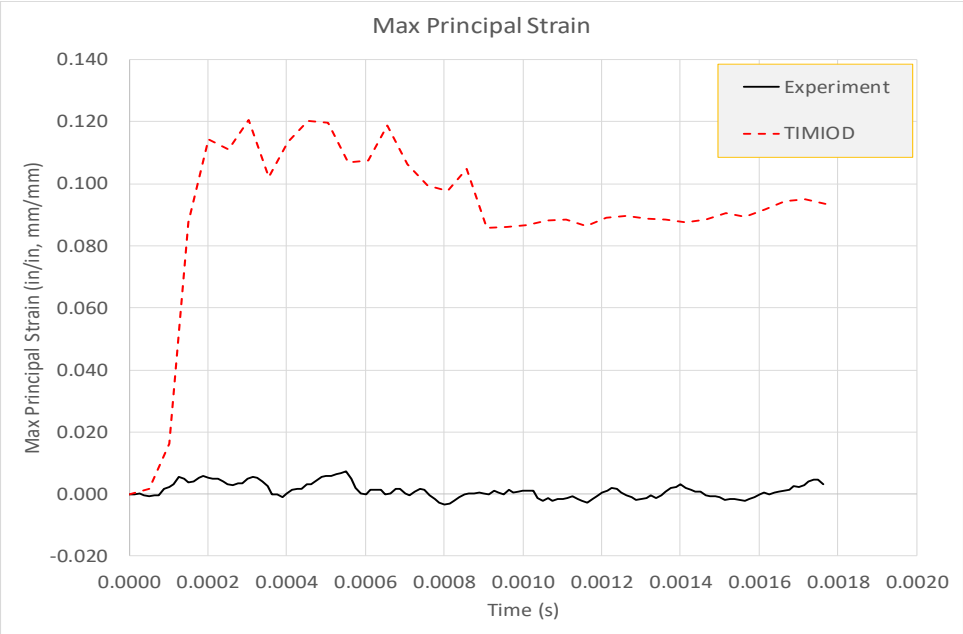

(b)

Figure 5-19. Maximum principal strain comparison (a) experiment and TMID simulation and (b) experiment and TIMIOD simulation

Figure 5-19(a) shows that the maximum principal strain predicted by the TIMID simulation is in good agreement with the experiment. However, some of the same issues seen elsewhere (not matching negative peaks as well as being out of phase with the experiment) are present. While the out-of-plane displacement is reasonably accurate in the TIMIOD simulation, the model grossly over predicts the maximum principal strain (Figure 5-19(b)). Additionally, the expected oscillatory behavior is not captured in the simulation.

5.4.3 Delamination and Damage

Figure 5-20 provides a comparison of the damage exhibited in the experiment, obtained through ultrasonic scan of the panel after the test, and the interlaminar delamination predicted by the finite element model.

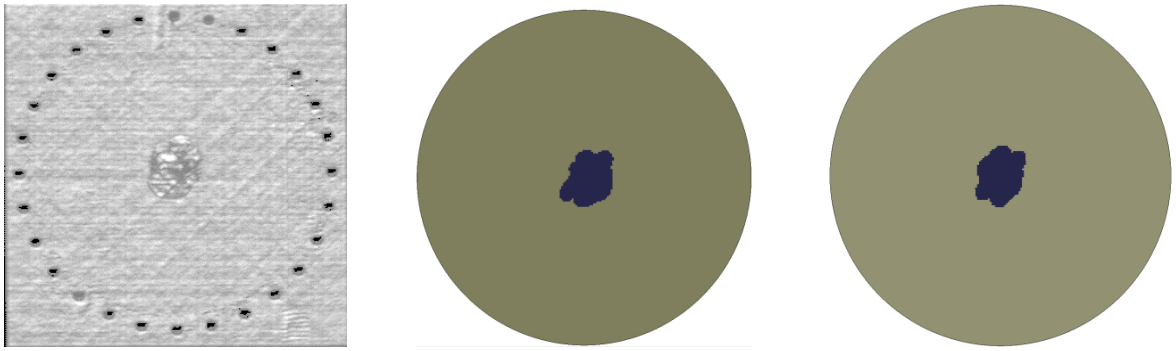

(a) (b) (c)

Figure 5-20. Delamination plot comparison (a) scanned image from ultrasound C-scan of the tested panel, (b) TIMID simulation, and (c) TIMIOD simulation

The dark region in the center of Figure 5-20 (b) and (c) correspond to failed cohesive zone elements - LS-Prepost was used with a transparency of 90% to show delamination through the thickness of the model. The location and overall shape and size of the experimental and simulation results are quite similar. Since the scanned image does not indicate between which layers delamination has occurred, the simulation results were processed to answer that question.

Figure 5-21 shows the failed cohesive zone elements between each ply starting from the side of the panel opposite the impact (Ply 16-15 boundary). The images show that visually observable delamination has occurred in 10 ply boundaries (15-14, 13-12, 12-11, 11-10, 10-9, 8-7, 7-6, 5-4, 4-3, 3-2).

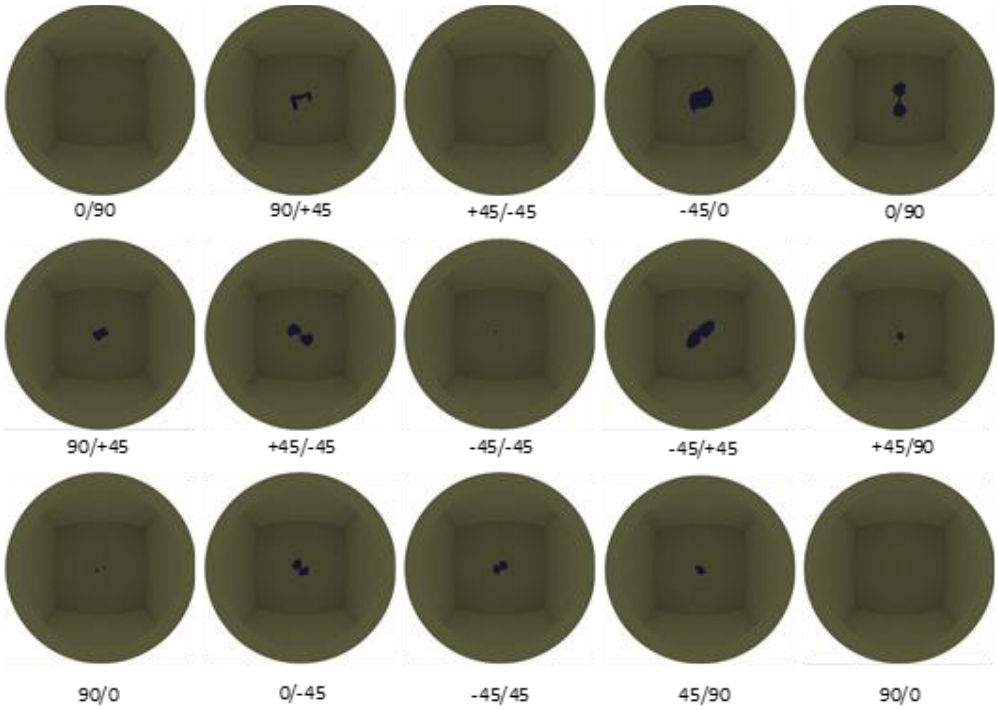

Figure 5-21. Cohesive zone element failure between adjacent plies in the finite element model (TIMIOD simulation)

The damage zones in Figure 5-21 match the cracked zone from the experimental panel. Though failure of the cohesive zone was captured in the simulation, the surface cracks observed in the experiment were not captured by the finite element model since no failure/erosion criteria were used for the composite parts.

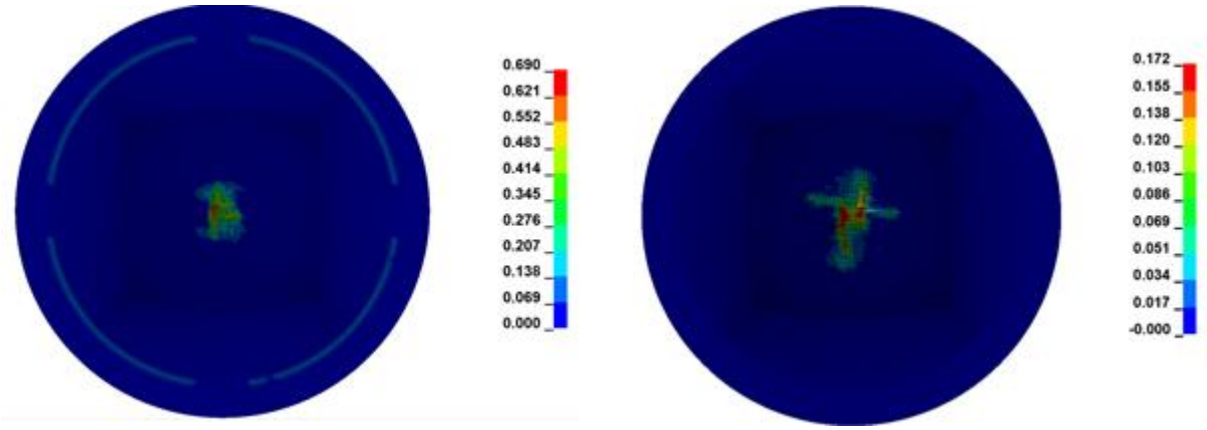

(a) (b)

Figure 5-22 shows the contour plots of two dominant damage parameters, $\left(d_{12}^{12}\right)$ and $\left(d_{33_C}^{33_C}\right)$, at the instance of time when the size of the damage zone has stabilized. Among the damage parameters included in the simulations (Table 5-5), the dominant damage parameters are defined as those whose final values are the largest when compared to their peak damage values from the experiments.

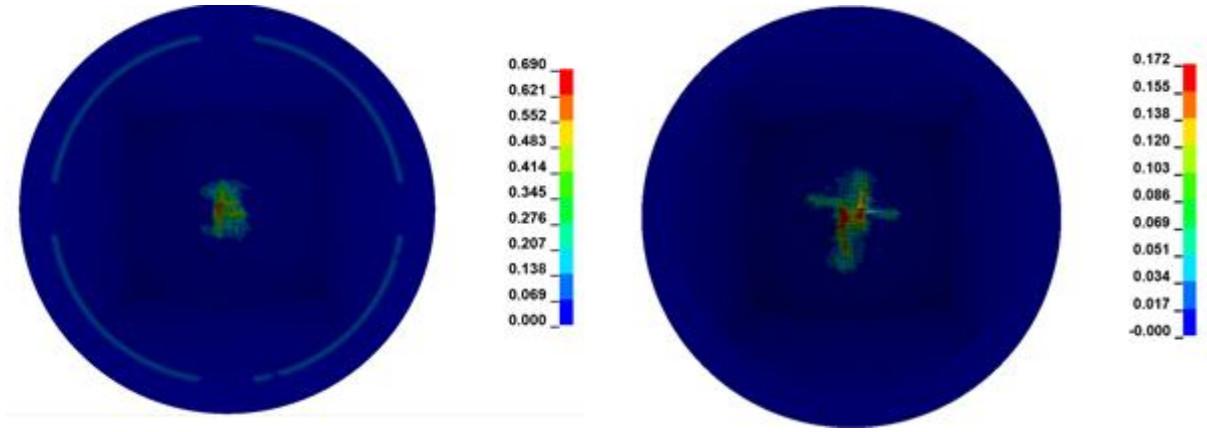

(a) (b)

Figure 5-22. Dominant damage parameter observed in (a) TIMID simulation $\left(d_{12}^{12}\right)$, and (b) TIMIOD simulation $\left(d_{33_C}^{33_C}\right)$.

Use of the first metric, the out-of-plane displacements, shows that the simulation predicted values are reasonably close to the experimental results both qualitatively and quantitatively. Differences in the first negative peak as well as the overall shape may be attributed primarily to modeling errors, errors in the input to the material model, and experimental errors. Similarly, a comparison of the principal strains shows the experimental and simulation values to be close both qualitatively and quantitatively. The assumption of transverse isotropy as well as the assumed damage parameters may have been used incorrectly.

Additionally, these simulations showed large strain rates in the elements near the impact region ($O(10^3)$). However, no rate dependent data was used in the simulations. The cohesive zone element properties may need to be recalibrated in order to properly represent the experimental conditions. Finally, the qualitative comparison of the damage, including delamination, shows good correlation between simulation and experiment.

6. CONCLUDING REMARKS

A list of desirable features for use in modeling a general composite was presented in chapter 1. We will re-examine the list here.

Desirable Feature	Link to MAT213
Continuum Damage Model with generalized, tabulated input, stress strain curve for non-damage related behavior (with limited or no curve fitting required by user).	A general (non-architecture dependent) orthotropic plasticity material model has been developed and implemented in LS-DYNA.
Current models use point-wise properties that lead to curve fit approximations to actual material response.	MAT213 deformation sub-model is driven by tabulated stress-strain data. No curve fit approximations are needed.
Tabulated input based on a well-defined set of mechanical property tests leads to more accurate representations of actual material behavior.	MAT213 verification tests show that (complex) orthotropic behavior can be accurately reproduced including tension-compression asymmetry, and rate and temperature dependencies.
Input parameters based upon standard mechanical property tests – although alternate specimen test configurations or micro-mechanic analytical approaches producing virtual test results should be acceptable.	MAT213 input does not differentiate between actual experimental, virtual test, or synthetic data.
Effects of strain rate need to be accounted for in a flexible, unified manner accounting for anisotropy of rate effects.	MAT213 accounts for rate dependencies.
Temperature dependency.	MAT213 accounts for temperature dependencies.
Strain based damage and failure parameters.	The damage sub-model is driven by tabulated strain data. The current suite of failure models in MAT213 include both strain- and stress-based failure models. The failure modeling will be improved in future work.
Failure parameters adjusted for mesh size, i.e., mesh regularization (to adjust for localization effects in element removal).	More sophisticated failure models are under development and will support failure parameters that are mesh independent.

Desirable Feature	Link to MAT213
Explicit modeling of interlaminar delamination via tiebreak contact and cohesive zone elements.	MAT213 will work with any material model used to model cohesive zone or tie-break behavior.
Shell and solid element implementations required (through thickness properties can be important).	MAT213 supports solid elements. Support for shell elements are under development.
Must be computationally fast.	Increasing the computational efficiency of MAT213 is proposed for the follow-on FAA-funded proposal.

6.1 FOLLOW-UP RESEARCH WORK

A proposal titled “Continued Development of MAT213 for Impact Analysis” was submitted to FAA in June, 2018 and was subsequently funded by the FAA for the period Aug 1, 2018 through July 31, 2020. The proposed work is divided into three tasks.

Task 1 deals with the improvements that are required to make MAT213 more versatile:

- support for rate and temperature dependencies,
- improvements to failure modeling to obtain more accurate and stable failure predictions,
- support for thick shell elements, and
- improvements that are required to speed up the overall computations with emphasis on plasticity calculations.

Task 2 deals with the development of additional verification and validation tests dealing specifically with the T800-F3900 unidirectional composite. Unidirectional composites are very widely used in the aerospace industry.

Task 3 deals with a combination of additional experiments and theoretical investigations to improve the understanding of the theory behind MAT213. This will enable users with varying degrees of experience to use MAT213 in a more efficient and robust fashion.

Appendix A provides a detailed list of journal papers, conference presentations and papers, and the list of grant-funded graduate student degrees obtained from this sponsored research work.

7. REFERENCES

[1] C. Hoffarth, S. D. Rajan, R. Goldberg, K. Carney, P. DuBois and G. Blankenhorn, "Implementation and Validation of a Three Dimensional Plasticity Based Deformation Model for Orthotropic Composites," *Composites A,* vol. 91, pp. 336-350, December 2016b.

[2] NASA, "Future Aircraft," 2 April 2015. [Online]. Available: https://www.nasa.gov/press/2015/april/nasa-creates-partnership-to-advance-composite-materials-for-aircraft-of-the-future.

[3] C. Hoffarth, B. Khaled, L. Shyamsunder, S. D. Rajan, R. Goldberg, K. Carney, P. DuBois and G. Blankenhorn, "Verification and Validation of a Three-Dimensional Orthotropic Plasticity Constitutive Model Using a Unidirectional Composite," *Fibers,* vol. 5, no. 1, pp. 1-13, 2017.

[4] L. P. Moreira and G. Ferron, "Finite element implementation of an orthotropic plasticity model for sheet metal forming simulations," *Latin American Journal of Solids and Structures,* vol. 4, pp. 149-176, 2007.

[5] M. Ganjiani, R. Naghdabadi and M. Asghari, "An elastoplastic damage-induced anisotropic constitutive model at finite strains," *International Journal of Damage Mechanics,* vol. 22, pp. 499-529, 2012.

[6] M. Buyuk, "Development of a New Metal Material Model in LS-DYNA, Part 2: Development of a Tabulated Thermo-Viscoplastic Material Model with Regularized Failure for Dynamic Ductile Failure Prediction of Structures Under Impact Loading," Federal Aviation Administration, Atlantic City, 2014.

[7] J. S. Bergstrom, "Constitutive Modeling of Elastomers - Accuracy of Predictions and Numerical Efficiency," 2005. [Online]. Available: PolymerFEM. com.

[8] A. Tabiei and J. Wu, "Three-dimensional nonlinear orthotropic finite element material model for wood," *Composite Structures,* vol. 50, pp. 143-149, 2000.

[9] R. Vaziri, M. D. Olson and D. L. Anderson, "A Plasticity-Based Constitutive Model for Fibre-Reinforced Composite Laminates," *Journal of Composite Materials,* pp. 512-535, 1991.

[10] P. Petit and M. Waddoups, "A method of predicting the nonlinear behavior of laminated composites," *Journal of Compsoite Materials,* vol. 3, pp. 2-19, 1969.

[11] X. Xiao, "Modeling Energy Absorbtion with a Damage Mechanics Based Composite Material Model," *Journal of Composite Materials,* vol. 43, pp. 427-444, 2009.

[12] F. Wu and W. Yao, "A fatigue damage model of composite materials," *International Journal of Fatigue,* pp. 134-138, 2010.

[13] H.-S. Chen and S.-F. Hwang, "A Fatigue Damage Model for Composite Materials," *Polymer Composites,* pp. 301-308, 2009.

[14] D. Allen, C. Harris and S. Groves, "A thermomechanical constitutive theory for elastic composites with distributed damage-I. Theoretical development," *International Journal of SOlids and Structures,* vol. 23, pp. 1301-1318, 1987.

[15] C. T. Sun and J. L. Chen, "A Simple Flow Rule for Characterizing Nonlinear Behavior of Fiber Composites," *Journal of Composite Materials,* 1989.

[16] O. Griffin, M. Kamat and C. Herakovich, "Three-dimensional inelastic finite element analysis of laminated composites," *Journal of Composite Materials,* vol. 5, pp. 543-560, 1981.

[17] M. Pindera and C. Herakovich, "An endochronic model for the response of unidirectional composites under off-axis tensile loads," in *Mechanics of Composite Materials: Recent Advances, Proceedings of the IUTAM Symposium on Mechanics of Composite Materials*, Blacksburg, 1982.

[18] D. Notta-Cuvier, F. Lauro and B. Bennani, "An original approach for mechanical modelling of short fiber reinforced composityes with complex distribution of fibre orientation," *Composites Part A,* vol. 62, pp. 60-66, 2014.

[19] V. Rajan, J. Shaw, M. Rossol and F. Zok, "An elastic-plastic constitutive model for ceramic composite laminates," *Composites Part A,* vol. 66, pp. 44-57, 2014.

[20] A. Boutaous, B. Peseux, L. Gornet and A. Belaidi, "A new modeling of plasticity coupled with damage and identification for carbon fibre composite laminates," *Composite Structures,* vol. 74, pp. 1-9, 2006.

[21] A. Matzenmiller, J. Lubliner and R. L. Taylor, "A constitutive model for anisotropic damage in fiber-composites," *Mechanics of Materials,* vol. 20, pp. 125-152, 1995.

[22] B. Khaled, L. Shyamsunder, N. Schmidt, C. Hoffarth and S. Rajan, "Experimental Tests to Characterize the Behavior and Properties of T800-F3900 Toray Composite," Tempe, 2018c.

[23] S. Kan, "Final Report on Probabilistic Modeling and Implementation in MAT 213," Fairfax, 2018.

[24] S. W. Tsai and E. M. Wu, "A General Theory of Strength for Anisotropic Materials," *J. Composite Materials,* vol. 5, pp. 58-80, 1971.

[25] I. M. Daniel and O. Ishai, Engineering Mechanics of Composite Materials, New York: Oxford University Press, 2006.

[26] W. H. Yang and W. W. Feng, "General and Specific Quadratic Yield Functions," *Journal of Composites,* vol. 6, no. 1, pp. 19-21, 1984.

[27] A. S. Khan and S. Huang, Continuum Theory of Plasticity, New York: John Wiley and Sons, 1995.

[28] J. Harrington and S. D. Rajan, "Test Results from Virtual Testing Software System," 2014.

[29] B. A. Bednarcyk and S. M. Arnold, "MAC/GMC 4.0 User's Manual - Keywords Manual," National Aeronautics and Space Administration, Washington, D.C., 2002.

[30] R. Goldberg, K. Carney, P. DuBois, C. Hoffarth, J. Harrington, S. Rajan and G. Blankenhorn, "Development of an Orthotropic Elasto-Plastic Generalized Composite Material Model Suitable for Impact Problems," *ASCE J of Aerospace Engineering,* vol. 29, no. 4, July 2016.

[31] "Brent's Method," 10 August 2018. [Online]. Available: https://en.wikipedia.org/wiki/Brent%27s_method.

[32] Livermore Software Technology Corporation, 2018. [Online]. Available: http://ftp.lstc.com/anonymous/outgoing/lsprepost/dev/.

[33] B. Khaled, L. Shyamsunder, C. Hoffarth, S. Rajan, R. Goldberg, K. Carney, P. DuBois and G. Blankenhorn, "Damage characterization of composites to support an orthotropic plasticity material model," *Journal of Composite Materials,* pp. 1-27, 2018a.

[34] T. A. Bogetti, J. Staniszewski, B. P. Burns, C. P. Hoppel, J. W. Gillespie Jr and J. Tierney, "Predictign the nonlinear response and progressive failureof composite laminates under triaxial loading: Correlation with experimental results," *Journal of Composite Materials,* vol. 47, no. 6-7, pp. 793-804, 2012.

[35] S. Tsai and E. Wu, "A General Theory of Strength for Anisotropic Materials," *Jourmal of Composite Materials,* vol. 5, no. 1, pp. 58-80, 1971.

[36] C. Hoffarth, "A Generalized Orthotropic Elasto-Plastic Material Model for Impact Analysis," PhD Dissertation, Arizona State university, Tempe, AZ. USA, 2016a.

[37] ASTM International, "ASTM D8101/D8101M-17 Standard test method for measuring the penetration resistance of composite materials to impact by a blunt projectile," ASTM International, West Conshohocken, PA, 2017.

[38] B. Khaled, L. Shyamsunder, C. Hoffarth, S. D. Rajan, R. K. Goldberg, K. S. Carney, P. DuBois and G. Blankenhorn, "Experimental characterization of composites to support an orthotropic plasticity material model," *Journal of Composite Materials,* vol. 52, no. 14, pp. 1847-1872, 2018b.

[39] G. A. Holzapfel and T. C. Gasser, "A viscoelastic model for fiber-reinforced composites at finite strains: Continuum basis, computational aspects and applications," *Computer methods in applied mechanics and engineering,* vol. 190, pp. 4379-4403, 2001.

[40] P. B. Lourenco, R. D. Borst and J. G. Rots, "A Plane Stress Softnening Plasticity Model for Orthotropic Materials," *International Journal for Numerical Methods in Engineering,* pp. 4033-4057, 1997.

[41] F. P. Van der Meer, "Mesolevel Modeling of Failure in Composite Laminates: Constitutive, Kinematic and Algorithmic Aspects," *Archives of Computational Methods in Engineering,* vol. 19, pp. 381-425, 2012.

[42] J. D. Littell, W. K. Binienda, W. A. Arnold, G. D. Roberts and R. K. Goldberg, "Effect of Microscopic Damage Events on Static and Ballistic Impact Strength of Triaxial Braid Composites," NASA, Washington, 2010.

[43] B. A. Gama, J.-R. Xiao, M. J. Haque, C.-F. Yen and J. W. J. Gillespie, "Experimental and Numerical Investigations on Damage and Delamination in Thick Plain Weave S-2 Glass Composites Under Quasi-Static Punch Shear Loading," U.S. Army Research Laboratory, Aberdeen Proving Ground, 2004.

[44] A. F. Johnson, A. K. Pickett and P. Rozycki, "Computational methods for predicting impact damage in composite structures," *Composites* Science *and Technology,* vol. 61, pp. 2183-2192, 2001.

[45] J. Ozbolt, V. Lackovic and J. Krolo, "Modeling fracture of fiber reinforced polymer," *International Journal of Fracture,* vol. 170, pp. 13-26, 2011.

[46] C.-F. Yen, "Ballistic Impact Modeling of Composite Materials," in *7th International LS-DYNA Users Conference*, 2002.

[47] J. Cho, J. Fenner, B. Werner and I. M. Daniel, "A Constitutive Model for Fiber-reinforced Polymer Composites," *Journal of Composite Materials,* vol. 44, pp. 3133-3150, 2010.

[48] K. Micallef, A. S. Fallah, P. T. Curtis and L. A. Louca, "A homogenised continuum constitutive model for visco-plastic deformation of uni-directional composites," *Composite Structures,* vol. 99, pp. 404-418, 2013.

[49] R. Goldberg, K. Carney, P. DuBois, C. Hoffarth, J. Harrington, S. Rajan and G. Blankenhorn, "Theoretical Development of an Orthotropic Three-Dimensional Elasto-Plastic Generalized Composite Material Model," in *13th International LS-DYNA User's Conference*, Detroit, MI, 2014.

[50] K. S. Raju and J. F. Acosta, "Crashworthiness of Composite Fuselage Structures - Material Dynamic Properties, Phase I," U.S. Department of Transportation: Federal Aviation Administration, Washington, DC, 2010.

[51] D. L. Smith and M. B. Dow, "Properties of Three Graphite/Toughened Resin Composites," NASA Technical Paper 3102, September 1991.

[52] O. Allix, "A composite damage meso-model for impact problems," *J. Composites Science and Technology,* vol. 61, pp. 2193-2205, 2001.

[53] J. Xu, A. Askari, O. Weckner and S. Silling, "Peridynamic Analysis of Impact Damage in Composite Laminates," *J. Aerosp. Eng.,* vol. 21, pp. 187-194, 2008.

[54] K. V. Williams, R. Vaziri and A. Poursartip, "A physically based continuum damage mechanics model for thin laminated composite structures," International *Journal of Solids and Structures,* vol. 40, pp. 2267-2300, 2003.

[55] J. Hallquist, "LS-DYNA Keyword User's Manual - Volume II: Material Models," Livermore Software Technology Corporation, 2013.

[56] E. J. Barbero, Finite element analysis of composite materials using Abaqus, Boca Raton, FL: CRC Press, 2013.

[57] J. Lemaitre and R. Desmorat, Engineering Damage Mechanics: Ductile, Creep and Brittle Failures, Berlin: Springer, 2005.

[58] T. Ogasawara, T. Ishikawa, T. Yokozeki, T. Shiraishi and N. Watanabe, "Effect of on-axis tensile loading on shear properties of an orthogonal 3D woven SiC/SiC composite," *Comp. Sci. Technol.,* vol. 65, no. 15-16, pp. 2541-2549, 2005.

[59] M. Salavatian and L. V. Smith, "The effect of transverse damage on the shear response of fiber reinforced laminates," *Comp. Sci. Technol.,* vol. 95, pp. 44-49, 2014.

[60] P. Ladeveze and E. Le Dantec, "Damage modeling of the elementary ply for laminated composites.," *Compos. Sci. Technol.,* vol. 43, no. 3, pp. 257-267, 1992.

[61] M. R. C. Fouinneteau and A. K. Pickett , "Shear mechanism modelling of heavy tow braided composites using a meso-mechanical damage model.," *Composites: Part A,* vol. 38, no. 11, pp. 2294-2306, 2007.

[62] S. Song, A. M. Waas, K. W. Shahwan, O. Faruque and X. Xiao, "Effects of Matrix Microcracking on the Response of 2D Braided Textile Composites Subjected to Compression Loads.," *Journal of Composite Materials,* vol. 44, no. 2, pp. 221-240, 2010.

[63] C. Wang, Z. Liu, B. Xia, S. Duan, X. Nie and Z. Zhuang, "Development of a new constitutive model considering the shearing effect for anisotropic progressive damage in fiber-reinforced composites," *Composites Part B: Engineering,* vol. 75, pp. 288-297, 2015.

[64] U. Santhosh, J. Ahmad, G. Ojard, R. Miller and Y. Gowayed, "Deformation and damage modeling of cermaic matrix composites under multiaxial stresses," *Composites Part B: Engineering,* vol. 90, pp. 97-106, 2016.

[65] J. Cheng, "Material Modeling of Strain Rate Dependent Polymer and 2D Triaxially Braided," University of Akron, Akron, OH, 2006.

[66] F. K. Chang and K. Y. Chang, "Post-failure Analysis of Bolted Composite Joints in Tension and Shear-Out Mode Failure," *J of Composite Materials,* no. 21, pp. 834-855, 1987a.

[67] F. -K. Chang and K. -Y. Chang, "A Progressive Damage Model for Laminated Composites Containing Stress Concentrations," *Journal of Composite Materials,* vol. 21, pp. 834-855, 1987b.

[68] S. T. Pinho, L. Iannucci and P. Robinson, "Physically-based failure models and criteria for laminated fibre-reinforced composites with emphasis on fibre kinking: Part I: Development," *Composites: Part A,* vol. 37, pp. 63-73, 2006.

[69] S. T. Pinho, L. Iannucci and P. Robinson, "Physically-based failure models and criteria for laminated fibre-reinforced composites with emphasis on fibre kinking: Part II: FE implementation," *Composites: Part A,* vol. 37, pp. 766-777, 2006.

[70] P. Maimi, P. P. Camanho, J. A. Mayugo and C. G. Davila, "A continuum damage model for composite laminates: Part I – Constitutive model," *Mechanics of Materials,* vol. 39, pp. 897-908, 2007.

[71] P. Maimi, P. P. Camanho, J. A. Mayugo and C. G. Davila, "A continuum damage model for composite laminates: Part II – Computational implementation and validation," *Mechanics of Materials,* vol. 39, pp. 909-919, 2007.

[72] P. B. Bogert, A. Satyanarayana and P. Chunchu, "Comparison of Damage Path Predictions for Composite Laminates by Explicit and Standard Finite Element Analysis Tools," in *47th AIAA/ASME/ASCE/AHS/*ASC *Structures, Structural Dynamics, and Materials Conference*, Washington D.C., 2006.

[73] C. Hoffarth, J. Harrington, S. D. Rajan, R. Goldberg, K. Carney, P. Du Bois and G. Blankenhorn, "Verification and Validation of a Three-Dimensional Generalized Composite Material Model," in *13th International LS-DYNA User's Conference*, Detroit, MI, 2014.

[74] R. Solecki and R. J. Conant, Advanced Mechanics of Materials, New York, New York: Oxford University Press, Inc., 2003.

[75] G. D. Roberts, R. K. Goldberg, W. K. Binienda, W. A. Arnold, J. D. Littell and L. W. Kohlman, "Characterization of Triaxial Braided Composite Material Properties for Impact Simulation," NASA, Washington, 2009.

[76] T. C. M. America, "https://www.toraycma.com," 2018. [Online]. [Accessed 2 March 2018].

[77] H. M. Deuschle and A. Puck, "Application of the Puck failure theory for fiber-reinforced composites under three-dimensional stress: Comparison with experimental results," *Journal of Composite Materials,* vol. 47, no. 6-7, pp. 827-846, 2012.

[78] K. Kodagali, A. Tessema and A. Kidane, "Progressive failure analysis of a composite lamina using Puck Failure Criteria," in *Thirty-Second Technical Conference, American Society for Composites*, West Lafayette, Indiana, 2017.

[79] R. Christensen, "Failure Criteria," 27 January 2008. [Online]. Available: http://www.failurecriteria.com/Media/Failure_Criteria_for_ Anisotropic_Fiber_Composite_Materials.pdf. [Accessed 7 April 2018].

[80] J. Ye and D. Zhang, "Prediction of failure envelopes and stress-strain curves of fiber composite laminates under triaxial loads," *Journal of Composite Materials,* vol. 46, no. 19-20, pp. 2417-2430, 2012.

[81] D. Zhang, L. Xu and J. Ye, "Prediction of failure envelopes and stress-strain curves of fiber composite laminates under triaxial loads: Comparison with experimental results," *Journal Composite Materials,* vol. 47, no. 6-7, pp. 763-776, 2012.

[82] J. Berthelot, Composite materials: mechanical behavior and structural analysis, New York, U.S.A.: Springer, 1999.

[83] S. Li and S. Lim, "Variational principles for generalized plane strain problems and their applications," *Coomposites A,* vol. 36, no. 3, pp. 353-365, 2005.

[84] H. M. Deuschle and B.-H. Kropline, "Finite element implementation of Puck's failure theory for fiber-reinforced composites under three-dimensional stress," *Journal of Composite Materials,* vol. 46, no. 19-20, pp. 2485-2513, 2012.

[85] A. Puck and H. Schurmann, "Failure analysis of FRP laminates by means of physically based phenomenological models," *Composites Science and Technology,* vol. 62, no. 12-13, pp. 1633-1662, 2002.

[86] R. Christensen , "Failure of Fiber Composite Laminates- Progressive damage and polynomial invariants," 8 August 2009. [Online]. Available: http://www.failurecriteria.com/Media/Failure_of_Fiber_Composite_Laminates-

_Progressive_Damage_and_Polynomial_Invariants.pdf. [Accessed 7 April 2018].

[87] R. K. Goldberg, K. S. Carney, P. DuBois, C. Hoffarth, B. Khaled, S. Rajan and G. Blankenhorn, "Analysis and Characterization of Damage Using a Generalized Composite Material Model Suitable for Impact Problems," *Journal of Aerospace Engineering,* pp. doi: 10.1061/(ASCE)AS.1943-5525.0000854, 2018.

[88] J. Harrington, C. Hoffarth, S. D. Rajan, R. GOldberg, K. Carney, P. DuBois and G. Blankenhorn, "Using virtual testing to complete the description of a three-dimensional orthotropic material," *Journal of Aerospace Engineering,* vol. 30, no. 5, pp. 04017025-1-04017025-14, 2017.

[89] R. Goldberg, K. Carney, P. DuBois, C. Hoffarth, J. Harrington, S. Rajan and G. Blankenhorn, "Development of and orthotropic elasto-plastic generalized composite material model suitable for impact probelms," *Journal of Aerospace Engineering,* vol. 29, no. 4, pp. 04015083-1-04015083-11, 2015.

APPENDIX A—SPONSORED RESEARCH PRODUCT LIST

REFERRED JOURNAL PAPERS

(1) R. Goldberg, K. Carney, P. DuBois, C. Hoffarth, J. Harrington, S.D. Rajan, and G. Blankenhorn, “Development of an Orthotropic Elasto-Plastic Generalized Composite Material Model Suitable for Impact Problems”, *ASCE J of Aerospace Engineering*, doi: 10.1061/(ASCE)AS.1943-5525.0000580. Dec 2015. Also 29:4, 1-11, 2016.

(2) C. Hoffarth, S.D. Rajan, R. Goldberg, K. Carney, P. DuBois, and G. Blankenhorn, “Implementation Validation of a Three-Dimensional Plasticity-Based Deformation Model for Orthotropic Composites”, *Composites A*, http://dx.doi.org/10.1016/j.compositesa.2016.10.024, 91:1, 336-350, December 2016.

(3) C. Hoffarth, B. Khaled, L. Shyamsunder, S.D. Rajan, R. Goldberg, K. Carney, P. DuBois, and G. Blankenhorn, “Verification and Validation of a Three-Dimensional Orthotropic Plasticity Constitutive Model Using a Unidirectional Composite”, *Fibers*, 5(1), 12; doi:10.3390/fib5010012, March 2017.

(4) J. Harrington, C. Hoffarth, S.D. Rajan, R. Goldberg, K. Carney, P. DuBois, and G. Blankenhorn, “Using Virtual Tests to Complete the Description of a Three-Dimensional Orthotropic Material”, *ASCE J of Aerospace Engineering*, DOI: 10.1061/(ASCE)AS.1943-5525.0000737, March 2017.

(5) B. Khaled, L. Shyamsunder, C. Hoffarth, S.D. Rajan, R.K. Goldberg, K.S. Carney, P. DuBois, and G. Blankenhorn, “Experimental Characterization of Composites to Support an Orthotropic Plasticity Material Model”, *J of Composite Materials*, DOI: 10.1177/0021998317733319, August 2017.

(6) R. Goldberg, K. Carney, P. DuBois, C. Hoffarth, B. Khaled, S.D. Rajan, and G. Blankenhorn, “Analysis and Characterization of Damage Utilizing a Generalized Composite Material Model Suitable for Impact Problems”, *ASCE J of Aerospace Engineering*, 10.1061/(ASCE)AS.1943-5525.0000854, March 2018.

(7) R. Goldberg, K. Carney, P. DuBois, C. Hoffarth, B. Khaled, L. Shyamsunder, S.D. Rajan, and G. Blankenhorn, “Implementation of a Tabulated Failure Model Into a Generalized Composite Material Model”, *J of Composite Materials*, https://doi.org/10.1177/0021998318786778, July 10, 2018.

(8) B. Khaled, L. Shyamsunder, C. Hoffarth, S.D. Rajan, R.K. Goldberg, K.S. Carney, P. DuBois, and G. Blankenhorn, “Damage Characterization of Composites to Support an Orthotropic Plasticity Material Model”, accepted, *J of Composite Materials*, June 2018.

CONFERENCE PRESENTATIONS AND PAPERS

(1) S.D. Rajan, “Finite Element Modeling of Composite Materials for Impact Loading”, *LS-DYNA Aerospace Working Group Meeting*, NASA-GRC, OH, September 2012.
(2) S.D. Rajan, “Implementation of a New Constitutive Model for Composite Materials Subjected to Impact Loading”, *LS-DYNA Aerospace Working Group Meeting*, LSTC, Livermore, CA, March 2013.
(3) S.D. Rajan, “MAT214: A Dry Fabric Model in LS-DYNA”, *LS-DYNA Aerospace Working Group Meeting*, LSTC, Livermore, CA, March 2013.
(4) R. Goldberg, K. Carney, P. Du Bois, *C. Hoffarth*, *J. Harrington*, S.D. Rajan, and G. Blankenhorn, “Theoretical Development of an Orthotropic Elasto-Plastic Generalized Composite Material Model”, *13th International LS-DYNA User's Conference*, Detroit, MI, June 2014.
(5) *C. Hoffarth*, *J. Harrington*, S.D. Rajan, R. Goldberg, K. Carney, P. Du Bois, and G. Blankenhorn, “Verification and Validation of a Three-Dimensional Generalized Composite Material Model”, *13th International LS-DYNA User's Conference*, Detroit, MI, June 2014.
(6) S.D. Rajan, *C. Hoffarth*, *J. Harrington*, R. Goldberg, K. Carney, P. Du Bois, and G. Blankenhorn, “An Orthotropic 3D Elasto-Plastic Material Model for Composite Materials Subjected to High Velocity Impact Loads”, *1st International Conference on Mechanics of Composites*, Stony Brook University, Long Island, NY, June 2014.
(7) R. Goldberg, K. Carney, P. Du Bois, *C. Hoffarth*, *J. Harrington*, S.D. Rajan, and G. Blankenhorn, “Development and Characterization of an Orthotropic Three-Dimensional Macroscopic Plasticity Model Suitable for Use in Composite Impact Models”, *17th U.S. National Congress on Theoretical and Applied Mechanics*, Michigan State University, East Lansing, MI, June 2014.
(8) S.D. Rajan, “Dynamic Impact Modeling of Polymer Matrix Composites using MAT213”, *Aerospace Working Group Meeting*, Livermore, CA, March 2015.
(9) R. Goldberg, K. Carney, P. Du Bois, *C. Hoffarth*, S.D. Rajan, and G. Blankenhorn, “Development and Characterization of a Rate-Dependent Three-Dimensional Macroscopic Plasticity Model Suitable for Use in Composite Impact Models”, *SAE 2015 World Congress*, Detroit, MI, June 2015.
(10) R. Goldberg, K. Carney, P. Du Bois, *C. Hoffarth*, S.D. Rajan, and G. Blankenhorn, “Incorporation of Plasticity and Damage Into an Orthotropic Three-Dimensional Model with Tabulated Input Suitable for Use in Composite Impact Problems”, *American Society for Composites*, East Lansing, MI, September 2015.
(11) R. Goldberg, K. Carney, P. Du Bois, *C. Hoffarth*, S.D. Rajan, and G. Blankenhorn, “Analysis and Characterization of Damage Utilizing an Orthotropic Generalized Composite Material Model Suitable for Use in Impact Problems”, *ASCE Earth and Space Conference*, Orlando, FL, April 2016.
(12) *C. Hoffarth*, *B. Khaled*, S.D. Rajan, R. Goldberg, K. Carney, P. Du Bois, and G. Blankenhorn, “Using Tabulated Experimental Data to Drive an Orthotropic Elasto-Plastic Three-Dimensional Model for Impact Analysis”, *14th International LS-DYNA User's Conference*, Detroit, MI, June 2016.
(13) R. Goldberg, K. Carney, P. Du Bois, *C. Hoffarth*, *B. Khaled*, S.D. Rajan, and G. Blankenhorn, “Incorporation of Damage and Failure Into an Orthotropic Elasto-

Plastic Three-Dimensional Model with Tabulated Input Suitable for Use in Composite Impact Problems", *14th International LS-DYNA User's Conference*, Detroit, MI, June 2016.
(14) R. Goldberg, K. Carney, P. Du Bois, *C. Hoffarth*, *B. Khaled*, S.D. Rajan, and G. Blankenhorn, "Analysis and Characterization of Damage and Failure Utilizing a Generalized Composite Material Model Suitable for Use in Impact Problems", *31st ASC Technical Conference and ASTM D30 Meeting*, Williamsburg, VA, Sept. 2016.
(15) S.D. Rajan and C. Hoffarth, "MAT213 Development: Status Update", *Aerospace Working Group Meeting*, Livermore, CA, March 2017.

GRADUATE STUDENT DEGREES

(1) Canio Hoffarth, “A Generalized Orthotropic Elasto-Plastic Material Model for Impact Analysis”, Doctoral Dissertation awarded December 2016.
(2) Bilal Khaled, “Experimental Characterization of Composites to Support an Orthotropic Plasticity Model”, in progress.
(3) Loukham Shyamsunder, “Deterministic versus Probabilistic Modeling of Deformation, Damage, and Failure During Impact Events using an Orthotropic Plasticity Model”, in progress.
(4) Joseph Harrington, “Using Virtual Testing for Characterization of Composite Materials”, Master of Science awarded May 2015.
(5) Nathan Schmidt, “Experimental Procedures and Data Analysis of Orthotropic Composites”, Master of Science awarded December 2016.